ULTRAFAST INVESTIGATIONS OF SLOW LIGHT IN PHOTONIC CRYSTAL STRUCTURES

Samenstelling van de promotiecommissie:

prof. dr. ir. H. J. W. Zandvliet (voorzitter)	Universiteit Twente
prof. dr. L. Kuipers (promotor)	Universiteit Twente
prof. dr. T. F. Krauss	University of St. Andrews
prof. dr. P. Lalanne	Université Paris-Sud
prof. dr. J. L. Herek	Universiteit Twente
prof. dr. K. Boller	Universiteit Twente
prof. dr. W. L. Vos	Universiteit Twente

The work described in this thesis is part of the research program of the
"Stichting Fundamenteel Onderzoek der Materie" (FOM), which is financially supported
by the
"Nederlandse Organisatie voor Wetenschappelijk Onderzoek" (NWO).

This work was carried out at:
NanoOptics Group,
FOM-Institute for Atomic and Molecular Physics (AMOLF)
Kruislaan 407, 1098 SJ Amsterdam, The Netherlands,
where a limited number of copies of this thesis is available.

ISBN: 978-90-77209-23-3
Printed by Pons & Looijen B.V., The Netherlands.

ULTRAFAST INVESTIGATIONS OF SLOW LIGHT IN PHOTONIC CRYSTAL STRUCTURES

PROEFSCHRIFT

ter verkrijging van
de graad van doctor aan de Universiteit Twente,
op gezag van de rector magnificus,
prof. dr. W. H. M. Zijm,
volgens besluit van het College voor Promoties
in het openbaar te verdedigen
op donderdag 19 juni 2008 om 15:00 uur

door

Rob Jacques Paul Engelen

geboren op 7 november 1977
te Tegelen

Dit proefschrift is goedgekeurd door:
prof. dr. L. (Kobus) Kuipers

Aan
mijn ouders

Publications related to this thesis:

H. Gersen, T.J. Karle, R.J.P. Engelen, W. Bogaerts, J.P. Korterik, N.F. van Hulst, T.F. Krauss & L. Kuipers, *Real-space observation of ultraslow light in photonic crystal waveguides*, Phys. Rev. Lett. **94**, 073903 (2005).

H. Gersen, T.J. Karle, R.J.P. Engelen, W. Bogaerts, J.P. Korterik, N.F. van Hulst, T.F. Krauss & L. Kuipers, *Direct observation of Bloch harmonics and negative phase velocity in photonic crystal waveguides*, Phys. Rev. Lett. **94**, 123901 (2005).

R.J.P. Engelen, T.J. Karle, H. Gersen, J.P. Korterik, T.F. Krauss, L. Kuipers & N.F. van Hulst, *Local probing of Bloch mode dispersion in a photonic crystal waveguide*, Opt. Express **13**, 4457 (2005).

R.J.P. Engelen, Y. Sugimoto, Y. Watanabe, N. Ikeda, K. Asakawa & L. Kuipers, *The effect of higher-order dispersion on slow light propagation in photonic crystal waveguides*, Opt. Express **14**, 1658 (2006).

M.D. Settle, R.J.P. Engelen, M. Salib, A. Michaeli, L. Kuipers & T.F. Krauss, *Flatband slow light in photonic crystals featuring spatial pulse compression and terahertz bandwidth*, Opt. Express **15**, 219 (2007).

R.J.P. Engelen, Y. Sugimoto, H. Gersen, N. Ikeda, K. Asakawa & L. Kuipers, *Ultrafast evolution of photonic eigenstates in k-space*, Nature Phys. **3**, 401 (2007).

R.J.P. Engelen & L. Kuipers, *Tracking light pulses with near-field microscopy* in A.V. Zayats & D.R. Richards (eds.), *Nano-Optics and Near-Field Optical Microscopy* (Artech House, Norwood, MA, U.S.A), in press.

R.J.P. Engelen, D. Mori, T. Baba & L. Kuipers, *On the subwavelength structure of the evanescent field of an optical Bloch wave*, submitted.

R.J.P. Engelen, D. Mori, T. Baba & L. Kuipers, *Two regimes of slow-light losses revealed by adiabatic reduction of group velocity*, submitted.

R.J.P. Engelen, D. Mori, T. Baba & L. Kuipers, *Probing the local dispersion relation of a chirped photonic crystal waveguide*, to be submitted.

M. Burresi, D. Mori, R.J.P. Engelen, D. van Oosten, A. Opheij, T. Baba & L. Kuipers, *Observation of phase singularities in the evanescent field*, in preparation.

Contents

1

1

Introduction

Periodic structures can be found throughout nature and are famous for their interesting properties for waves propagating through them. One of the best studied periodic structures are those of atomic or molecular crystals.[1] In these crystals, electrons are attracted by the nuclei which are periodically ordered. If the interaction between the electron waves and the periodic structure is particularly strong, physical effects like electronic bandgaps may occur.[2] Since the late 80's, there have been increasing efforts to apply the principles known from solid state physics to optical waves in periodic media.[3,4]

The optical analogue of an atomic crystal is a photonic crystal (PhC).[5,6] In such a crystal, materials with different refractive indices are alternated in a periodic fashion. Examples of such materials can in fact be found in nature. Some beetles and butterflies have evolved to self-assemble a photonic-crystal-like structure on their shells or wings that behaves as a broadband reflector[7] or can extract fluorescent light more efficiently than unpatterned wings.[8] Also man-made photonic crystals exist and they come in many sorts, from dielectric mirrors[9] to photonic crystal fibers[10] and artificial opals.[11]

In such crystals, the propagation of light is affected strongest if the wavelength of the light coincides with the periodicity of the lattice. For visible and near-infrared light, the lattice period of a photonic crystal must therefore be on the order of a few hundred nanometers. Due to the enormous progress in lithographic techniques, fabrication resolutions down to several nanometers are attainable, allowing the manufacturing of photonic crystals with very high quality.[12]

The ability to modify how and if light can propagate through a material leads to a means to control how embedded emitters can emit light. Modifying emission using photonic crystals has already been demonstrated to enhance or reduce emission rates[13,14] and can drastically improve efficiency of light emitting diodes.[15] Particularly interesting is the possibility to embed an emitter in a defect of a photonic crystal, that acts as an ultra-high-Q cavity.[16] The

strong coupling of emitter and cavity achieved in this way may be exploited in quantum information processing.

Another interesting property of photonic crystals is that they support so-called slow-light: light in a certain range of frequencies will propagate at velocities a few orders of magnitude slower than in vacuum.[17–19] Not only is it intriguing that one is able to manipulate the speed of light, but slow-light can also enhance the interaction of light with the medium and can thus improve sensing efficiencies and non-linear optical effects.[20] In particular enhanced nonlinear effects could pave the road to all-optical switching using miniature photonic crystal circuitry.

Crucial components in such circuitry will be waveguides. These guides are created by introducing lines of defects in the crystal lattice.[32] Light propagating in these waveguides is affected by the lattice in which the waveguide is embedded and therefore the waveguide exhibits strong dispersive effects like slow light. In this thesis, the optical properties of linear photonic crystal waveguides (PhCWs), coupled waveguides and composite photonic crystal devices are investigated, by probing the light in the near field. Various topic will be addressed, ranging from the physics of wave propagation in and above these waveguides, to how the dispersion can be engineered and what consequence slow light has for losses and pulse dynamics.

1.1 Photonic crystals

Photonic crystals can be fabricated by periodically stacking two or more materials with a high contrast in refractive index. Using such a stacking, one, two and three-dimensional photonic crystal can be created, as is depicted in figure 1.1. In a 1-dimensional crystal, when the period a corresponds to half of the wavelength of light in the medium, Bragg reflection[22] will occur, i.e., light incident along the stacking direction will be reflected back with nearly 100% efficiency. The larger the refractive index contrast of the materials used, the broader the range of frequencies over which Bragg reflection will occur range. In one-dimensional photonic crystals, Bragg reflection will only occur along the stacking direction, or in a narrow range of angles around this direction.

As shown in figure 1.1, two-dimensional and three-dimensional photonic crystals can be created by stacking rods or cubes, respectively. In the latter case, a proper choice of geometry and materials can create a so-called photonic bandgap, i.e., light in a certain range of frequencies cannot propagate in any direction through the material, or in other words, no photonic eigenstates exist for these frequencies.[3,23] Such conditions are very difficult to obtain. In order to open up a photonic bandgap, the materials used must have a large contrast in refractive index. In addition, the unit cell should be as spherical as possible and have very few defects. Particularly the last requirement is hard to fulfill, since imperfections in the lattice positions and roughness within a unit cell are unavoidable, even in

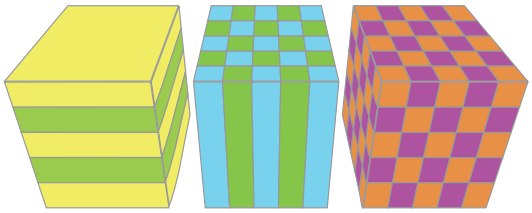

Figure 1.1: Schematic representation of three types of photonic crystals. From left to right: a multi-layer stack of materials, a periodic stacking of pillars and a cubic lattice of cubes.

state-of-art fabrication techniques.

1.2 Bloch waves

To understand the basic optical properties of a photonic crystal, we will describe the propagation of light through a one-dimensional photonic crystal.[24] Due to the discrete translational symmetry, the propagation of light is governed by Bloch's theorem,[2] which states that the amplitude of the light must conform to the imposed periodicity,

$$\psi_k(y) = u_k(y)\exp(iky), \text{ where } u_k(y) = u_k(y+a). \tag{1.1}$$

The Bloch wave ψ_k, with wavevector k, has a periodic amplitude modulation in space $u_k(y)$, which coincides with the lattice period a. Any Bloch wave obeying equation 1.1, can be written as

$$\psi_k(y) = \sum_m a_m \exp(i(k + m\frac{2\pi}{a})y), \text{ where } m \in \mathbb{Z}, \tag{1.2}$$

which is just an expansion in plane waves, each having an amplitude a_m. We will refer to these plane waves, indexed with m, as Bloch harmonics. The wavevector of each harmonic is spaced one reciprocal lattice vector $(2\pi/a)$ apart. The Bloch wave generally has one dominant harmonic, which we call the fundamental. The additional harmonics introduce a spatial beating which coincides with the periodic lattice. This spatial beating is of course the amplitude modulation $u_k(y)$ in equation 1.1.

The optical properties of a material are described in the dispersion relation, which relates wavevector and optical frequency of a wave. The dispersion relation of the first few Bloch modes is schematically depicted in figures 1.2a and 1.2b. Figure 1.2a shows the dispersion relation of a homogeneous medium, without a modulation of the refractive index. The dispersion relation is simply $\omega = ck/n$ (shown in black), with c the speed of light in vacuum and n the refractive index. Note that the slope of the dispersion relation determines the direction of propagation. Both the forward and backward propagating waves are depicted

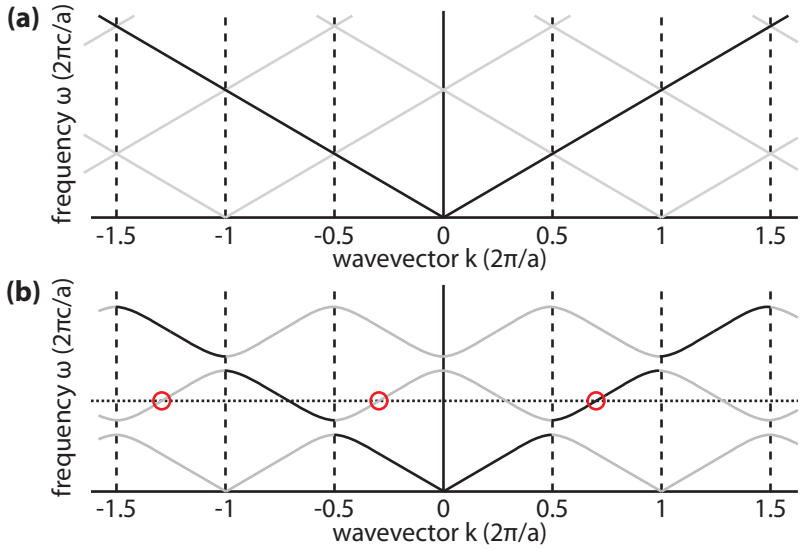

Figure 1.2: (a) Dispersion relation of a homogeneous medium indicated by the black line. The Bloch harmonics of a virtual periodicity (zero refractive index difference) are indicated by the gray lines. (b) In case there is a periodic modulation of the refractive index, avoided crossings appear at the Brillouin zone edges (vertical dashed lines) and mode gaps appear.

in figure 1.2. Waves in a homogenous medium can be considered a special class of Bloch waves without a spatial modulation $u_k(y)$. The harmonics (in gray) all having $m \neq 0$ in equation 1.2 then have zero amplitude.

When a refractive index contrast is present, the dispersion relation has avoided crossings at the edges of the Brillouin zones, resulting in the dispersion relation shown in figure 1.2. These edges are indicated by the dashed lines. Where the avoided crossings occur, a range of optical frequencies has no modes. No photonic eigenstates exist for these frequencies and a bandgap opens up. At the frequency indicated by the dotted line, a photonic eigenstate is found, which means a propagating wave exists. The Bloch wave excited at this frequency is composed of multiple wavevectors as is indicated by the red encircled intersections, as well as the wavevectors of the harmonics outside the plotted range.

All modes allowed in a periodic medium have harmonics in all Brillouin zones,[2] including one harmonic in the first irreducible Brillouin zone. In a one-dimensional representation, this zone is between $k = 0$ and $k = \pi/a$. A dispersion relation in which only the wavevectors in the first irreducible Brillouin zone are described, therefore includes all the modes allowed in the structure. By unfolding the dispersion relation of the first irreducible Brillouin zone into the adjacent zones, we obtain the full dispersion relation as is depicted in figure 1.2b. The wavevectors in such a dispersion relations are usually depicted in normalized units of $2\pi/a$ and the frequency has normalized units of $2\pi c/a$. These normalized units will be used throughout this thesis.

1.3 Waveguides

Arguably the most spectacular effects have been measured in a particular two-dimensional photonic crystal, a photonic crystal slab[14,19,25–29] which is graphically depicted in figure. 1.3a. The crystal slab consists of a thin film with a high refractive index, usually silicon or (Al)GaAs, in which a hexagonal lattice of air holes is etched. The film is suspended in a material with low refractive index, usually SiO_2 or air. Light can be confined in the thin slab of material, due to total internal reflection. This reduces the need for a periodicity in the third dimension. These structures can be fabricated with a very high accuracy with E-beam or optical lithography. In this thesis, the properties of waveguides embedded in these PhC membranes, as depicted in figure 1.3b, will be investigated.

At frequencies in the 2D-bandgap of the PhC membrane, light cannot propagate through the crystal. However, when a row of defects is created in the lattice of the photonic crystal, for example by leaving a row of holes in a photonic crystal slab unperforated, a state is created in the bandgap.[30,32] In this row of defects, propagating light will be strongly affected by the periodic nature of the surrounding crystal. The propagating light will therefore be a Bloch wave.[31] Figure 1.3b shows a schematic representation of a so-called W1 waveguide, which is formed by a single-line defect.[32] If a waveguide is two or three rows wide, it is

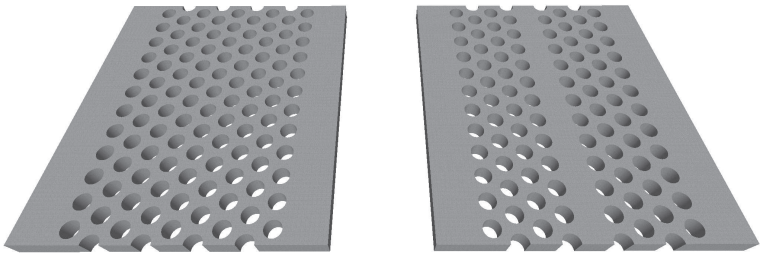

Figure 1.3: Photonic crystal slabs, a thin film of transparent material is perforated to yield a lattice of air holes. (a) A defect-free photonic crystal membrane. (b) A photonic crystal waveguide created by introducing a single-line defect in the lattice.

called a W2 or W3 waveguide, respectively.[33]

Figure 1.4 shows the dispersion relations of a W1, W2 and a W3 waveguide. Only wavevectors along the waveguide direction are shown, as the propagation of light through a linear defect is one dimensional. In all three dispersion relations, there are photonic eigenstates that allow light to propagate through the crystal. These states are represented by the shaded regions at the high and low frequency end of the diagrams. The frequency range between the crystal states is the 2D bandgap. Due to the linear defect introduced in the crystal, defect states are created in the bandgap. The width of the waveguide determines how many modes are supported by the waveguide. In figure 1.4, two modes are found in the narrow W1 waveguide, while the W3 waveguide supports up to 5 modes in the bandgap.

Each mode has a unique modal pattern in the waveguide.[21] The modes can be classified by the in-plane symmetry of the electric (E-)field with respect to the center of the waveguide. The even modes have a symmetric field distribution, while the odd modes have opposing E-fields alongside the waveguide. The modes with equal symmetry, are coupled via the periodic structure. As a result, avoided crossings can be observed for modes with the same symmetry. States with opposing symmetry do not interact and cross in the dispersion relation. An example of a crossing can be seen in the W1 dispersion relation at ω=0.295. Avoided crossings are depicted with the arrows in the dispersion relation of the W2 waveguide. An avoided crossing creates mini-stopbands in the dispersion relation: a range of frequencies where a range of wavevectors cannot propagate. Note that at the frequencies of a mini-stopband other modes may allow the guiding of light. In a photonic bandgap, there are no guided modes in a frequency range.

In the dispersion relations, also the so-called light line is plotted. This line corresponds to the modes of the material in which the slab is suspended, the cladding, and is described by $\omega = ck/n$ with n the refractive index of the cladding. The Bloch harmonics with a wavevector above the light line can couple to out-of-plane radiation. For light in a photonic crystal waveguide, only the modes underneath the light line are truly guided modes, which

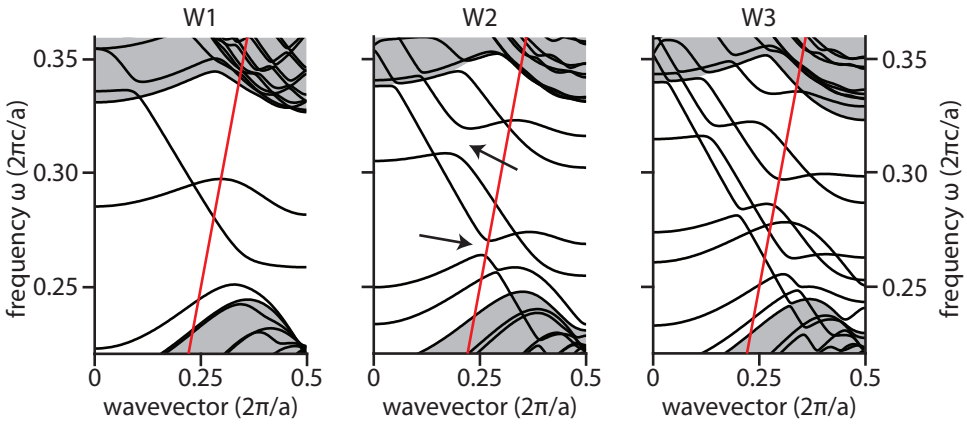

Figure 1.4: Dispersion relation for three symmetric PhC waveguides. From left to right: W1, W2 and W3 waveguides. The shaded region shows the crystal modes. A number of avoided crossings are depicted with arrows. The red line shows the light line ($\omega = ck$).

can (theoretically) propagate without radiative losses through the waveguide.

The modes in these waveguides have a field profile which is not completely inside the dielectric of the slab. A portion of the field extends into the photonic crystal region and (for photonic crystal slabs) into the cladding above and below the slab. The field in the cladding is bound to the waveguide and is called the evanescent field. Such an evanescent field can be used for coupling light in or out of a waveguide,[34] for sensing[35] or even as a trap for neutral atoms.[36] By probing the evanescent field with a so-called near-field microscope, the modes in the waveguide can be characterized. Phase-resolved near-field measurements can even reveal the dispersion relation, while time-resolved investigations can shed light on the dynamics of pulse propagation through photonic crystal structures.

1.4 Slow light

The dispersion relations discussed in the previous sections show that the wavevector of the waves in a PhC waveguide are strongly dependent on the optical frequency. Non-patterned structures would show merely straight or slightly bend modes in the dispersion relation.[37] The gradient of the bands is crucial for the dynamic response of a PhC waveguide, since the slope of the dispersion relation determines the group velocity of the propagating light,

$$v_g \equiv \frac{\mathrm{d}\omega}{\mathrm{d}k}. \tag{1.3}$$

As a result, the group velocity in photonic crystals is strongly dependent on frequency. As can be seen in the dispersion relations in figure 1.4 both shallow and steep slopes are

present. The steepest slopes correspond to group velocities around $c/5$, while light that is excited at a frequency where the dispersion relation is flattening will propagate at a very low group velocity. In the extreme case, at the Brillouin zone boundary, the dispersion relation is flat and as a consequence, light will theoretically be frozen in the waveguide.

These low group velocities have an intriguing effect on the E-field amplitude of a wave packet.[20] To illustrate this effect, we consider a pulse of light impinging on a slow-light medium from air. The pulse has a certain spatial extend in air. As a result of the lower v_g, the spatial extend of the pulse in the slow-light medium will be smaller than that in air. The energy density of the pulse is determined by the energy of the pulse and its spatial extend. If we now assume that all the energy of the pulse has been transmitted into the medium, this results in a higher energy density in the medium. In a photonic crystal, this results in an increase of the E-field intensity in the medium, roughly proportional to the inverse of the group velocity.

Since the group velocity in photonic crystals can be dramatically reduced, these structures are promising for the enhancement of light-matter interaction, especially in the case of nonlinear processes.[38] If the efficiency of such a process is sufficiently large, photonic crystals can be exploited for low threshold all-optical switching.

In the dispersion relations in figure 1.4, we can see that in the slow-light regime (where the slope is shallow), the curvature of the dispersion relation is rather high. This means that the group velocity of light in this photonic crystal waveguide is strongly dependent on frequency. The resulting second order derivative is called the group velocity dispersion and causes a broadening of pulses in time.[17,38] For processes where the electric field should be high, pulse broadening is obviously a disadvantageous effect, since the peak power of a pulse decreases due to this broadening.

Another effect that plays a role in slow light propagation is the influence of disorder in the photonic crystal lattice. Any imperfection in the lattice, such as a slight displacement of a unit cell, variations in shape or size of a cell or surface roughness, can cause losses.[39] As both slow light and the increase of the E-field are caused by multiple reflections of the light at the lattice sites, one can intuitively expect higher losses for slow light, since the interaction time with the medium and therefore also the chance of scattering at imperfections increases.

Photonic crystal structures are nevertheless promising for both passive and active optical devices, with highly integrated structures with dimensions on the micron-scale and responses in the picosecond time-scales. There are a number of challenges to be resolved, which lie on the forefront of the development of future applications. In this thesis we will investigate the fundamental properties of the waveguides and of composite structures.

1.5 Outline of this thesis

In chapter 2, we describe the near-field microscope used for the investigations of photonic crystal structures. With this microscope, the optical field of the propagating light can be mapped with subwavelength resolution. The near-field microscope can measure both the phase of the propagating light as well as track pulses in a time-resolved fashion. We describe the principles of the microscope, as well as a strategy to recover the phase and group velocity from near-field measurements. As a physical application of the microscope, the effect of group velocity dispersion (and higher-order dispersion) is described in this chapter.

In chapter 3, the evanescent field above a photonic crystal waveguide is investigated. We find that both the Bloch wave character as well as the confinement to a narrow waveguide has a profound effect on the evanescent field and shows its modal pattern changes as a function of height above the membrane.

Chapter 4 describes how the near-field microscope can be used to measure the dispersion relation of a PhC waveguide. The measurements have been performed on a waveguide where the dispersion relation changes as a function of position. Our measurements show how to recover the local dispersion relation of a waveguide in which the dispersion relation is not translationally invariant.

In chapter 5 we investigate the losses in the slow-light regime of a PhC waveguide. In this case, the losses increase due to a stronger interaction with the surrounding lattice. We were able to establish a power-law scaling of the losses and found that the losses scale with the inverse cube of the group velocity.

Chapter 6 is dedicated to a time-resolved investigation of the propagation of ultrafast pulses in a photonic crystal waveguide. We show that the pulse dispersion is much stronger in the slow-light regime. In fact higher order dispersion plays a significant role, which results in an asymmetric pulse broadening at low group velocities. In addition, we show how to engineer the dispersion by altering the waveguide width. The modified waveguide has a much lower dispersion and as a result, the pulse broadening is reduced.

In chapter 7, we describe measurements on a composite photonic crystal device, consisting of waveguides, bends and two coupled waveguides which together form a passive filter. Using the phase-sensitive near-field microscope we show how the photonic eigenstates can be separated, even when these states overlap spatially and temporally. By an analysis of the wavevectors in k-space, the states are separated and can thus be studied individually.

1

2 Interferometric near-field microscopy

The dynamics of light propagation on a femtosecond time scale can be visualized with a near-field microscope. To that end, the near-field microscope has to be integrated in an interferometer. We discuss the working and design considerations of such an interferometric near-field microscope. The interferometric near-field microscope is used to measure the propagation of pulses through a photonic structure. We show how to recover the phase and group velocity from the measurements.

2.1 Introduction

Many new optical structures appeared in recent years, which have intriguing properties due to nanoscale engineering. A few examples of such structures are meta-materials with a negative refractive index,[40] surface-plasmon-polariton structures[41] or highly integrated and miniaturized optics such as photonic-crystal-based circuitry.[42] With a near-field microscope, the intensity distribution of the light in or near a nanophotonic structure can readily be measured with a resolution that is beyond the diffraction limit, i.e., at a resolution not attainable by conventional microscopy. Near-field microscopy is therefore an invaluable tool for investigating novel optical nanostructures, especially since intriguing effects often occur on length scales comparable to the diffraction-limit or involve coupling phenomena on this length scale.[43]

Although such an investigation is useful to gain understanding of the time-averaged propagation properties, it does not reveal the dynamics of the propagation of light. These dynamics play an important role in, for example, ultrafast optical circuitry which is expected to improve the bandwidth of optical networks. In these structures, multiple optical com-

ponents have to be integrated into one device possibly not larger than a square millimeter. A local time-resolved near-field investigation is crucial for a detailed understanding of all the dynamic processes involved in such a composite device. Also in nonlinear optics, time-resolved near-field investigations are highly beneficial. For example, self-phase modulation or soliton formation can be monitored while the light propagates. How pulses evolve while undergoing a nonlinear interaction with, e.g., a nanostructure would be a fascinating topic for a time-resolved near-field investigation both from an academic and an engineering point of view. The relevant time scale in such a study is usually in the femtosecond domain. This poses a challenge in near-field microscopy, since most near-field optical microscopes map a time-averaged optical field in a nanostructure. Time-resolved microscopy with such a system would be limited by the frame rate of the microscope; given the typical acquisition time of near-field microscopy, the low frame rate would result in a time resolution of several minutes.

Time-resolved experimental investigations can be performed using high-speed electronics. Fast electronics may be able to record data up to the nanosecond regime. Specialized optical recording systems could possibly extend this range into the picosecond regime.[44] But it is impossible to record optical signals in the femtosecond range only with electronic means. The only option available on this timescale is to detect optical signals using other optical signals. The most common approach to obtain femtosecond time-resolved data in near-field microscopy is to incorporate the scanning set-up in an interferometer. After a short introduction into near-field microscopy in section 2.2, the principles of the heterodyne interferometer are discussed in section 2.3. The technique is applied in section 2.4 to find the phase and group velocity of light propagating through a ridge waveguide. The effect that very strong dispersion has on the tracking of pulses with a near-field microscope is discussed in section 2.5.

2.2 Near-field microscopy

Near-field microscopes exploit the optical interaction of a subwavelength-sized probe with a sample of interest. The microscope can be used in so-called illumination mode as well as collection mode.[43] In illumination mode, the near-field probe acts as a small source of light. The light can couple to the object under investigation. By analyzing the light coming from the object, its optical properties can be recovered. A near-field probe can also be used in collection mode, in which the light from an object is coupled to the near-field probe. In this thesis, we make use of a collection-mode microscope, where the source of the light is the light propagating in a photonic crystal structure.

A schematic representation of a near-field microscopy experiment on a photonic crystal waveguide is depicted in figure 2.1a. In this schematic, light is coupled into the waveguide, propagates along the waveguide and exits the structure at the end. The guided modes in the

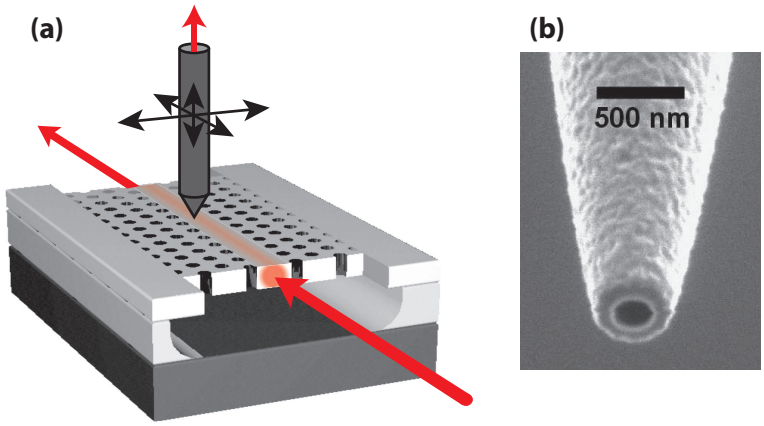

Figure 2.1: (a) Schematic representation of a near-field microscopy measurement on a photonic crystal waveguide. Light is coupled into the photonic crystal structure in which light is guided. A tapered optical fiber is placed in the evanescent field of the guided light. A portion of the propagating light couples to this near-field probe and can be detected in the far field. By scanning the probe over the surface of the structure, a map can be reconstructed of where the light is present in the structure. (b) Focused ion beam image of a typical near-field probe used in this thesis, consisting of an aluminum-coated tapered fiber. The apex is milled flat and, at the view angle of ∼45 degrees, its aperture is clearly visible. The size of the apertures used in this thesis is typically between 200 and 250 nm in diameter.

photonic crystals waveguide have a modal pattern that is confined to the crystal structure. However, a portion of the field, which is called the evanescent field, extends above and below the structure. By placing a near-field probe in the evanescent field of the structure, a small portion of the propagating field can couple to the probe. By using a tapered optical fiber as a probe, the collected light is transported away from the evanescent field and can be detected in the far field. When the fiber is raster scanned over the surface of photonic crystal structure, the distribution of light in the structure can be measured.

All the near-field measurements described in this thesis are performed with a metal-coated near-field probe. The apex of such a probe is depicted in figure 2.1b. The apex of the probe has been milled with a focussed ion beam. The result is an aluminum-coated fiber probe with a flat end facet. The glass of the fiber is visible as a dark circle in the center of the apex in figure 2.1b. Only the light directly underneath the aperture can couple to the fiber. All other light is shielded by the metallic coating of the probe. The resolution of the near-field microscope is therefore to first approximation given by the diameter of the aperture of the near-field probe.

The probe is kept at a fixed distance from the surface by a shear-force feedback mechanism. To this end, the fiber probe is glued to one of the prongs of a piezoelectric tuning fork, which is resonantly exited with a piezo actuator. When the probe is at close proximity to the surface ($2 - 20$ nm), the oscillation of the tuning fork is slightly damped and its resonance frequency shifts. When the electric signal from the fork is included in a feedback loop, the change in tuning fork ascillation due to the probe-surface interaction can be kept constant. As a result, also the height of the probe above the structure is kept constant. The resulting data obtained with such a near-field microscope is therefore both the optical information in the structure as well as the topography of the sample.

Near-field microscopes using the principles described above are widespread throughout the scientific community and can also be purchased at several companies. The applications of these microscopes vary from biology, chemistry, electrical engineering to physics. Specialized microscopes can even image in extreme conditions like ultrahigh vacuum and cryogenic environments. Most systems can only measure a time-averaged optical field of a structure, however. To visualize light pulses propagating through a structure, an interferometric addition to the microscope is required.

2.3 Heterodyne interferometry

A practical approach for time-resolved imaging on femtosecond time-scales is to place the microscope including the sample in one branch of a Mach-Zehnder interferometer.[45,46] In order to explain time-resolved near-field experiments, it is useful to review the principles of the interferometer. Therefore, the basic properties are introduced, including a discussion on the requirements on light sources in the interferometric set-up.

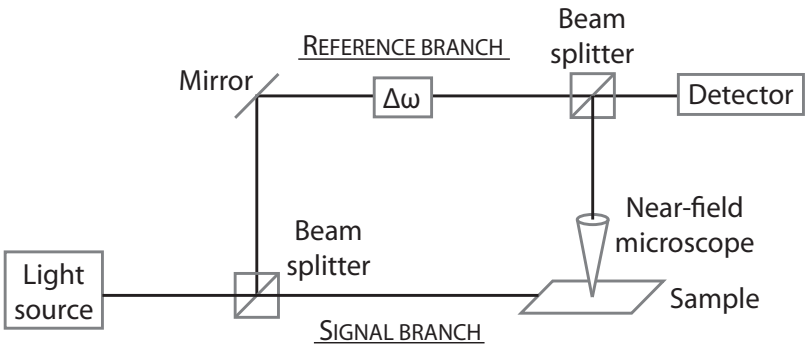

Figure 2.2: Schematic representation of a near-field set-up incorporated into a Mach-Zehnder interferometer. The incoming light is split into two branches, denoted signal and reference branch. In the signal branch, the light is coupled into a photonic structure and picked up by a near-field probe. The signal light and the reference light are mixed interferometrically with the second beam splitter and the interference between them is detected. In the heterodyne interferometer, the optical frequency of the light in the reference branch is shifted by $\Delta\omega$, so that the interference with the signal light yields a time-modulated interference signal on the detector.

2.3.1 Mach-Zehnder interferometer

Figure 2.2 schematically depicts a Mach-Zehnder interferometer with a microscope integrated. The incoming light is split into two branches, the signal and reference branch. The signal branch of the interferometer contains the photonic structure under investigation and the near-field microscope. In the reference branch, the light propagates through air. A small portion of the light in the structure is picked up by the near-field probe and mixed with the light from the reference branch. When the light of the two branches is mixed at the second beam splitter, the detector will register an interference signal. The intensity I_D on the detector will therefore be

$$I_D(t) = \epsilon_0 c\{|E_R(t)|^2 + |E_S(t)|^2 + 2\mathrm{Re}[E_R^*(t)E_S(t)]\}, \tag{2.1}$$

where ϵ_0 and c are the permittivity of free space and the speed of light in vacuo, respectively. E_R and E_S denote the electric field in the reference and signal branch, respectively. For monochromatic laser light, the amplitude $|E|$ is constant in time. Equation 2.1 can then be simplified to

$$I_D = \epsilon_0 c\{|E_R|^2 + |E_S|^2 + 2|E_R||E_S|\cos\Delta\phi\}. \tag{2.2}$$

In this equation, $\Delta\phi$ denotes the phase difference between the fields. There are three terms in equation 2.2, the first two are the intensities of the light in the two branches and are not phase-sensitive. The last term, however, mixes the two fields and is called the interference

term. The interferometric mixing is an advantage of the presented approach: the intensity from the probe ($\epsilon_0 c|E_S|^2$) is usually very weak, but in the interference term, the weak field from the signal branch is amplified by the strong field of the reference light. An interferometric approach thus allows the measurement of time-averaged intensities in the signals branch down to the femtoWatt regime.

If the near-field probe is moved to a different position on the surface of our sample, the optical path length of the signal branch changes. When the optical path from probe to mixing point remains the same, for example by using a fiber, only the path through the sample increases in length. Due to this change in length, the phase in the signal branch will change accordingly, leading to a change in $\Delta\phi$, which results in a change of the interference signal.

Our goal is to perform a time-resolved investigation of light in a photonic structure. Not surprisingly, this can be achieved with the same interferometric set-up. When using Fourier-limited (see section 2.3.3) laser pulses, the detector signal is

$$V_D(\tau) = \frac{C_D \epsilon_0 c}{T} \int_0^T \mathrm{d}t \, \{|E_R(t)|^2 + |E_S(t+\tau)|^2 + 2|E_R(t)||E_S(t+\tau)| \cos(\Delta\phi(\tau))\}, \tag{2.3}$$

with C_D the constant which describes the conversion of optical intensity to an electronic signal of the detector. Since the integration time of the detector T is usually much larger than the repetition rate of the laser, individual pulses are not detected. τ denotes the time difference in traversing the reference branch compared to the signal branch. The contribution of the interference term is maximal when the pulses in the signal and reference branches traverse the interferometer in the same time. Typically, in order to have a significant interference effect, the time difference τ must be at most in the order of the laser pulse duration ($\sim$100 fs).

In summary, if the position of the near-field probe on the surface of the sample is changed, the optical path length also changes. As discussed above, the resulting interference signal will change due to differences in relative phase $\Delta\phi$. At larger τ, the interference term also changes, since the temporal overlap of the pulses at the detector is changed.

2.3.2 Lock-in detection

In most experimental set-ups,[47–51] the frequency of the reference beam is intentionally slightly shifted with respect to the frequency of the incoming laser beam. In that case, the voltage of the detector for Fourier-limited pulses becomes

$$V_D(\tau) = C_D \epsilon_0 c \{\langle|E_R|\rangle^2 + \langle|E_S|\rangle^2 + \frac{1}{T}\int_0^T \mathrm{d}t \, 2|E_R(t)||E_S(t+\tau)| \cos(\Delta\phi(\tau) + \Delta\omega t)\}. \tag{2.4}$$

The frequency shift $\Delta\omega$ is usually in the kHz range and its period is longer than the integration time T of the detector. The interference of two beams of light with a slightly different optical frequency results in a time-modulated detector signal with a frequency of $\Delta\omega$. The modulated signal can readily be detected with a lock-in amplifier (LIA). The output of the LIA contains only the interference term in equation 2.4. The LIA has a double output. One output ($V_{LIA,\cos}$) contains the cosine of the phase difference:

$$V_{LIA,\cos}(\tau) = 2C_{LIA}C_D\epsilon_0 c\ \cos(\Delta\phi(\tau))\ \frac{1}{T}\int_0^T \mathrm{d}t\ |E_S(t+\tau)|\ |E_R(t)|, \tag{2.5}$$

The other output ($V_{LIA,\sin}$) is shifted by 90 degrees in phase, and therefore gives the sine of the phase, with the same amplitude as the cosine contribution:

$$V_{LIA,\sin}(\tau) = 2C_{LIA}C_D\epsilon_0 c\ \sin(\Delta\phi(\tau))\ \frac{1}{T}\int_0^T \mathrm{d}t\ |E_S(t+\tau)|\ |E_R(t)|. \tag{2.6}$$

The combination of the two signals gives the complex phase evolution by:

$$V_{complex}(\tau) = V_{LIA,cos} + iV_{LIA,sin} = 2C_{LIA}C_D\epsilon_0 c\,\mathrm{e}^{i\Delta\phi(\tau)}\ \frac{1}{T}\int_0^T \mathrm{d}t\ |E_S(t+\tau)|\ |E_R(t)|. \tag{2.7}$$

In this equation, the phase difference $\Delta\phi(\tau)$ depends on the difference in optical path length of the branches, and therefore shows the same evolution as the actual phase inside the photonic structure $\phi(z)$ as a function of position z. The cross-correlation of the fields amplitudes (the integral) is closely related to the actual field amplitude $E_{sig}(t)$, as is discussed in section 2.4.3. In fact, as a function of τ the shape of the cross-correlate qualitatively has the same shape in time as the actual pulse in the signal branch at the position of the probe. The amplitude of the interference signal (closely related to the actual E-field amplitude) is simply $|V_{complex}|$ and the phase is $\arg(V_{complex})$.

2.3.3 Light source requirements

The above treatment assumes a source of pulsed laser light, since this assumption relates more to intuition. However, only the temporal coherence of the light source matters for the time-resolved imaging. As such, also a non-coherent light source, for example a broadband LED or an incandescent lamp can be used instead of a pulsed laser system.

This property can be understood by evaluating equation 2.1 again,

$$I_D = \epsilon_0 c\{|E_R|^2 + |E_S|^2 + 2\mathrm{Re}[E_S^* E_R]\}. \tag{2.8}$$

As explained in the previous section, a heterodyne interferometric experiment ensures that only the interference term is detected. So

$$V_{LIA}(\tau) = 2C_{LIA}C_D\epsilon_0 c\ \frac{1}{T}\int_0^T \mathrm{d}t\ E_R^*(t)E_S(t+\tau). \tag{2.9}$$

This equation describes the output of the lock-in amplifier and is proportional to the cross-correlate of the field in the signal branch and the reference branch. Assuming that a non-coherent light source with a constant amplitude is used, the interference will tend to zero when τ becomes much larger than the coherence time of the light source, e.g., when the optical path length of the two branches differs significantly. The cross-correlate between the reference and signal light can be rewritten as a multiplication in the spectral domain:

$$V_{LIA}(\tau) = 2C_{LIA}C_D\epsilon_0 c\mathcal{F}^{-1}\{E_R^*(\omega)E_S(\omega)\}. \tag{2.10}$$

Here, $\mathcal{F}^{-1}$ denotes the inverse Fourier transform and $E_R(\omega)$ and $E_S(\omega)$ are in general complex. Equation 2.10 shows that in order to obtain a signal (V_{LIA}) on the lock-in amplifier, there must be spectral overlap between the light in the reference and the signal branch. However, also the phase matters which can be seen by separating the amplitudes and arguments of the spectra:

$$V_{LIA}(\tau) = 2C_{LIA}C_D\epsilon_0 c\,\mathcal{F}^{-1}\{A_S(\omega)A_R(\omega)\mathrm{e}^{i(\gamma_S(\omega)-\gamma_R(\omega))}\}. \tag{2.11}$$

In this equation, the spectral amplitudes are given by $A_R(\omega)$ and $A_S(\omega)$. The arguments $\gamma_R(\omega)$ and $\gamma_S(\omega)$ determine the temporal shape of the light. When $\gamma = 0$, the light is so-called Fourier-transform-limited,[52] indicating that the light consists of pulses, which are maximally compressed in time: their width in time is determined by the Fourier transform of the spectrum.

In equation 2.11, the exponent contains the difference in accumulated dispersion $\gamma_S - \gamma_R$. The argument $\gamma_S - \gamma_R$ will be non-zero, if the dispersion in the two branches is not balanced. Let us assume that the dispersion in the two branches is balanced, so the complex exponential in equation 2.11 yields unity. The only contributions left to the cross-correlation result V_{LIA} come from the spectra of the reference and signal light. Given this result, it does not matter what type of source produces the spectra. A broadband LED can give exactly the same result in an interferometric measurement as a femtosecond pulsed laser source. For the interferometric experiment, it does not matter what source is used, since the cross-correlation V_{LIA} only depends on the spectrum.

When light propagates through a medium, it acquires a dispersion of $\gamma(\omega) = zk(\omega)$, where z is the propagation length through the dispersive medium, and $k(\omega)$ is the dispersion relation of the material. The dispersion relation can be expanded in a Taylor series about a central frequency ω_0:

$$k(\omega) = \beta_0 + \beta_1(\omega - \omega_0) + \frac{\beta_2}{2}(\omega - \omega_0)^2 + \frac{\beta_3}{6}(\omega - \omega_0)^3 + \dots\ . \tag{2.12}$$

The propagation constants β_n describe the propagation of the light through a medium, where β_0 is proportional to the inverse of the phase velocity ($\beta_0 = \omega_0/v_\phi$) and β_1 is the inverse of the group velocity ($1/v_g$). The higher order terms are commonly used in describing pulse dispersion in, for example, fibers. The terms β_2 and β_3 describe the group

velocity dispersion (GVD) and third order dispersion (TOD), respectively. In each branch of the interferometer, the above equation describes the propagation of light, given that the medium through which the beam propagates has a uniform dispersion relation. Balancing the dispersion in the branches can be achieved with various materials, with different dispersive properties and different lengths, as long as the accumulated dispersion is equal. The most straightforward approach is to build a symmetric interferometer, where the branches of the interferometer contain exactly the same components. In principle, the unknown dispersion of the sample is then left as the only source of imbalance, which is exactly the desired situation.

For simplicity, the use of laser pulses is assumed, unless otherwise indicated. The pulsed laser is easier to relate to intuitively, while in fact, the same results will be obtained if a non-pulsed light source would be used, provided it has the same spectrum.

2.4 Application in near-field microscopy

In the following section, the interferometric set-up will be used in a near-field measurement in order to characterize a photonic structure. The individual elements of the near-field set-up are discussed as well as a measurement of pulses in a ridge waveguide and how to recover the phase and group velocities with the pulse tracking near-field microscope.

2.4.1 Set-up considerations

A number of groups have demonstrated a heterodyne version of the interferometric near-field microscope.[47–51] The microscopes can be separated into two types: scattering-type microscopes[48,51] and the collection-type, fiber-probe microscopes.[47,49,50] The first type of microscopes uses a apex of a sharp probe to scatter light from the structure in all directions, while in the other type, light tunnels from the structure into a sub-wavelength tapered fiber. In principle, both types can be used for time-resolved and phase-sensitive investigations. In the following, the second type will be described in greater detail. Most groups use a femtosecond laser system as a light source. Such a system has the advantage that it outputs a well collimated beam with high average power with a high spatial coherence. Figure 2.3 shows a typical set-up.

The frequency shifting in the reference branch, which is necessary for the heterodyne detection, is achieved by passing the laser beam through two acousto-optic modulators (AOMs). In such a modulator, the incoming wave is Doppler shifted by an $\sim$80 MHz acoustic wave. Two acousto-optic modulators are used in a crossed configuration to obtain an overall shift of the frequency of tens of kHz, which is the frequency difference in the two modulators. The interference of the original wave and the frequency shifted wave results in a time-modulated interference signal as described in section 2.3.2. Note that the specific use of

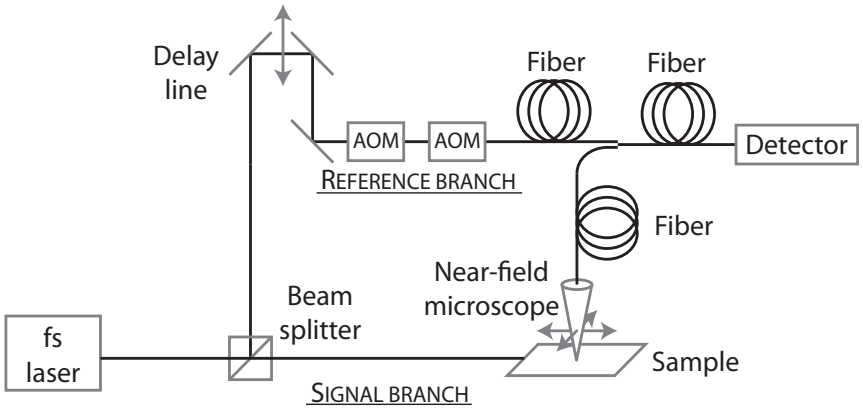

Figure 2.3: Schematic representation of a heterodyne near-field set-up. The incoming femtosecond pulses are split into two branches by a beam splitter. In the signal branch, the light is coupled into a photonic structure and picked up by a fiber-optic near-field probe, which can be scanned over the surface of the sample. The light in the reference branch is also coupled into a fiber. The signal light and the reference light are recombined by a fiber coupler and transported by a fiber to the detector. The optical frequency of the light in the reference branch is shifted by two acousto-optic modulators (AOM) in a crossed configuration. A delay line is included in the reference branch.

acousto-optic modulators as described here may lead to some confusion. A traveling-wave acousto-optic modulator accomplishes a shift in the frequency of the light without inducing an (extra) time dependence of the optical amplitude, which a standing-wave modulator induces.

Using a tapered fiber probe has the advantage that the distance from probe apex to mixing point does not change during scanning. It is therefore convenient also to use fiber optics in the rest of the optical set-up. The dispersion in these fibers is generally not negligible. The same holds for the dispersion caused by the acousto-optic modulators. The dispersion is not detrimental to the measurements, however, as long as the dispersion in the two branches is balanced, as discussed in section 2.3.3. One method to balance the dispersion, is to use the same length of optical fiber in each branch and to distribute the two AOMs over the two interferometer branches.

2.4.2 Pulse tracking in a waveguide

In a near-field experiment, a probe is scanned over the surface of a sample. When the detection path after the near-field probe is purely fiber optic, the optical path length, from probe apex to mixing point, does not change as the probe is scanned over the surface of the sample. The distance over which the light propagates in the sample, until the light reaches the probe, may however change. As a result, the delay time τ between the two branches of the interferometer will change. At small changes of τ, e.g. equivalent to a few optical cycles, consecutive constructive and destructive interference can be observed at the detector. Note that the amplitude in the reference branch is in general (much) higher than in the signal branch. The intensity of the interference will therefore not reach zero. At larger changes of τ, of the order of the coherence time of a pulse, the effective temporal overlap of the signal pulse and the reference pulse becomes smaller, resulting in a reduction of the interference amplitude.

In a near-field measurement, the delay time τ is continuously changed when the probe is scanned. A map of the interference will therefore appear like a snapshot of the propagating pulse: the interference fringes resemble the (co-)sine of the phase of the E-field, and the interference envelope resembles the pulse envelope in space.

2.4.3 Determination of the phase velocity

A pulse-tracking near-field measurement on a ridge waveguide as a model photonic structure is discussed next to demonstrate the working of the heterodyne interferometric set-up. The waveguide under investigation is a 2.08 μm wide waveguide, created by etching 3.5 nm deep in a 190 nm thick layer of Si_3N_4 on top of a SiO_2 layer. This waveguide can support two modes, one with the E-field oriented parallel to the slab and one with the E-field pointing out-of-plane.[53] Each of the two modes has a different effective refractive index.

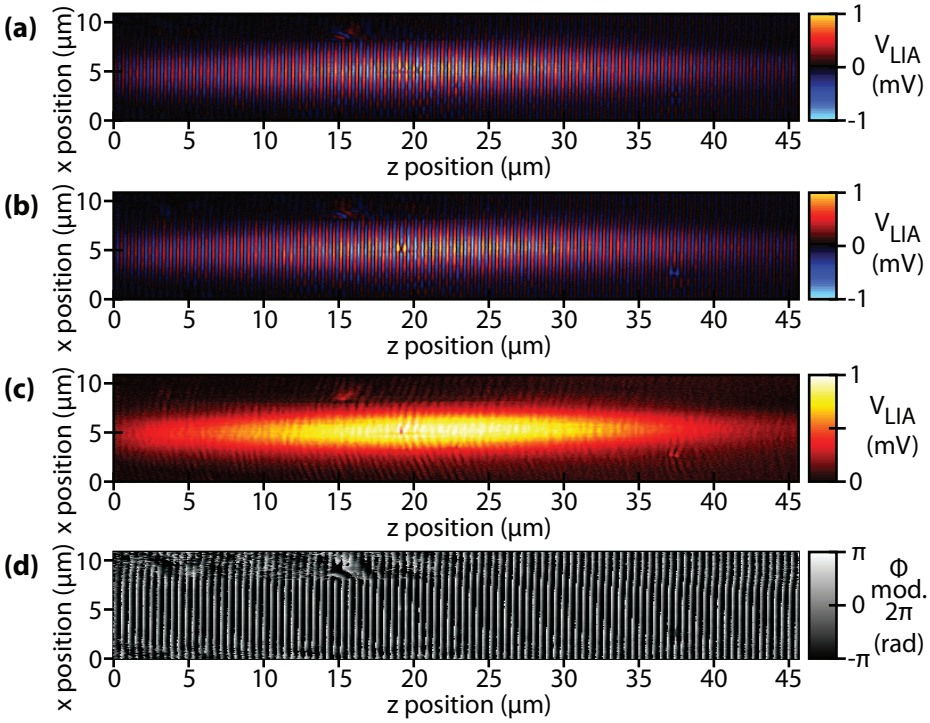

Figure 2.4: Results of a heterodyne near-field experiment on a femtosecond pulse in a ridge waveguide. (a) Signal from the lock-in amplifier representing the real part of the interference signal as in equation 2.5. (b) Corresponding imaginary part of the interference signal, as in equation 2.6. (c) Amplitude of the interference calculated by evaluating the measurements in (a) and (b). (d) In a similar fashion, also the phase, modulo 2π, can be recovered.

Since the phase of the light in the structure can be recovered with the interferometric near-field microscope and the optical frequency is known, the phase velocity can be measured in these waveguides. The signals $V_{LIA,cos}$ and $V_{LIA,sin}$ are depicted in figures. 2.4a and b, respectively. The colorscale indicates the root-mean-square value of the heterodyne detector signal. Note that the interference signal is on the order of ± 1 mV, while the detector signal from only the reference light was 520 mV. The intensity in the reference branch is much higher than the intensity picked up in the signal branch. The intensities in each branch can be estimated using equation 2.2. The power in the reference branch is found to be 0.1 μW, while the signal picked up by the near-field probe is approximately 0.1 pW: the intensity in the signal branch is 6 orders of magnitude lower than in the reference branch. The heterodyne detection scheme amplifies the signal using the reference light and can therefore readily be detected.

In figure 2.4a, the waveguide is oriented along the z-direction, and centered around $x = 5$ μm. A clear modulation pattern is present along z, which is strongest in the center of the waveguide and decreases away from $x = 5$ μm. The modulation is caused by the cosine term in equation 2.5: the optical path length changes due to the scanning of the probe resulting in consecutive constructive and destructive interference. The distance between two consecutive maxima is determined by $\Delta\phi$, the phase difference between the light in the reference branch and the signal branch. So when $\Delta\phi$ changes by 2π, the same signal is found, providing that the amplitude is constant. The optical path of the reference branch is constant, so the change in phase is due to the light in the signal branch only. A shift of 2π corresponds to a full cycle of the optical field in the structure and the distance between two maxima is therefore the same as the wavelength λ of the light in the waveguide.

The modulation pattern does not change away from the center of the waveguide in the direction perpendicular to the propagation, i.e., at larger or smaller x. The flat phase fronts proves that the phase of the light in the waveguide does not change perpendicular to the propagation direction as is expected for a zeroth order propagating mode. The same holds for the second LIA output channel, proportional to the sine of $\Delta\phi$ (see figure 2.4b), which appears to be the same image as figure 2.4a, but the phase is shifted by $\pi/2$.

Now that the real and imaginary part of $V_{complex}$ are recovered, as described by equation 2.7, the amplitude of the interference can be calculated by taking the absolute value of $V_{complex}$. The amplitude of the interference is depicted in figure 2.4c. The highest amplitude is found in the center of the waveguide, along $x = 5$ μm. The amplitude decays at larger and smaller x positions. Note that the amplitude pattern is wider than the 2-μm-wide waveguide. The larger spatial extent is the result of weak confinement due to the small effective index difference between waveguide and the Si_3N_4 slab.

The interference amplitude decays significantly at small or large z-values, which gives the pattern in figure 2.4c the appearance of a pulse in space. At small or large z-values, the time delay corresponding to the path length difference (τ) in the interferometer branches is larger than the coherence time of the light used. The interference amplitude is therefore

lower at small and large z-values (see equation 2.7). To what extent this pattern is an actual snapshot of a propagating pulse is discussed in section 2.5.1.

In a similar fashion as the amplitude, the phase of the light can be extracted from the measurements by taking the argument of $V_{complex}$. The phase modulo 2π, is shown in figure 2.4d. When following a line from left to right, the color changes gradually from white to black: the phase difference decreases. From $-\pi$, the phase jumps to π, which is represented by a color change from black to white.

Line traces of the measurement data are shown in figures 2.5a and b, showing the details of the amplitude ($|V_{LIA,complex}|$) and the real part of the lock-in signal (Re$\{V_{LIA,complex}\} = V_{LIA,cos}$) along the line $x = 5.1$ μm, respectively. The amplitude data shows a near Gaussian shape. A slight modulation is visible on the amplitude data, which may be due to interference of the propagating light with light that is scattered out of the waveguide at imperfections or dust particles.

As mentioned before, the modulation of the $V_{LIA,cos}$ signal corresponds to the oscillations of the field inside the waveguide. So the distance between two consecutive maxima gives the wavelength of the light in the waveguide. In order to find the effective index of the light in the waveguide, the $V_{complex}$ signal is Fourier transformed along the z-direction, to recover the periodicity of the E-field oscillations. The result is depicted in figure 2.5c, in which the amplitude of the transformed data is given as a function of the wavevector k_z of the light (or $2\pi/\lambda$). A clear peak is present at $k_z = 13.3$ μm^{-1}, corresponding to a wavelength of 472 nm. Since the central wavelength of the laser pulses used is 810 nm in vacuum, the effective refractive index is 1.71 ± 0.02, corresponding to a phase velocity (v_ϕ) of $1.75 \pm 0.02 \cdot 10^8$ m/s. The width of the peak in figure 2.5c is determined by the spatial extent of the measured interference.

The above exercise for determining the wavevectors is a very useful tool for determining the optical properties of integrated optical structures. By repeating the process for different optical frequencies, the dispersion relation $k(\omega)$ is recovered. In periodically nano-structured materials, for example photonic crystals, the relation between wavevector and frequency can become very complex.[54] This complexity can result in interesting optical properties, such as photonic bandgaps or slow light propagation.[18] With a phase-sensitive near-field microscope, the fundamental properties of photonic structures can be recovered with an unprecedented accuracy.

2.4.4 Determination of the group velocity

Other than the phase velocity, which is determined in the previous section, there is a second velocity of crucial importance present in nanostructured devices: the group velocity. This velocity (v_g) describes how fast a wavepacket, such as a laser pulse, travels through a

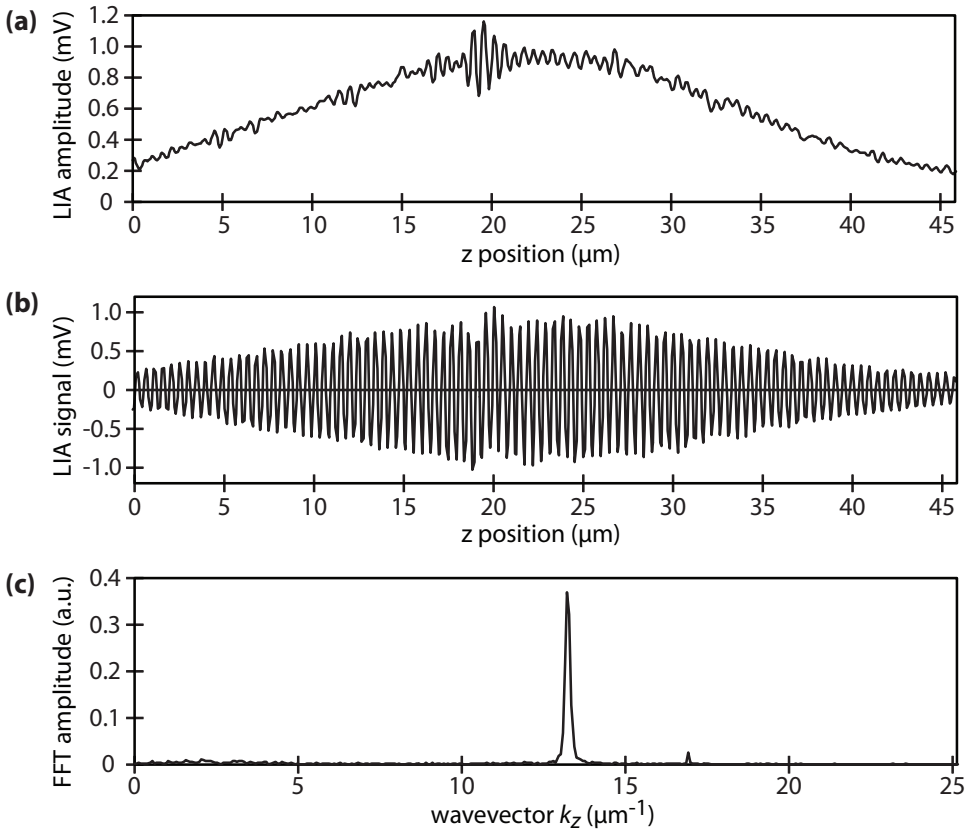

Figure 2.5: Details of the measurement show in figure 2.4. (a) Interference amplitude along $x = 5.1$ μm of figure 2.4c. (b) Real part of the complex measurement data showing the interference fringes due to scanning the probe over the waveguide taken from figure 2.4a along $x = 5.1$ μm. (c) Fourier transform of the complex measurement data showing the periodic components present in (b).

dispersive material. The group velocity is defined as

$$v_g \equiv \frac{\mathrm{d}\omega}{\mathrm{d}k}. \tag{2.13}$$

If the wavevector k is not linearly proportional to the optical frequency ω, the group velocity is different from the phase velocity. The difference does not require nanostructuring of materials. The intrinsic dispersion of materials is already sufficient to cause a difference in phase and group velocity of 1% for quartz or 11% for silicon at a vacuum wavelength of 810 nm.

The interferometric near-field microscope allows tracking of pulses as they propagate in a photonic structure, thus giving insight in the dynamic processes inside a photonic structure.[55] As a demonstration of the dynamics of pulses and how to track their propagation in a structure, the determination of the group velocity is demonstrated of a femtosecond pulse traveling through a simple model system: a conventional ridge waveguide.

In figure 2.4, a measurement of a laser pulse in a ridge waveguide was already presented. In fact, this measurement is one out of a series of measurements. In the complete set of measurements, a series of scans over the surface of the waveguide are performed. Between successive measurements, the length of the reference branch was changed, by moving the delay line in the set-up (see figure 2.3).

When the reference branch increases in length, the total length of the signal branch must also increase in order to achieve the maximum interference amplitude. The length of the signal branch can only become larger by changing the position of the near-field probe to a position further along the waveguide. As a result, each consecutive measurement for increasing lengths of the reference branch will result in a map of the interference amplitude, where the maximum of the interference envelope is at a different position in the waveguide.

A series of measurements, each with a different position of the delay line, is depicted in figure 2.6. It appears to be a series of snapshots of the propagating pulse at different times. The delay time at which the measurement is started is defined as zero delay time. At delay time 192 fs, the interference amplitude is maximal close to $z = 5$ μm: the optical path lengths of the reference and signal branch are equal at $z = 5$ μm.

As the conversion of the reference branch length change to a change in time delay is readily made, the changes in position can be tracked in time. In the waveguide, the pulse envelope moves with the speed of the group velocity. (Note that the phase moves with the phase velocity.) By evaluating the position of the maximum of the interference amplitude in the measurements, the group velocity can be found.

A Gaussian envelope is fitted to the interference amplitudes and the center position of the envelope is determined. The center positions as a function of delay time are depicted in figure 2.6g. A linear dependence is found for the position of the pulse as a function of the delay time. The slope corresponds to $1.44 \pm 0.02 \cdot 10^8$ m/s, which is the group velocity of

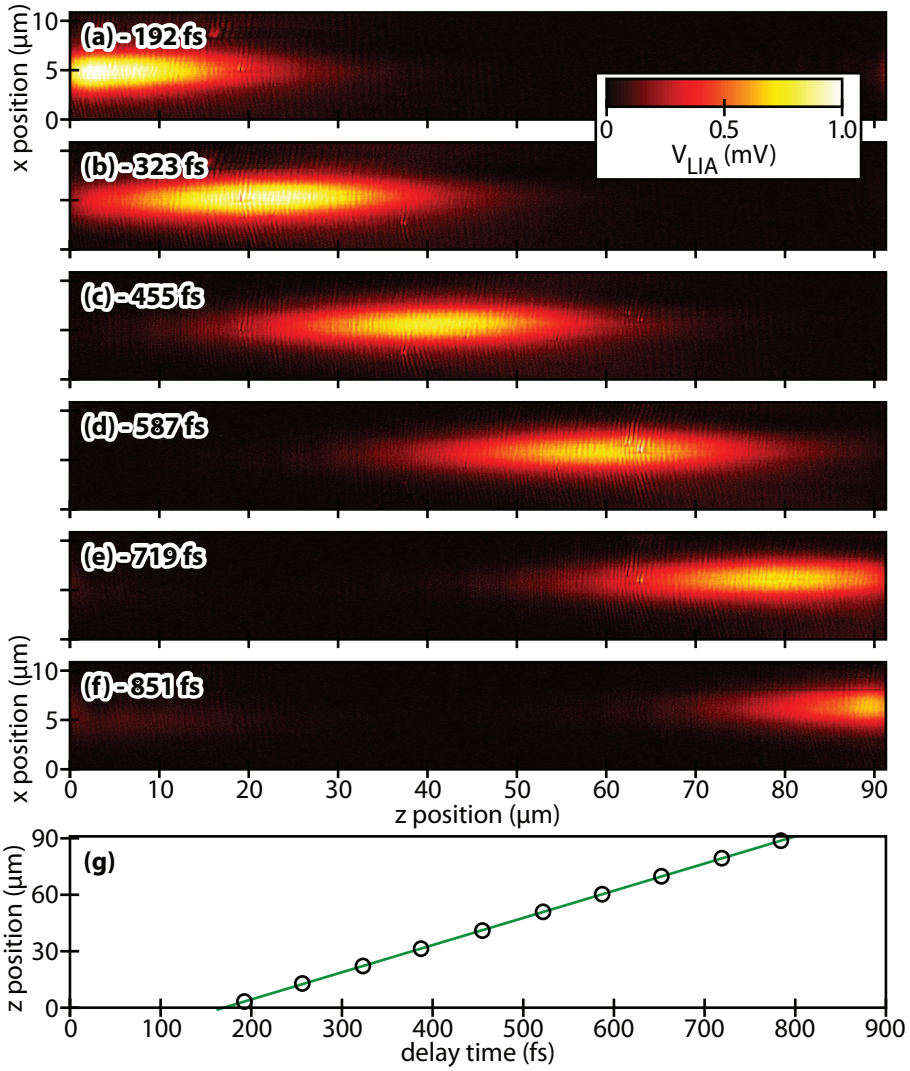

Figure 2.6: A series of pulse tracking measurements. (a-f) Amplitude of the lock-in signal of the same area ($91.6 \times 10.9\ \mu m^2$) *of ridge waveguide. Between each measurement, the optical length of the optical delay line is increased by 19.8 µm corresponding to a time-delay of 132 fs. (g) Position of the center of the interference peak as a function of delay time. The gray line shows a fit to the measurements, corresponding to a group index of* 2.08 ± 0.03.

the pulse in the waveguide. The group index n_g is 2.08 ± 0.03 (=), which is considerably different from the effective index (for the phase) of 1.71 ± 0.02.

The ridge waveguide has a fairly simple structure, which has a number of advantages for the analysis in this section. For example, the pulse retains its shape during propagation through the waveguide. Also, the pulse spectrum in the waveguide is the same as in the reference branch and remains that way. When the spectra differ however, care has to be taken when drawing conclusions from the interferometric data. In particular, if the dispersive properties vary significantly within the spectral bandwidth of the light used, the analysis is very complicated. In such a case, it is more suitable to use a narrow-band light source, e.g., a tunable laser, to recover the dispersion relation $k(\omega)$ and recover the dispersion constants β_N by differentiating the experimentally found $k(\omega)$.

The challenges that arise in a pulsed experiment if the dispersion in the structure is very large, and therefore deforms the pulse significantly, are addressed in the next section. The dispersive properties are still moderate however, and the spectrum of the pulses will hardly be affected.

2.5 Pulse tracking in dispersive media

In the previous section, the phase and group velocity were recovered. The propagation of light is governed by the dispersion relation $k(\omega)$, which can be expanded in a Taylor series as described in equation 2.12. The first two terms of this expansion describe the phase velocity and group velocity. A strategy to find the first two values has been described in the previous sections. In order to find the higher order values, the analysis requires additional effort. This section starts with a description of the effect of group velocity dispersion in near-field pulse-tracking experiments; subsequently, third and higher orders of dispersion are addressed.

2.5.1 The influence of group velocity dispersion

Group velocity dispersion (GVD) causes a pulse to broaden in time as it propagates through a dispersive medium. This effect can be significant in any (solid) material: for example, in fiber optic communication, pulses have to be compressed after a few kilometers of propagation. Also at a much smaller scale (within the scan area of a near-field microscope) this broadening may occur. The effect of group velocity dispersion on interferometric near-field measurements can still be described analytically.

Let us assume that the pulse in the reference branch is Fourier transform limited. The electric field of a Fourier-limited Gaussian pulse with a center frequency ω_0 is

$$E_{ref}(t) = A_{ref} \mathrm{e}^{i(\omega_0 + \Delta\omega)t - t^2/\sigma^2}, \tag{2.14}$$

The peak amplitude of the pulse in the reference branch is denoted by A_{ref} and the temporal width of the Gaussian pulse profile is determined by σ. The full width at half maximum (FWHM) is related to σ by FWHM$= 2\sigma\sqrt{\ln 2}$. Since the frequency of the light in the reference branch is shifted, the $\Delta\omega$ appears again. The equivalent in the frequency domain is obtained via a Fourier transformation:

$$\tilde{E}_{ref}(\omega) = \frac{A_{ref}\sigma}{\sqrt{2}} \mathrm{e}^{-\frac{1}{4}(\omega-\omega_0-\Delta\omega)^2\sigma^2}. \tag{2.15}$$

The pulse in the signal branch is initially Gaussian, but after traveling through a portion of the photonic structure, it acquires some dispersion $k \cdot z$. The electric field of the light is therefore

$$\tilde{E}_{sig}(\omega, z) = \frac{A_{sig}\sigma}{\sqrt{2}} \mathrm{e}^{-\frac{1}{4}\sigma^2(\omega-\omega_0)^2} \mathrm{e}^{ik(\omega)z}. \tag{2.16}$$

Note that this is the E-field as a function of frequency, not time. To elucidate the effect of group velocity dispersion only, the higher order terms, β_3 and higher in the Taylor expansion of $k(\omega)$ (see equation 2.12) are taken to be negligible. By substituting the expansion for $k(\omega)$, equation 2.16 becomes

$$\tilde{E}_{sig}(\omega, z) = \frac{A_{sig}\sigma}{\sqrt{2}} \mathrm{e}^{iz\beta_0 + iz\beta_1(\omega-\omega_0) + [\frac{1}{2}iz\beta_2 - \frac{1}{4}\sigma^2](\omega-\omega_0)^2}. \tag{2.17}$$

At the detector, the interferometrically mixed signal from the reference and signal branch is detected. This signal is averaged for a characteristic time T. For the detected signal by the LIA the averaging yields the following cross-correlation of the fields:

$$V_{LIA,complex}(\tau, z) \propto \int_T \mathrm{d}t \; E_{ref}(t+\tau) E_{sig}(t, z). \tag{2.18}$$

There as two ways to change the length of the branches: by moving the delay line in the reference branch (see figure 2.3), or by changing the position of the probe. These two methods are described in the above equation by a change in τ or z, respectively. The detector signal is the convolution of the field in the reference branch and the signal branch. The equivalent in the frequency domain is a multiplication of the fields:

$$V_{LIA,complex}(\tau, z) \propto \mathcal{F}^{-1}[\tilde{E}_{ref}(\omega)\tilde{E}_{sig}(\omega, z)]. \tag{2.19}$$

The following analysis will focus on the shape of the pulse envelope. The phase of the interference signal will therefore not be evaluated. As described in equation 2.18, the amplitude of the complex measured signal from the lock-in amplifier is proportional to the amplitude of the cross-correlated fields.

The two fields from the reference and signal branches in equations 2.15 and 2.17 are multiplied to yield

$$\tilde{E}_{ref}(\omega)\tilde{E}_{sig}(\omega, z) = \frac{A_{sig}A_{ref}\sigma^2}{2} \mathrm{e}^{i\beta_0 z - \frac{1}{4}\sigma^2\Delta\omega^2 + (i\beta_1 z + \frac{1}{2}\sigma^2\Delta\omega)(\omega-\omega_0) + (\frac{1}{2}i\beta_2 z - \frac{1}{2}\sigma^2)(\omega-\omega_0)^2}. \tag{2.20}$$

The signal of the lock-in amplifier is found by taking the inverse Fourier transform of this equation:

$$V_{LIA,complex}(\tau,z) \propto \frac{A_{ref}A_{sig}\sigma^2}{2\sqrt{\sigma^2-i\beta_2 z}}\mathrm{e}^{-\frac{1}{4}\sigma^2\Delta\omega^2+i\beta_0 z-i\omega_0\tau-\frac{(\tau-\frac{i}{2}\Delta\omega\sigma^2-\beta_1 z)^2}{2\sigma^2-2i\beta_2 z}}. \quad (2.21)$$

With the assumptions that $\Delta\omega \ll 1/\sigma \ll \omega_0$ and the timescale of τ is much larger than $\Delta\omega\sigma^2$, equation 2.21 can be simplified to

$$V_{LIA,complex}(\tau,z) \propto \frac{A_{ref}A_{sig}\sigma^2}{2\sqrt{\sigma^2-i\beta_2 z}}\mathrm{e}^{i\beta_0 z-i\omega_0\tau-\frac{(\tau-\beta_1 z)^2}{2\sigma^2-2i\beta_2 z}} \quad (2.22)$$

In this equation τ represents the delay time set by the delay stage in the reference branch and z is the propagation distance through the dispersive medium. Both variables change the phase of the measurement signal. The phase increases as the delay time increases, while the phase decreases as the distance z increases. The third term in equation 2.22 also contains a complex value, and describes the frequency chirp of the detected interferogram.

To determine the envelope of the interference, the absolute value of $V_{LIA,complex}(\tau,z)$ is calculated. Using equation 2.22, the LIA signal becomes

$$|V_{LIA,complex}(\tau,z)| \propto \frac{A_{sig}A_{ref}\sigma^2}{2\sqrt[4]{\sigma^4+\beta_2^2 z^2}}\exp\{-\frac{\sigma^2(\tau-\beta_1 z)^2}{2\sigma^4+2\beta_2^2 z^2}\}. \quad (2.23)$$

The term in the exponent contains $\tau-\beta_1 z$, ensuring that the movement of the interference envelope in space as a function of delay time has the same group velocity ($v_g \equiv 1/\beta_1$) as the actual propagating pulse in the photonic structure. This correspondence also allows a measurement of the group velocity, as is demonstrated in section 2.4.4.

Assuming that the propagation distance z through the photonic structure is small, the factor before the exponent reduces to $A_{sig}A_{ref}\sigma/2$, implying that the signal level increases with an increase of the pulse width σ, which can be understood by realizing that the amplitudes A_{sig} and A_{ref} are the peak amplitudes. If the width increases, the energy in each pulse increases, and therefore also the time-averaged intensity and signal level. On the other hand, if the pulse in the signal branch is broadened due to dispersion, the factor $\beta_2 z$ is no longer zero and the signal level goes down.

The term in the exponent describes the pulse shape. In the absence of dispersion, the term reduces to $\tau^2/(2\sigma^2)$. Compare this reduced term to equation 2.14, which describes the field of a Gaussian pulse. The width of the interference envelope is always a factor of $\sqrt{2}$ broader than the actual width of the E-field. In fact, the width of a laser pulse is usually expressed as the width of the intensity of a pulse. In that case, the interference width is, in the absence of dispersion, twice as broad as the intensity width of the used laser pulses. In the case dispersion is non-negligible, $\beta_2 z$ is non-zero, the pulse broadens as does the interference width.

In the experiments on the ridge waveguide as described in section 2.4, femtosecond laser pulses were used with a FWHM of the intensity spectrum of 9 nm, which corresponds to a FWHM of the pulse intensity in time of 107 fs. In a medium with a group index of 2.08 ± 0.03 (from measurement), the pulse width in space should be 15 μm. Using equation 2.23, this length results in an interference envelope that is twice as broad as the intensity width. The interference width in figure 2.5a is 31 μm, which corresponds perfectly to the expected 2×15 μm$= 30$ μm when taking into account the small inaccuracy in the determination of the spectral width. The group velocity dispersion is therefore expected to be low in the ridge waveguide.

2.5.2 The influence of higher order dispersion

In the interferometric near-field set-up, there are two methods to change the length of the interferometer branches: through the probe position z, which is changed by scanning the probe and though the delay time τ by moving the delay line. These methods provide the two options of performing a time-resolved near-field measurement: either scanning the probe (change z and keep t fixed) or scanning the delay line at a fixed position z of the probe and thus changing τ. In the first option, the probe picks up light at various positions z. While in this measurement option one has to realize that the accumulated dispersion in the signal branch is a function of z: while the pulse probed at position z may be Fourier limited, a pulse picked up at a position further along the structure ($z + \Delta z$) may be significantly dispersed. The analysis of a 'snapshot' of a pulse in a structure with strong dispersion therefore becomes more complicated, especially when higher order dispersion (β_3 or higher) plays a role.

If one is interested in the shape of the pulse, or the change of pulse shape upon propagation, it is more suitable to scan the delay line. In this way, the temporal information of the pulse is recovered at a single position. Repeating the experiment at different positions can then reveal the changes in shape of a pulse upon propagation, and makes the quantification of the dispersion more straightforward.

To model an experiment where pulses experience higher-order dispersion, on needs to evaluate equation 2.19, which can be rewritten as

$$V_{LIA}(\tau, z) \propto \mathcal{F}^{-1}[\, |\tilde{E}_{ref}(\omega)|\, |\tilde{E}_{sig}(\omega)| \mathrm{e}^{ik(\omega)z}\,]. \tag{2.24}$$

This equation can still be solved analytically, as long as $k(\omega)$ can be described by a second-order polynomial (i.e., $\beta_j \backsimeq 0$, for $j > 2$). We have demonstrated this possibility in the previous section. If also higher-order dispersive terms play a role, it is more convenient to evaluate equation 2.24 numerically. In chapter 6, we will show that we can use this numerical evaluation to describe the effects of higher-order dispersion on the propagation of femtosecond pulses in photonic crystals.

2.6 Conclusions

Phase-sensitive and time-resolved near-field investigations can be performed by integrating a near-field microscope into an interferometer. The heterodyne interferometer used in this thesis allows the recording of the optical field picked up by the near-field probe with average intensities down to the fW regime. For a time-resolved investigation of linear propagation phenomena it is not necessary to use an ultrafast femtosecond laser system. Any light source with a bandwidth of several (tens of) nanometers would be sufficient.

Time-resolved near-field investigations were performed using the interferometric near-field set-up on a ridge waveguide. We demonstrated how to determine the phase velocity in the waveguide and found a velocity of $1.75 \cdot 10^8$ m/s. We also measured the group velocity in the waveguide using the time-resolved measurements and found a value of $1.44 \pm 0.02 \cdot 10^8$ m/s. Materials with a very strong dispersion can show pulse deformation within the size of the scan area. In that case, it is still possible to extract dispersive properties like group velocity dispersion and higher-order dispersion. We have shown how to calculate the effects of only group velocity dispersion on the measurement result. In addition, we discussed how to model an interferometric experiment when also higher-order dispersion plays a role.

3 The evanescent field of a Bloch wave

We have measured the three-dimensional distribution of the evanescent field above a nanophotonic structure, a photonic crystal waveguide. The periodic structure of the photonic crystal causes the propagating waves to be governed by Bloch's theorem: they are composed of multiple wavevectors or harmonics. The Bloch character of the light has a profound influence on its evanescent field. We found, by measuring the field with phase-sensitive near-field microscopy, that the evanescent field of the composite Bloch wave decays non-exponentially as a function of height. Even the individual Bloch harmonics, having only a single wavevector, do not necessarily decay single-exponentially. This effect has its origin in the intricate in-plane field distribution of each harmonic. The complex decay leads to an evolution of the mode pattern as a function of the height above the structure. Our experimental results are confirmed with calculations.

3.1 Introduction

Sir Isaac Newton was the first to report on the evanescent field. He observed frustrated total internal reflection and concluded from his measurements that the evanescent field extends approximately "ten hundred thousandth Part of an Inch" (25 nm).[56] The evanescent field is exploited for a broad range of applications, ranging from coupling of light in and out of structures,[57] to two-dimensional Bose-Einstein condensation,[36] sensing[35] and microscopy.[58]

The text book example of an evanescent wave is that of total internal reflection. In this

simple case, an the evanescent field will be present at the planar interface into a low-ϵ material with an optical field amplitude decaying exponentially as a function of height z above the interface:

$$E(z,t) = E(0,t)\mathrm{e}^{ik_\perp z}, \tag{3.1}$$

where the wavevector in the low-ϵ material perpendicular to the interface ($k_\perp$) is

$$k_\perp = \sqrt{\epsilon_{low}\frac{\omega^2}{c^2} - k_\parallel^2}. \tag{3.2}$$

The optical frequency is denoted as ω and c is the speed of light in vacuum. For evanescent waves, the wavevector in the high-ϵ region, parallel to the interface ($k_\parallel$), must be larger than the maximally allowed wavevector in the low-ϵ material for that ω. In this case, $k_\perp$ is imaginary and therefore the wave is exponentially decaying away from the interface. The above equation holds for flat planar interfaces but not only for total internal reflection but also for, amongst others, light propagating in thin slabs of material, or surface waves like surface plasmon polaritons. The evanescent field of periodically patterned surfaces may differ however.

An intriguing class of periodically structured optical materials are photonic crystals, in which materials with a high and a low dielectric constant (ϵ) are arranged in a lattice. The periodic structure greatly affects the dispersion of the propagating light.[6] In certain geometries, a photonic bandgap may exist[23] and low group velocities of propagating light[18,19] have been reported.

Light in a photonic crystal, must obey Bloch's theorem, which dictates that the amplitude of a wave must conform to the imposed periodicity.[24] For a wave in periodic structure, with a periodicity along y, the resulting wavefunction ψ in the y-direction can be described as

$$\psi(x,y,z) = u_k(x,y,z)\exp(iky), \text{ where } u_k(x,y,z) = u_k(x,y+a,z). \tag{3.3}$$

The above equation describes that the Bloch wave, with wavevector k, has a periodic amplitude modulation u_k, with the same period (a) as the lattice. We can rewrite equation 3.3 as a Fourier series of waves:

$$\psi(x,y,z) = \sum_m a_m(x,z)\exp(i(k+m\frac{2\pi}{a})y), \text{ where } m \in \mathbb{Z}. \tag{3.4}$$

The individual partial waves that together make up the Bloch wave, each have an amplitude a_m. Their wavevector is k plus an integer (m) number of the reciprocal lattice period $2\pi/a$. The partial wave with the largest amplitude is defined as the fundamental with $m = 0$ and the partial waves with $m \neq 0$ are the Bloch harmonics. The two equivalent descriptions in equations 3.3 and 3.4 may, at first glance, give rise to some confusion concerning the expected decay of the evanescent field in a two-dimensional periodic structure. Based on equation 3.3, one might naively expect an exponential decay governed by the magnitude

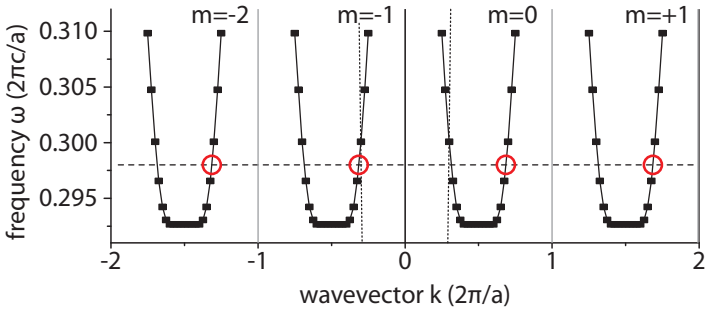

Figure 3.1: Portion of the dispersion relation of the photonic crystal waveguide under investigation, obtained via 3D FDTD simulations (solid squares). The solid lines are guides to the eye. An excited Bloch mode at ω=0.298 has multiple wavevectors (encircled intersections), spaced $(2\pi/a)$ apart. The vacuum mode (or light line, $\omega = ck$) is depicted with the dotted line.

of k, when assuming that $k = k_{\|}$ (see equation 3.2). The multiple partial waves in equation 3.4 however, suggest that the decay is multi-exponential.[59]

In this chapter, we have investigated the evanescent field above a two-dimensional photonic crystal waveguide with three-dimensional near-field microscopy. We will show both with experiments and calculations that both the Bloch nature of the guided light but also the confinement of light in a narrow waveguide, has a profound effect on the evanescent field above the structure. We find a highly complex decay behavior. As a result, also the field patterns above the structure strongly evolve with height.

3.2 Recovering the Bloch harmonics

The photonic crystal structure we investigated, is a 200-nm thick air-bridge membrane of Si. In the membrane, we etched a hexagonal lattice (period $a = 456$ nm) of air holes (radius 140 nm). A single row of holes is not perforated and acts as a waveguide. Figure 3.1 shows a portion of the calculated dispersion relation of the waveguide under investigation. The encircled intersections indicate the wavevectors, each spaced $2\pi/a$ apart, that together form the Bloch wave, that are excited at a specific optical frequency (ω=0.298, dotted line). Note that the non-encircled set of wavevectors at the intersection of the dotted line and the dispersion curve corresponds to backward propagating light, since the (sign of the) slope of the dispersion relation determines the (direction of the) group velocity.

We measured the optical field above the structure with a phase-sensitive near-field microscope.[55] By scanning a metal-coated tapered optical fiber over the structure, we obtain a map of the optical field above the structure. By incorporating the scanning setup in a

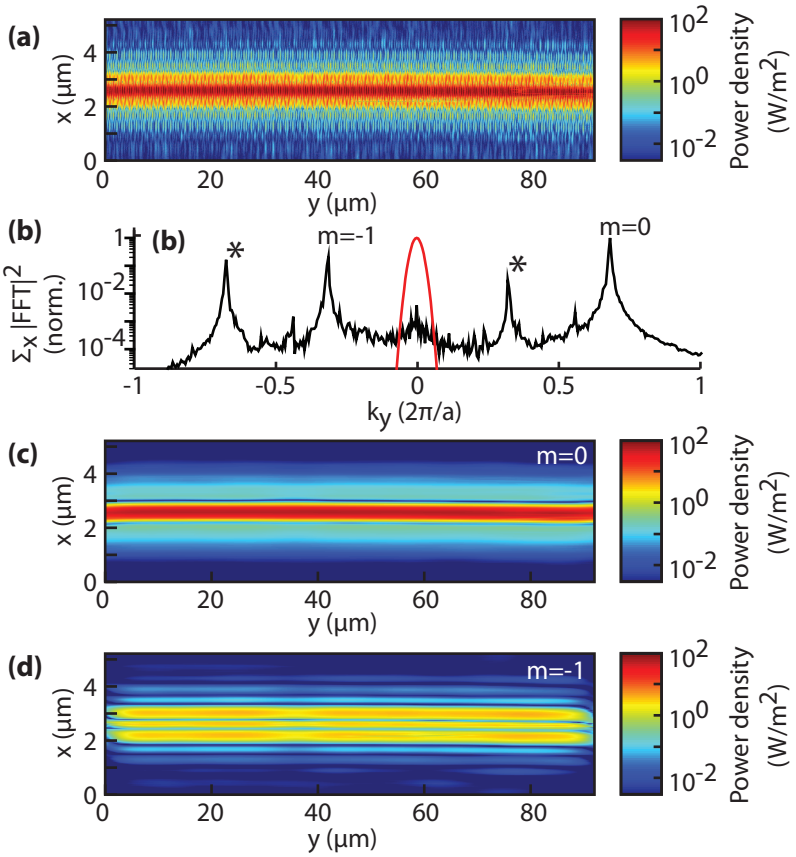

Figure 3.2: (a) Colorscale (logarithmic) image of the measured power density distribution. The waveguide is centered along the $x = 2.6$ μm line. (b) Power spectrum of the k_y wavevectors present in the structure, obtained via Fourier transforming the complex phase-sensitive E-field distribution underlying (a). Two Bloch harmonics are visible ($m = -1$ and $m = 0$) and two wavevectors of the reflected Bloch wave ($*$). The red line depicts the window of the Fourier filter (not necessarily at $k_y = 0$), used to extract the power density distribution of the fundamental and $m = -1$ harmonic, respectively (c,d), obtained via Fourier filtering the complex phase-sensitive E-field distribution underlying (a).

heterodyne interferometer, we recover the electric (E-)field amplitude and phase locally. The diameter of the probe aperture is 200 nm and determines, on first approximation, the detection area of $3.1 \cdot 10^{-14}$ m^2. The collected power by the probe is expressed as a power density in units W/m^2. Figure 3.2a shows the power density of the field, at ω=0.298 where the waveguide is located in the center of the image, with the light propagating through it from left to right. In this measurement, the distance of the probe to the sample is kept constant at 10 nm. The measurement clearly shows that the light is confined to the waveguide, centered along the line $x = 2.6$ μm.

By Fourier transforming the measured complex field along the direction of the waveguide (y-direction), we retrieve the periodic components of the field: the wavevectors k_y.[60] Figure 3.2b shows the power spectrum obtained by summing the square of the amplitude of the Fourier transforms for all x values. In agreement with the dispersion relation shown in figure 3.1, we find peaks at $k_y = 0.68 \pm m$ in normalized units of $2\pi/a$, with m being an integer. Also at $k_y = -0.68 \mp m$ peaks are found, indicated by the asterisks in figure 3.2b, which correspond to light that is reflected at the end facet of the waveguide.

In order to recover the spatial distribution of each Bloch harmonic, we applied a Fourier filter to the complex field data underlying figure 3.2a. Figure 3.2c shows the Fourier filtered data, with a Gaussian selection window centered around $k_y = 0.68$ and with a width of 0.02, corresponding to the $m = 0$ (or fundamental) Bloch harmonic. The same filter is applied for the $m = -1$ harmonic ($k_y = -0.32$), of which the results are depicted in figure 3.2d. Since both results are obtained by filtering the data underlying figure 3.2a, we expect a similar distribution as in 2a. For the fundamental wavevector the distribution is indeed similar: the power density is highest in the center of the image, around $x = 2.6$ μm, and the width is similar to the raw data. The power density distribution of the $m = -1$ harmonic is however more extended into the crystal region. We attribute this difference to the intricate modal pattern of the composite Bloch wave. The amplitude modulation of the Bloch mode is much stronger near the crystal region than in the center of the waveguide, i.e., (more) harmonics need to be added to the fundamental wave to obtain this modulation.[60]

3.3 Decay of the harmonics

To determine the decay of the evanescent field above the photonic crystal waveguide, we performed a series of measurements, where the distance of the probe to the sample z increases with increasing y. In this way, we obtained a controlled increase in height of approximately 400 nm in a single scan. A series of these scans yielded a total height range of 2 μm. Using the same Fourier filtering procedure as describe above, we calculated the power density for each height. We used appropriate Fourier filtering (see above), to recover the power density for the harmonics with $m = -2,\ -1,\ 0$ and $+1$. Each of these harmon-

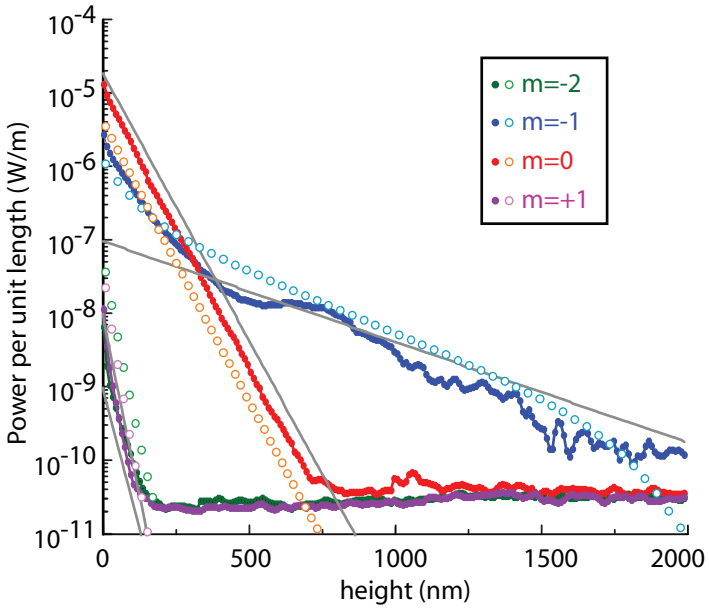

Figure 3.3: Measured power in each of the Bloch harmonics as a function of probe-sample height z for four harmonics (see legend). Both the measurement results (solid dots) and the 3D FDTD results (circles) are shown. The grey lines indicate the decay expected based on equations 3.1-3.2 and are offset for clarity.

ics can have a different lateral power distribution (the amplitudes a_m are allowed to depend on x). We therefore integrated over the distribution perpendicular to the waveguide, to obtain the power per unit length of waveguide. The result is depicted in figure 3.3, showing the power as a function of height.

Perhaps surprisingly, the curves show that each harmonic decays with a different slope as the height increases, until the curves level off at a power per unit length of $\sim 3{\cdot}10^{-11}$ W/m, where the noise level of the analysis is reached. The harmonics with the largest wavevectors ($m = -2$ and $m = +1$), have the strongest decay ($k_\perp \approx 20i$ μm^{-1}), whereas the harmonic with the smallest wavevector ($m = -1$), decays very slowly as a function of height ($k_\perp \approx 2i$ μm^{-1}). The ensemble of these harmonics together form the Bloch wave. Adding the harmonics of figure 3.3 yields a decay that is dominated by the fundamental harmonic close to the surface ($z < 250$ nm), but at larger distances ($z > 500$ nm), the $m = -1$ harmonic dominates. Obviously, the Bloch wave itself, which is composed of these harmonics, therefore does not exhibit a single exponential decay.

The differences in decay can be understood by considering equations 3.1-3.2, since each harmonic has a different wavevector $k_\parallel$, the decay must consequently also differ. Since

the parallel wavevectors of the $m = -2$ and $m = +1$ harmonic are much larger than the low-ϵ wavevector (air), their decay is rapid. The $m = -1$ harmonic on the contrary, which has a wavevector very close to the vacuum wavevector, decays much more slowly. The decays expected based on equations 3.1-3.2 are depicted with the solid lines. Equations 3.1-3.2 do not fully describe the measured decays. In particular, a strong deviation is found for the $m = -1$ harmonic: between 0 and 400 nm, the experimentally found decay is much stronger and more complex than a single exponential decay expected based on equations 3.1-3.2.

We have performed 3D finite-difference time-domain (FDTD) simulations [‡] to validate our experimental results and to confirm the deviation from a single-exponential decay. We applied a similar Fourier analysis to the FDTD data to resolve the individual Bloch harmonics. Comparing the measured and simulated result in figure 3.3, we conclude that there is qualitative agreement between FDTD results and experiment. There are some differences in relative amplitude between the harmonics, which we attribute to the wavevector dependent coupling to the near-field probe.[61] In the z region between 1500 and 2000 nm, the edge of the simulation window is approached and the decay is more rapid as a result of numerical errors.

Key to the full understanding of the complex decay of the Bloch harmonics and the composite Bloch wave are the lateral modal profiles (perpendicular to the waveguide direction) as a function of height. We have plotted the experimental and simulated results for the fundamental harmonic in figures 3.4a and 3.4b, respectively. The results are clearly in good agreement: the fundamental profile shows a maximum in the center of the waveguide at $y = 2.6$ μm, and a decay in the crystal region. The evanescent field has nodes (arrows in figure 3.4b), with fields with opposite signs on either side, as is indicated by '+' and '-'. On close examination, one can observe that the field profile broadens as the height is increased, since the nodes in figures 3.4a and 3.4b shift outward: the mode pattern changes as a function of height. The broadening is quite in contrast to what one would naively expect based on equations 3.1-3.4. Following these equations, the evanescent field for light propagating in the y direction would only be decreasing as a function of height, but the mode pattern (in the x direction) would not be affected.

We observe even stronger pattern changes in the evanescent field of the $m = -1$ harmonic in figures 3.4e and 3.4f, for the experimental and FDTD simulation results, respectively. In both images, the modal pattern is more complex than in figures 3.4a and 3.4b. In figure 3.4f, several nodes are visible at a height of 200 nm, due to alternating positive and negative field values. As the height is increased, the pattern changes gradually, until only a smooth profile without nodes remains at a height of 1000 nm.

Both the observation of the changes in modal pattern in the images in figures 3.4 as well as

[‡] 3D FDTD simulations were performed using a unit cell of $23 \times 267 \times 210$ pixels ($x \times y \times z$), corresponding to $1 \times 11.6 \times 9.1$ lattice periods, with absorbing boundaries for y and z and periodic boundaries for x.

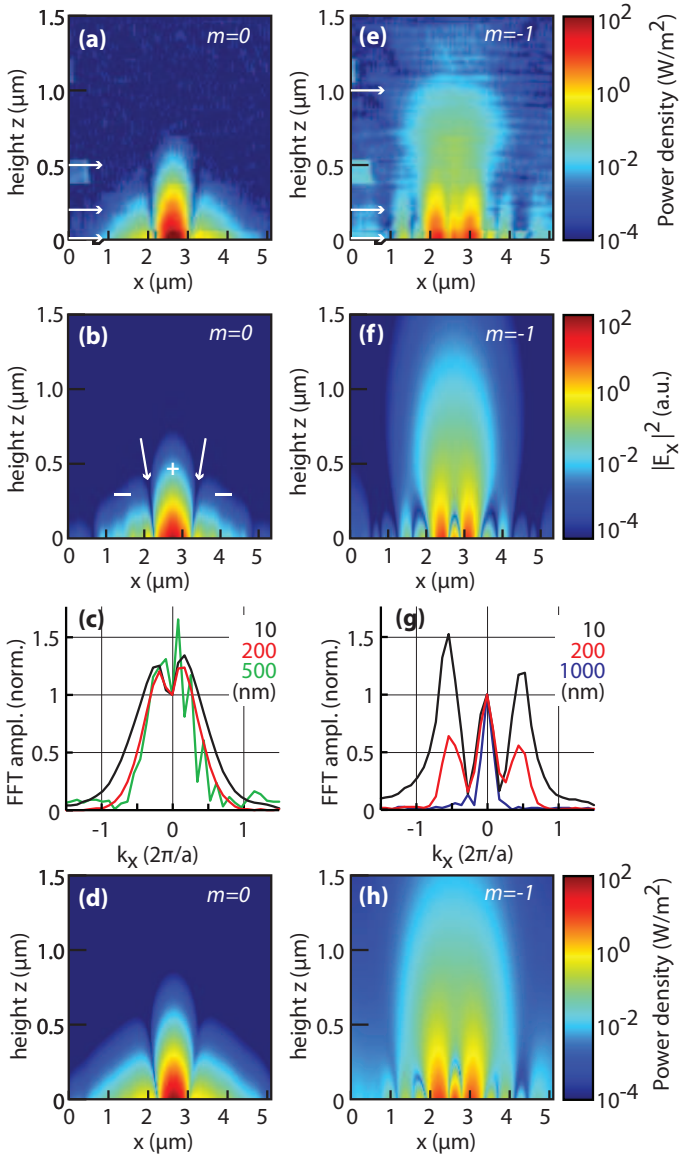

Figure 3.4: (a,b) Power density distribution of the fundamental harmonic as a function of height, measured (a) and from FDTD simulation (b). (c) Amplitude of k_x wavevectors obtained via Fourier transformation of the lateral field at heights indicated by the arrows in (a), normalized to the amplitude at $k_x = 0$. (d) Calculated power density distribution by including the decay of k_x wavevectors, using the measurements at 10 nm as a starting point. (e-h) Same as (a-d) for the $m = -1$ Bloch harmonic.

the non-single-exponential decay of the $m = -1$ harmonic seen in figure 3.3 deviate from the single exponential decay suggested by a naive interpretation of equations 3.1 and 3.2. The explanation for the deviations from this simple behavior lies in the lateral fields of the harmonics. The lateral fields are not only confined to a narrow waveguide, but also have a complex lateral modal pattern. To build up these modal patterns, a range of k_x wavevectors is required.

If the magnitude of the k_x wavevectors is comparable to or larger than that of k_y, they need to be taken into account when calculating the decay or the modal pattern of the evanescent field. By substituting $\sqrt{k_x^2 + k_y^2}$ for $k_\parallel$ in equation 3.2 we obtain

$$k_z = \sqrt{\frac{\omega^2 \epsilon_{low}}{c^2} - k_x^2 - k_y^2}. \tag{3.5}$$

The k_x wavevectors that make up the lateral patterns are calculated via Fourier transforming the fields. The results are depicted in figures 3.4c and 3.4g for the fundamental and $m = -1$ harmonic, respectively. In both figures, the higher k_x values vanish more rapidly as the height increases compared to the amplitude of the wavevectors closer to zero. Due to the broad range of k_x wavevectors in the waveguide, the decay of even a single Bloch harmonic is not a single exponent, but a multi-exponential decay. By including the k_x wavevectors in the calculation on the field decay, see equation 3.5, we obtain an excellent agreement with the measured field decay and modal patterns, as can be seen in figures 3.4d and 3.4h. In these figures, the field decay is calculated using the measured field distribution at 10 nm height above the structure.

3.4 Discussion and conclusions

The above analysis is performed for the evanescent decay of the E_x field only. In the near-field experiment, we were primarily sensitive to the E_x field and in the analysis of the 3D FDTD data we selected the x component of the field. If the experiment and the analysis would be performed for the E_y-field, the results are expected to be analogous, although the exact field patterns would differ from the E_x field. We were able to confirm the analogy and therefore also the validity of using Eq. 3.5, for the E_y field in the FDTD simulation.

In conclusion, we have investigated the decay and pattern changes of the evanescent field above a photonic crystal waveguide. Two effects were found that influence the subwavelength pattern and decay of the field. First, the Bloch nature of the propagating mode, which creates an ensemble of wavevectors (k_y), each with their own decay constants, plays an important role. Secondly, the strong confinement of the light in the narrow waveguide plus the intricate lateral mode profile resulting from the neighboring photonic crystal lattice, requires a broad range of wavevectors (k_x) perpendicular to the direction of propagation. The influence of the wavevectors in the x direction results in strong changes of the modal

pattern as a function of height above the photonic crystal waveguide, which were found in both near-field experiments and 3D FDTD simulations.

Both the measurements and the simulations show that nanostructured optical materials can have rich evanescent field patterns. This property may be exploited by engineering the geometry such that a specific (subwavelength) evanescent field pattern is obtained, by tuning the k_x wavevectors. Tailored evanescent field patterns may, for example, be exploited in optical trapping or manipulation of nanoparticles or Bose-Einstein condensates. Promising results have already been demonstrated for tuning of the k_y wavevectors in so-called dispersion engineering in photonic crystal waveguides.[54,62]

4

Measuring the local dispersion relation

A dispersion relation relates wavevector to frequency for infinitely large structures. Here we show that we can also assign a wavevector in a useful manner to light interacting with a finite-sized structure with a length of less than ten times the wavelength. We call the corresponding relation between wavevector and frequency the local dispersion relation. We have analyzed a so-called chirped photonic crystal waveguide in which the hole radius of the photonic crystal lattice gradually increases, which results in a dispersion relation that is position dependent. With a phase-sensitive near-field microscope we have mapped the amplitude and phase of propagating light in the waveguide. By Fourier analysis of the complex field measured, we recovered the spatial frequencies, which can be considered as the local wavevectors, contained in the light field in a region of 38 lattice spacings. We show that if the length of the analyzed region is increased the wavevector resolution increases, at the expense of local information however. Our measurements show that the local dispersion relation shifts to higher frequencies as the hole radius increases.

4.1 Introduction

One of the strengths of photonic crystal[6] structures is the engineering of the dispersion relation of light. This offers unprecedented possibilities for exploiting slow light in photonic crystals,[18] as integrated optical buffers[63] or for dispersion compensation.[64] Photonic crystals that exploit slow light modes may open new possibilities for integrated photon-

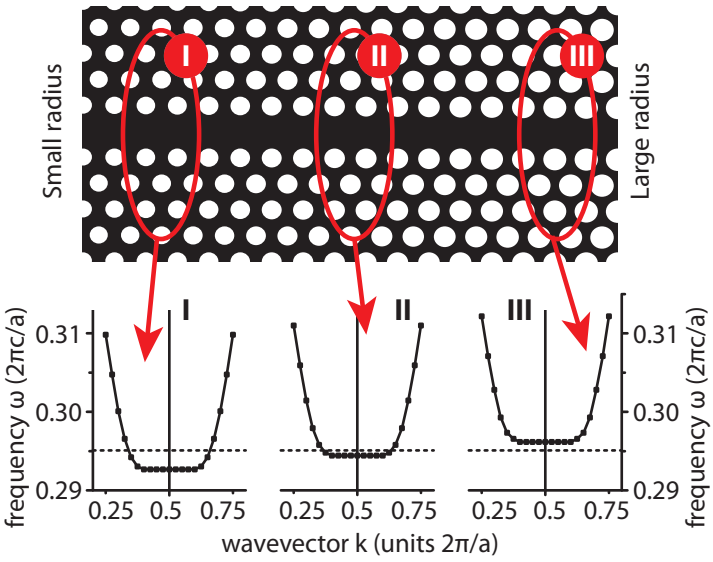

Figure 4.1: Schematic representation of a chirped waveguide (top). The radius of the holes in the PhC lattice is linearly increased from left to right. The dispersion relation (bottom) depends strongly on the radius of the holes: the waveguide mode (continuous line) in the dispersion relation shifts up as the hole size increases. Light with optical frequency $\omega = 0.295$ (dotted line) is therefore allowed to propagate in regions I (with a relatively high v_g) and II (lower v_g), but not in region III. The dispersion relations are calculated by 3D FDTD for hole radii of 0.306·a, 0.314·a and 0.321·a, respectively.

ics, for example using enhanced nonlinear interactions, due to slow light, for all-optical switching.[20] Such novel photonic crystal structures will be composite structures, with each component having different optical properties. Smart combinations of photonic crystal components can create polarization filters,[65] frequency filters[42] and all-optical switches.[66]

The (linear) propagation properties of the individual components are usually expressed in the dispersion relation, which relates wavevector to frequency.[2] A dispersion relation assumes that the photonic structure is infinitely large. However, also in an area of finite dimensions, a dispersion relation can be useful to describe propagation properties. The dispersion relation of only a small area, we call the local dispersion relation.

4.2 Chirped waveguides

It is also possible to change the local dispersion relation gradually as a function of position. In such structures, the wavevector becomes a function of position. The most used example

of such a concept is the chirped waveguide, in which the dispersion relation is gradually shifted as a function of position.[67] In these chirped waveguides, impedance mismatch losses are overcome and thus the gradual shift allows efficient coupling to modes with a low group velocity.[68]

Here we investigated the local dispersion relation of a so-called chirped photonic crystal waveguide. In this waveguide, the radius of the holes is linearly increased with position. As a result, the local dispersion relation will shift up in frequency as a function of position. By measuring the propagating optical wave using a phase-sensitive near-field microscope, we were able to determine the local dispersion relation directly from the measured spatial frequencies contained in the light field as a function of optical frequency. We show that the local dispersion relation indeed shifts as a function of position. The analysis is performed by retrieving the wavevectors in a small section of waveguide. We have included a detailed discussion on what the influence of the size of the analyzed section is on determination of the local dispersion relation.

Figure 4.1 shows a schematic of the photonic crystal waveguide (PhCW) under investigation. A PhCW is created by removing a single row of holes in the photonic crystal lattice. This so-called W1 waveguide has already been studied in great detail.[21,32] From left to right the hole radius is gradually increased. A portion of the dispersion relation is shown in figure 4.1, for different sections of the PhCW, calculated by 3D FDTD calculations. In these calculations, each section is treated as if it were infinitely long. In each section, the waveguide mode flattens as the wavevector approaches the Brillouin zone boundary at $k = 0.5$, corresponding to a decrease of the group velocity (v_g), until it reaches a zero v_g at the Brillouin zone edge. Due to the change in hole radius, the dispersion relation shifts. An increasing hole size leads to a shift of the dispersion curve to higher frequencies. As a result, light with a certain optical frequency (dashed line) is allowed to propagate in region I, where the hole radius is still small. In region II, the local dispersion relation has shifted due to the larger hole radius, but light is still allowed to propagate. In region III, the local dispersion relation has shifted that much, that there is no propagating mode allowed for the specified frequency. The group velocity varies in the different regions, as v_g is equal to the slope of the local dispersion relation. In region II the slope is less steep than in region I, resulting in a decrease of the group velocity. Since the change in hole radius in a chirped waveguide is gradual, the change in group velocity will also be gradual. The reduction of the group velocity will continue until the waveguide no longer allows propagation. At this so-called cut-off, the light will be reflected back towards the input, or will be scattered out-of-plane.

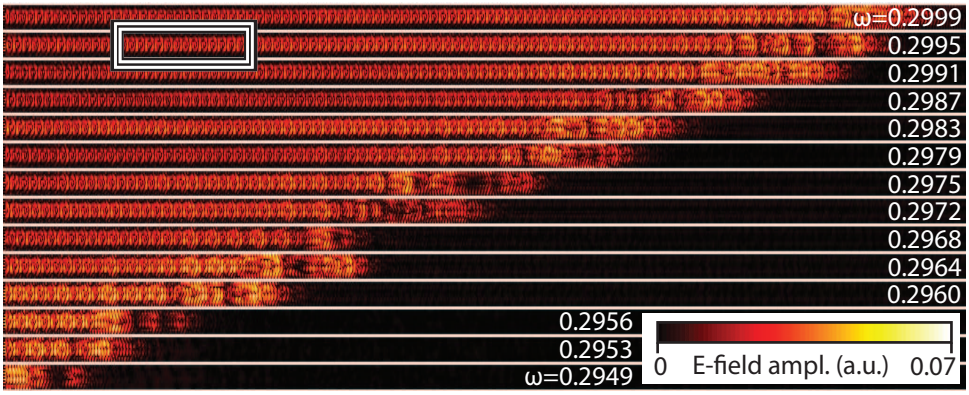

Figure 4.2: Measured amplitude of the optical field of the chirped waveguide at frequencies ranging from $\omega = 0.2999$ (top, 1534 nm) to $\omega = 0.2947$ (bottom, 1561 nm). Each image represents a measurement of the same area of the same chirped waveguide, only the frequency differs. Scan area: $139 \times 2.3\mu m^2$. The position where the light stops propagating depends strongly on the optical frequency. As the frequency increases, the light can propagate further in the waveguide. The rectangle on the top left represents the frequency and position of the measurement shown in figure 4.3.

4.3 Recovering the wavevectors

We investigated the propagation of light through such a chirped waveguide that was fabricated in a 210 nm thick silicon membrane with a hexagonal lattice of air holes with a 456 nm period (a). The hole radius increases from 142 nm to 150 nm over a length of 300 lattice periods. The optical field inside the waveguide was probed using a phase-sensitive near-field microscope.[55] In this microscope, we scan a near-field probe over the sample at a height of approximately 10 nm. A small portion of the field in the sample couples to the probe. We interferometrically mix the light picked up by the near-field probe with a reference beam from the same continuous laser source. The resulting interference signal is proportional to the electric field (E-field) amplitude of the light from the near-field probe and the E-field amplitude of the reference light, which is constant. The relative phase between the two E-fields also determines the measured interference signal. The resulting measurements, obtained by the near-field microscope therefore represent the amplitude (A) of the E-field in the waveguide and the detected phase (ϕ) of the light, since the reference field is kept constant.[69,70]

In figure 4.2, we show the amplitude of the E-field in the chirped PhCW of a 139×2.3 μm^2 area. Each image represents a near-field measurement of the same area, measured at different optical frequencies. The frequency decreases from top to bottom. The light is coupled into the PhCW from the left using end-fire coupling. The facet of the waveguide is located

only a few microns to the left of the left edge of the scan area. We observe that the light propagates until it reaches a certain position in the waveguide. The position at which the light stops propagating depends on the optical frequency. Light with a frequency of 0.2999 (in normalized units of $2\pi c/a$) will propagate through most of the scanned area, whereas light with a frequency of 0.2949 is stopped after only a few microns of propagation. The cut-off position x shows a linear dependence on frequency of $\Delta x/\Delta\omega$ of 2.6 mm using normalized frequency units or a $\Delta x/\Delta\lambda$ of 5 μm/nm, with λ being the vacuum wavelength of the laser light.

There are some deviations from the linear trend. For example, in the measurement at $\omega = 0.2968$, the light stops propagating before the expected point based on the linear trend. At $\omega = 0.2964$, the cut-off position exceeds the expected trend. We attribute these observations to irregularities in the structure. Note that the design gradient of the radii is only 0.03 nm per period, which is significantly below the fabrication accuracy of the e-beam lithography. From an analysis with electron microscopy, we estimate the variation in the hole radii to be around 1 nm. The variations can cause an undesired reflection of the light by backscattering. This effect is much stronger in the slow-light region[39] than in the rest of the waveguide, and will result in a reflection of the light before it has reached its theoretically attainable lowest group velocity. Alternatively, the variations in hole radius may permit light to propagate in the region that would normally not allow modes for that specific frequency. Both processes combined explain the irregular pattern observed in the cut-off region.

To validate that the change in local dispersion relation causes the limited propagation distance, we analyzed the near-field measurements in greater detail. Figure 4.3a shows the E-field amplitude data A of the area and frequency highlighted in figure 4.2. In figure 4.3b, we depicted an electron micrograph of a PhCW similar to the waveguide under investigation, with the same dimensions as in figure 4.3a. In figure 4.3a we see the details of the mode pattern as it is obtained by our microscope. The oscillations in the amplitude pattern are caused by the Bloch wave nature of the propagating light[71] plus the interference between the forward propagating and reflected light. Figure 4.3c, shows the corresponding real part of the measured complex optical field (Re($A \cdot e^{i\phi}$)). A line trace of the scan from left to right reveals consecutive maxima (white) and minima (black), due to the phase evolution of the optical field. The distance between to maxima represents a full cycle of the electric field. A Fourier transform of the complex E-field data recovers the periodic components of the E-field and therefore yields the wavevectors present in the waveguide.[60]

The image in figure 4.3c is built from multiple lines from left to right, that are all Fourier transformed. The summation of all these Fourier transforms results in the curve in figure 4.3d, which shows the amplitude of the wavevectors for a specific frequency and for a section of the chirped waveguide. Four peaks are clearly visible in this graph, corresponding to the wavevectors of the modes of the forward traveling light ($*$) and the reflected light ($\triangle$). Since the wave travels through a periodic medium, the wavefunction must conform

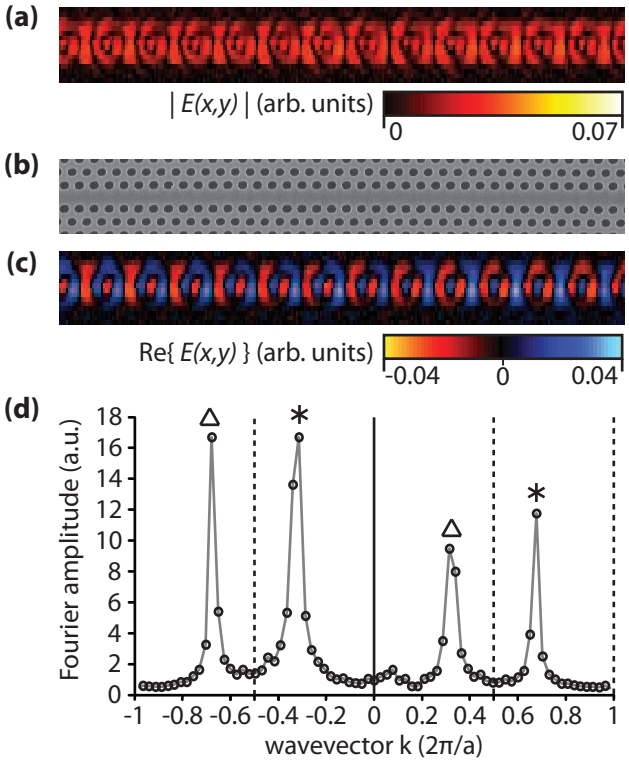

Figure 4.3: (a) Amplitude of the electric field measured with our near-field microscope at $\omega = 0.2995(2\pi c/a)$ *(*$\lambda = 1536$ *nm). (b) Scanning electron micrograph (of a portion) of the structure under investigation. (c) Corresponding real part of the measured electric field. Scan area (a-c):* $17.4 \times 2.3\mu m^2$*. (d) Fourier transform of the complex field data, revealing the wavevectors of the optical field of both forward propagation (*$*) and reflected light (*$\triangle$*). For each Bloch mode, two harmonics are visible. The dashed lines indicate the edges of the Brillouin zones.*

to the imposed periodicity and thus obey Bloch's theorem.[71] As a result, a single mode consists of multiple wavevectors, spaced $2\pi/a$ apart in k-space. The coherent superposition of these constituents yields a periodic amplitude modulation, with a period equal to that of the lattice. The $2\pi/a$ spacing can be observed in figure 4.3d, since a wavevector at $k = 0.68 \cdot 2\pi/a$ and a related Bloch harmonic at $k = 0.68 - 1 = -0.32$ in units of $2\pi/a$ are measured. These wavevectors correspond to forward propagating light, since the slope of the dispersion relation is positive at these values, see figure 4.1. The other two wavevectors at $-0.68 \cdot 2\pi/a$ and $0.32 \cdot 2\pi/a$ correspond to light reflected from the cut-off region and have a negative slope in the dispersion relation. The width of the peaks in figure 4.3d is determined by two factors. The length of the analyzed area determines the resolution of the Fourier transform, while the spatial frequencies found are the average over the area analyzed.

4.4 Frequency dependency

We performed the Fourier analysis for eight sections of the waveguide of equal length, that together form the entire measurement area of figure 4.2. In this way, we obtained the spatial frequencies of the propagating light in each section, or, in other words, the 'local' wavevectors. In addition, we performed this analysis for a range of frequencies, yielding the local wavevectors for each section as a function of frequency: the 'local' dispersion relation. The results are depicted in figure 4.4. All the local dispersion relations are qualitatively similar: the dominant mode has a steep slope at higher optical frequencies and flattens as the mode approaches the Brillouin zone edge. A clear shift of the local dispersion relation is observable as the hole radius increases. The total shift visible is 0.05 frequency units resulting in a shift of 0.0004 per μm. The observation of the flattening of the dispersion relation indicates that the light indeed couples to slower propagating light. If we determine the group velocity of the light based on the shallow slope of the dispersion relations, the v_g must be below $c/260$. The determination of this value is limited by the pixel resolution of the dispersion relation and may be even lower. In this case the v_g is based on 2 pixels in k and one pixel in ω.

We have measured the local dispersion relations with several near-field probes, both with a metal coating[72] and without, and found the same dispersion relations. From this observation, we conclude that the near-field probe has a negligible effect on the measurement of the local dispersion relation.

4.5 Discussion

At first glance, the measured dispersion relations appear to be a good match to the theoretic results in figure 4.1. On close examination of the measured dispersion relations, we

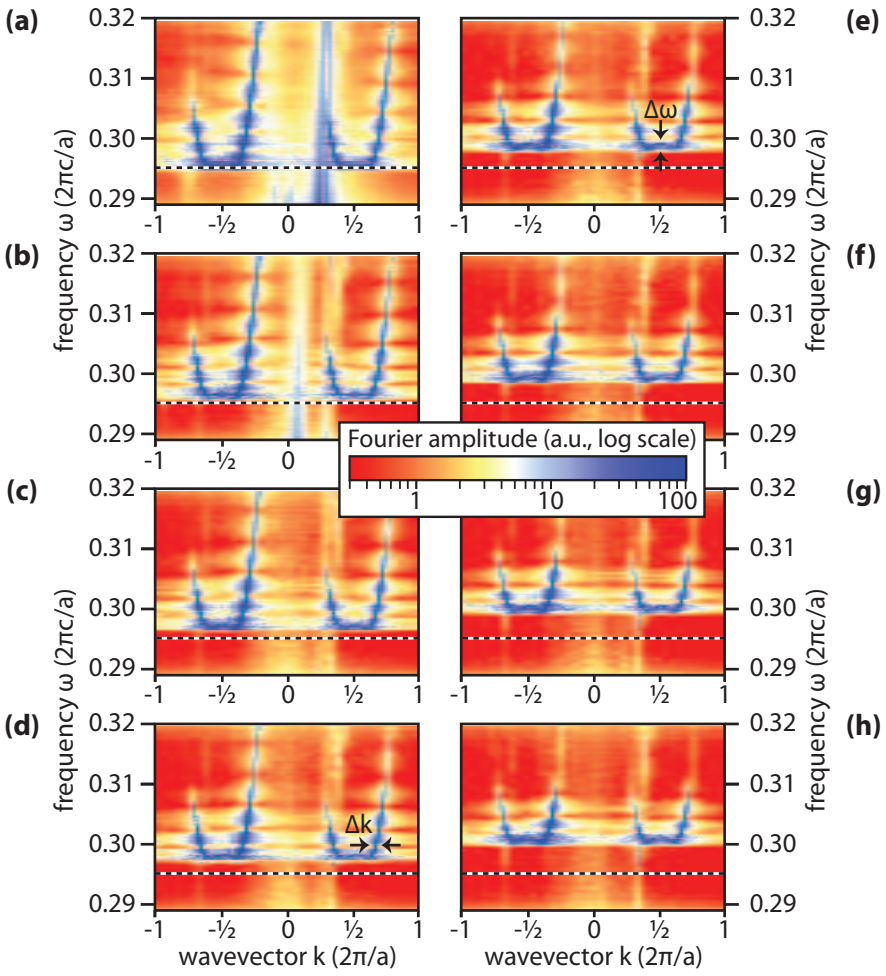

Figure 4.4: (a-h) Local dispersion relations of the chirped waveguide. The measured complex field is divided into 8 equal sections of $17.4 \times 2.3\mu m$ *of which the dispersion relation is determined. The most prominent band is the TE polarized waveguide mode. In (a) and (b), also the light line can be resolved. At greater distances from the entrance facet (d-h), a TM polarized mode can be discerned.*

observe however, that the measured curves are not strictly decreasing towards the edge of the Brillouin zone at $|k| = \pi/a$. Instead, the curves rise again around the zone edge, to form a 'w'-shape from $k = 0$ to $|k| = 2\pi/a$. The local maximum is especially well visible in figure 4.4e, between the arrows denoting $\Delta\omega$. We have not been able to determine what causes this shape of the dispersion relation. We know that the radius of the holes adjacent to the waveguide are on average 2% to 4% larger than the radius in the bulk, but the increased radius does not account for the 'w'-shape as observed in figure 4.3.[62] We also excluded the influence of the near-field probe as we explained in the previous paragraph. We did not find an explanation for the 'w'-shape by calculating the dispersion relation for infinitely long waveguides, without chirp. We can therefore not exclude that the deviating shape is a fundamental property of chirped waveguides as we used in this study.

The size of the measurement area for the analysis of the local dispersion relations in figure 4.4 may be varied. The choice for the length is a trade-off between resolution in wavevector and the size of the area from which the information is determined, which directly translates to the accuracy with which a change in dispersion as a function of position can be determined. To illustrate the size dependence, we have depicted the wavevector resolution versus analysis length L in figure 4.5a. The data plotted is taken at ω=0.299 and $k \simeq$0.7, which is depicted by the arrows in figure 4.4d. The resolution Δk is defined as the full width at half maximum (FWHM) of the Fourier transform. The spatial frequency resolution of a Fourier transform of a perfectly periodic quantity improves linearly with increasing size. However, here we found that it levels off at $L > 50a$ since such lengths are so large, that we observe the spread of wavevectors present in this large area, due to the chirp of the waveguide. The figure also shows an oscillation of the resolution. The oscillation is caused by a sampling effect of the Fourier transform, which prevents reaching the theoretically attainable resolution of $\Delta k = 1/L$. This effect can be suppressed by zero padding the data set, which artificially increases the number of points in the spatial frequency domain.

We observe a similar trend in figure 4.5b, where the width in frequency of the found band in the local dispersion relation is plotted versus the probed area. The resolution is obtained by evaluating the FWHM in frequency at k=0.5, which is depicted by the arrows in figure 4.4e. As the dispersion relation shifts further, the width of the band increases due to averaging over the larger area. At small L, the limited resolution in wavevector, also affects the band width in frequency. If the length increases, the measured frequency band reaches an optimum (low $\Delta\omega$), after which the shifting dispersion relation blurs the 'local' dispersion relation. At large L, we can hardly call the dispersion relation that is obtained a 'local' property, since the dispersion relation is an average over a large area.

The choice for the length used in the analysis is therefore a trade-off between frequency and wavevector resolution. The chirped photonic crystal waveguide investigated here, exhibited a relatively slow shift of the local dispersion relation as a function of position (see above). It is therefore an ideal structure to elucidate the type of analysis performed here. If the shift

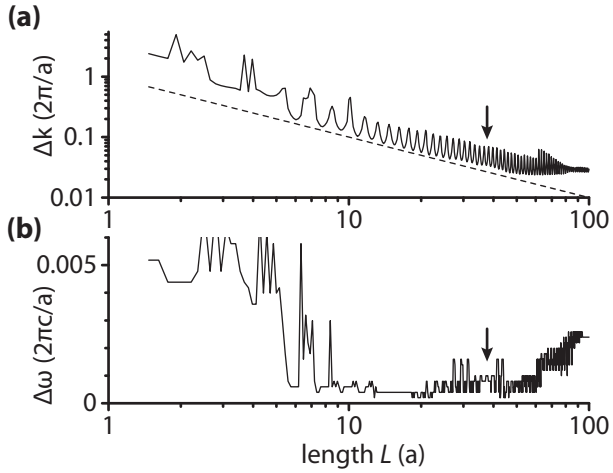

Figure 4.5: (a) Resolution for determining the 'local' wavevector, depending on the length of waveguide used in the analysis. The data is obtained at ω=0.299, in an area centered at x=132a. The dashed line depicts the theoretically attainable resolution. (b) Width of the band in the dispersion relation, depending on the length of waveguide used in the analysis. At large length, the width is large due to averaging over a large area with changing dispersive properties. The arrows in both figures depict the length used in the local dispersion relations plotted in figure 4.4

is more rapid as a function of position, i.e., the dispersion shifts significantly on a length scale of 10 or 20 lattice spacings, a suitable trade-off between frequency resolution and wavevector resolution becomes very hard. In an investigation that yields the optical phase as a function of position, like the one presented here, one may consider an evaluation of the phase evolution of the light as a function of position: the derivative of the phase with respect to position directly yields a quantity that may be considered as the local wavevector. However, such an analysis usually requires prior knowledge of all the modes excited in the structure. For example, in this study a separation of the forward and backward propagating modes would first be needed. Such a separation invariably requires a Fourier analysis, with the same trade-off as the one which was to be avoided. Hence, a determination of the local wavevector from the phase evolution in space will be limited to cases where the individual modes can be separated. Another consideration with respect to rapidly changing local dispersion relations, is whether the concept of wavevectors is still helpful or even relevant on small length scales. This consideration may be particularly relevant if transitions in propagation properties involve a non-adiabatic process.

4.6 Conclusions

In conclusion, we have fabricated and characterized a chirped photonic crystal waveguide, with an increasing hole diameter from the start of the waveguide towards the end. The gradient in hole radius is small enough to approximate the system as having adiabatically changing optical properties. Due to the increase of the hole radius, the waveguide mode in the local dispersion relation shifts to higher frequencies. We have measured the so-called local dispersion relation with a phase-sensitive near-field microscope and confirmed that the local dispersion relation depends on the hole radius in a limited region of the structure. Both in the measured dispersion relation and in the measured modal profiles of the propagating light we observed a slow-light characteristic: the dispersion relations show a clear flat band, corresponding to low group velocities ($v_g < c/260$). The degree to which the found dispersion relation is local, obviously depends on the size of the area analyzed. We showed that the trade-off between high wavevector resolution (large analysis area) and local information (small analysis area), could be made properly, since the dispersion relation shifted slowly as a function of position.

4

5 Two regimes of slow light losses

The losses in a photonic crystal waveguide were measured with a near-field microscope in the group velocity range of $c/7$ down to $c/100$. The waveguide under investigation was chirped so that the group velocity becomes position dependent and decreases adiabatically as the light propagates further into the waveguide. The position at which a given group velocity is obtained can therefore be tuned by controlling the optical frequency. By using a range of frequencies, we can investigate the losses for a specific group velocity for many different realizations of unintentional disorder and thereby obtain the realization-averaged behavior. When all group velocities are considered together the losses are found to scale proportional to $v_g^{-\alpha}$, with an unusual loss exponent of α=2.9 ± 0.3. Our measurements show that for group velocities v_g below $c/30$, the modal pattern becomes irregular, indicative of multiple scattering. Both findings show that the usual perturbative approach to describe the propagation of light in a photonic crystal waveguide with fabrication disorder breaks down at lower group velocities.

5.1 Introduction

Photonic crystals (PhCs) consist of a periodic arrangement of dielectric materials, usually with a high refractive index contrast. In a PhC with properly chosen geometry and materials, light can be strongly influenced by the periodic structure. Numerous interesting properties have been reported over the years, like photonic bandgaps,[73] negative refraction[74] and super-lensing.[26] These properties can be exploited for, amongst others, miniaturized

optical circuitry. One of the interesting properties of PhCs is that light can be made to propagate with low group velocities at specific optical frequencies.[18,19] This 'slow light' can enhance nonlinear effects,[20] useful for future on-chip all-optical switching.

5.2 Structural imperfections

In two-dimensional photonic crystal waveguides, light can in theory propagate without losses.[75] However, unavoidable structural imperfections[76] like variations in hole diameter or shapes, roughness of the interfaces of the structure and/or slight displacement of the holes will result in coupling out of the waveguide mode, thus inducing loss. We will refer to these imperfections as the disorder in the structure. The major loss channels resulting from the disorder are out-of-plane radiation losses and scattering in the backward direction in the waveguide. Since slow light propagation is intrinsically linked to a very strong interaction with the lattice in which the waveguide is embedded, the losses per unit length increase with decreasing group velocity.[39] Although the disorder created by the structural imperfections is disadvantageous for efficient guiding of light, it can give rise to interesting optical transport phenomena involving multiple scattering.[77] In the extreme case of strong scattering in disordered systems, it may lead to Anderson localization.[78]

There has been significant effort to determine how the losses in photonic crystal waveguides (PhCWs) scale with the group velocity. Hughes *et. al.*[39] suggested in a theoretical study, that the total losses scale proportional to v_g^{-2}, with v_g being the group velocity of light in the waveguide. Crucial to this study and alike,[39,79] is that the disorder is considered to be a small perturbation on the geometry of the waveguide allowing the Born approximation. The disorder therefore hardly affects the propagation of light, apart from the losses scattered out of the mode, and the optical properties can therefore be described by the properties of the unperturbed system. There have been a few studies that attempted to elucidate the scaling of the losses experimentally.[80–82] In these studies several waveguides with different lengths are fabricated. By comparing the transmission spectra of the structures for the different lengths, the losses may be determined. For such a study it is crucial that only the waveguide length differs and the mean optical properties are exactly equal. The reported results in references [80-82] range between a proportionality of the losses with $v_g^{-1/2}$ and v_g^{-2}, corresponding to loss exponents (α) of 0.5 and 2, respectively.

Here we investigate the propagation of light and the losses directly by monitoring the optical field in a PhCW en route, with a phase-sensitive near-field microscope. The waveguide under investigation is a so-called chirped waveguide: the hole radius is gradually increased along the propagation direction. As a result, the light slows down adiabatically, which leads to a position-dependent group velocity. By changing the optical frequency, the position in the waveguide for which a specific group velocity occurs can be controlled. We can therefore investigate the losses occurring at a given group velocity at different positions along the

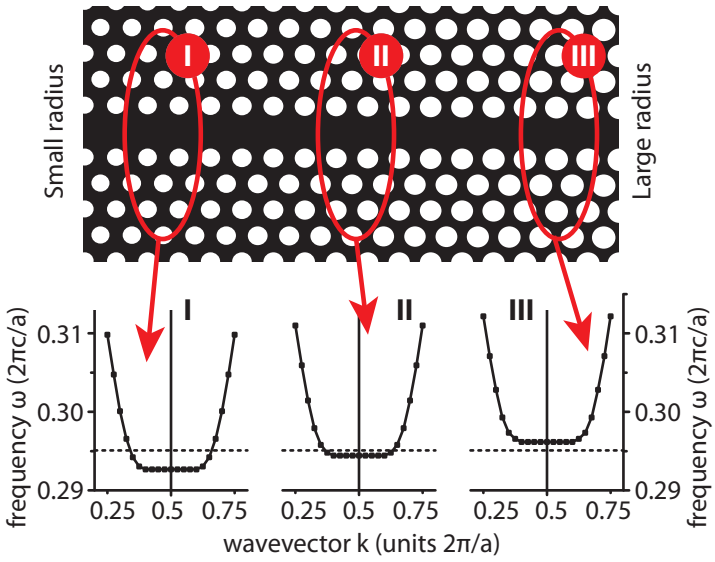

Figure 5.1: Schematic representation of the geometry of the chirped waveguide (top). The radius of the holes in the PhC lattice is linearly increased from left to right. The dispersion relation depends on the radius of the holes: the waveguide mode (continuous line) in the dispersion relation shifts up as the hole size increases. Light with a specific optical frequency (dotted line) is therefore allowed to propagate in regions I (with a relatively high v_g) and II (lower v_g), but not in region III. The dispersion relations of regions I, II and III are calculated by 3D FDTD for hole radii of 0.306·a, 0.314·a and 0.321·a, respectively.

waveguide, each with its own local realization of unintentional disorder. Thus, the chirped waveguide allows the propagation of light at low group velocity to be explored over many different realizations of the disorder by merely varying the optical frequency. We show by visualization of the modal pattern as well as a quantitative analysis of the losses averaged over many realizations of the disorder, that a perturbative approach to dealing with disorder breaks down at the lowest group velocities, in our case below $c/30$, as in this slow light regime multiple scattering becomes important.

5.3 Experimental aspects

Figure 5.1 shows a schematic of the waveguide under investigation. A PhCW is created by removing a single row of holes in the photonic crystal lattice.[17,83] From left to right the hole radius is linearly increased, resulting in a chirped PhCW.[67] We used an air-bridge structure with a 210 nm thick silicon membrane with a hexagonal lattice of air holes with a 456 nm

period (a). The hole radius increases linearly from 142 nm to 150 nm over a length of 300 lattice periods, with typical local fabrication variations in diameter of approximately 3 nm. A portion of the dispersion relation calculated by 3D FDTD calculations is presented in figure 5.1, for different sections of the PhCW. In these calculations each section is treated as if it were infinitely long, i.e., with a constant hole radius. In the dispersion relation, the waveguide mode flattens as the wavevector approaches the Brillouin zone boundary at k=0.5 (in units of $2\pi/a$). The group velocity ($v_g \equiv \mathrm{d}\omega/\mathrm{d}k$) is determined by the slope of the dispersion relation. At k=0.5 the group velocity is zero.

As the hole size increases, the waveguide mode in the dispersion relation shifts to higher frequencies. As a result, light with a certain optical frequency (dashed line in figure 5.1) is allowed to propagate in section I and II. In section III, there is no longer any supported propagating mode for the specified frequency due to the shift of the local dispersion relation caused by the larger hole radii in this section. Due to the change in hole radii, the group velocity of the light in the PhCW becomes dependent on position. For the frequency range of the guided mode shown in figure 5.1, the position dependence leads to a reduction of the group velocity along the propagation direction until the waveguide no longer allows propagation (section III). We will refer to the region were light is propagating with $v_g < c/20$ as the cut-off region. This region corresponds to group indices (defined as $n_g = c/v_g$) above 20. After this region, the light must either have been reflected back towards the input, or have been scattered out-of-plane.

The optical field inside the waveguide was measured using a phase-sensitive near-field microscope.[84] In this microscope, we scan a near-field probe over the sample at approximately 10 nm height. A small portion of the optical field in the sample couples to the probe. By scanning the probe over the surface we can map the electric (E-)field distribution in the waveguide. Figure 5.2a shows the amplitude of the E-field picked up in a near-field measurement at ω=0.2961. The waveguide is oriented horizontally, centered around y=2.8 a. The light is incident from the left. We observe that the modal pattern does not change dramatically up to x=190 a. In the cut-off region ($190a < x < 250a$), the pattern broadens laterally and becomes irregular along the propagation direction.

With the phase-sensitive near-field microscope we also recovered the phase of the propagating light. By analyzing the phase evolution over 9 lattice periods, the dominant or 'local' wavevector was determined. For the measurement at ω=0.2961, the 'local' wavevector is plotted versus position in figure 5.2b. The expected 'local' wavevector, based on the theoretical dispersion relation, is depicted in red in figure 5.3b. The measured results show very good correspondence with the results obtained from the calculated dispersion relation. By exploiting the correspondence between experiment and calculations, we determined the group velocity v_g as a function of position x from the calculated data. The result is depicted in figure 5.2c and shows that the group velocity is 0.12 c at x=0 and gradually decreases, until it reaches zero at x=248.

In order to analyze the experimental data, we summed the intensity ($|E|^2$) of the meas-

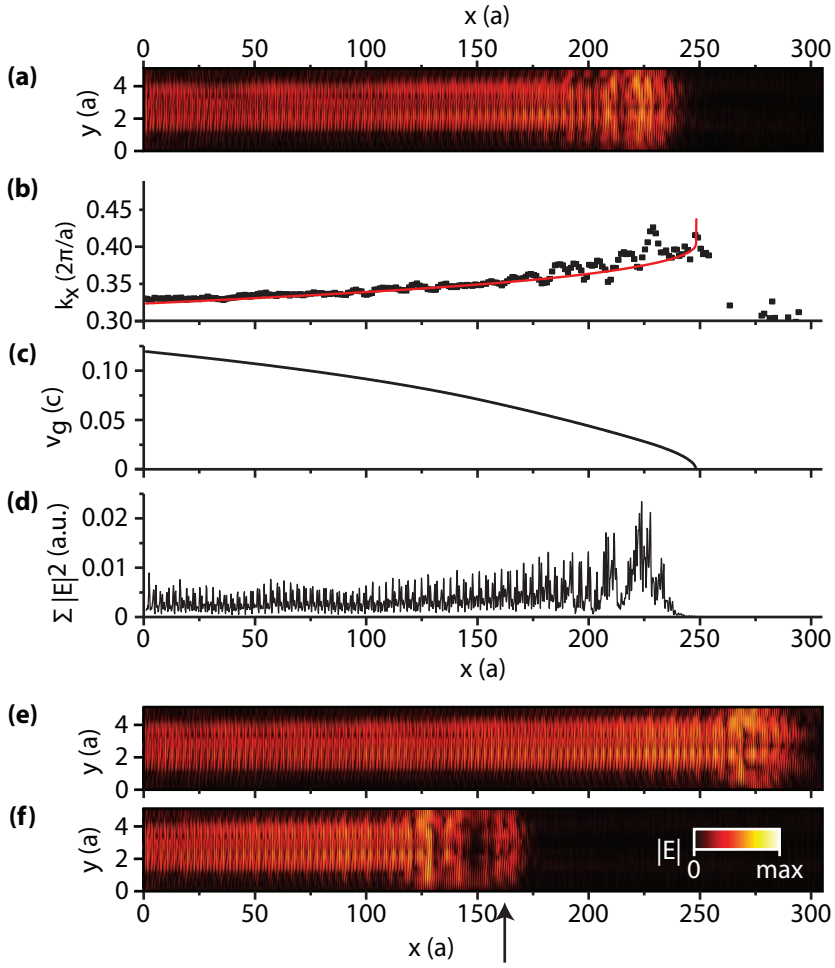

Figure 5.2: (a) Near-field measurement on the chirped waveguide at ω=0.2961 (in units $2\pi c/a$). The image represents the measured E-field amplitude. (b) 'Local wavevector' as a function of x-position, obtained from the measurement in (a) (solid points). The solid (red) line depicts the expected wavevector calculated with the dispersion relations of figure 5.1. (c) Group velocity corresponding to the calculated data in (b). (d) Summed intensity ($|E|^2$) over all y points of the image in (a), yielding the total intensity in the waveguide as a function of position x. (e,f) Measured E-field amplitude of the same waveguide and area as in (a), now at ω=0.2973 and 0.2950, respectively. The arrow in (f) indicates a striking disorder-induced resonance.

urement in figure 5.2a along the y-direction in order to suppress the effect of mode pattern differences so that the energy of the mode can be determined as a function of position along the propagation direction. The thus obtained energy as a function of position is depicted in figure 5.2d. The energy has a short-range oscillation due to two effects: the Bloch wave character of the guided mode[60] and interference of forward propagating and reflected light. The detected intensity shows dramatic changes in the cut-off region ($190a < x < 250a$): the intensity increases, becomes irregular and drops to zero when x is larger.

When we repeat the experiment at different optical frequencies, we observe qualitatively the same results: a gradual increase of the energy at larger propagation distances and an irregular pattern for positions where $v_g < c/30$. The first, expected difference is a shift in position with respect to the measurement at ω=0.2961, as can be seen in figures 5.2e and 5.2f for ω=0.2973 and ω=0.2950, respectively. Note that these are measurements on the same waveguide and the same area. The position where light stops propagating is clearly dependent on frequency, since these positions are $x \simeq 300$ for ω=0.2973 and $x \simeq 175$ for ω=0.2950. This observation is in agreement with a shifting dispersion relation as depicted in figure 5.1: at lower optical frequencies, the light stops propagating at smaller hole radii, and vice versa. For all 25 optical frequencies used in this investigation, we observe that the mode pattern becomes irregular in the cut-off region. The pattern is different for each frequency, despite the small increments in frequency ($\Delta\omega < 0.07\%$) used. The irregularities in the mode patterns are attributed to local imperfections in the waveguide geometry. Please note that the local imperfections are very small and can hardly be resolved with a good scanning electron microscope. The fact that the shape of the irregularity changes dramatically when a different local realization of the disorder is probed with the same low group velocity, e.g., compare figures 5.2a and 5.2f, is a fingerprint for multiple scattering.[85]

5.4 Transmission losses

To find the relation between waveguide losses and group velocity, we can now directly relate the position-dependent energy in the waveguide (figure 5.2d) with the position-dependent group velocity (figure 5.2c). In order to properly quantify the relation between group velocity and losses, one needs to average over the many realizations of the local disorder underlying the losses. This necessity becomes particularly clear considering the large fluctuations observed in the cut-off region. We therefore averaged our analysis over 25 measurements, with different optical frequencies. Since the shift in frequency of the local dispersion relation is linear with respect to position, the relation of group velocity and position is the same for each frequency, apart from a shift in position. By averaging over many frequencies, we average over different realizations of the disorder within a single sample, while the coupling of light into the waveguide remains unchanged.

Figure 5.3 depicts the intensity picked up by the probe as a function of the group index, av-

eraged over 25 effective realizations. It shows that the detected intensity increases linearly with group index between n_g=7 and n_g=15. At higher group indices the increase of the detected intensity slows down until the intensity reaches a maximum at n_g=50. When the group index increases further, the probed intensity decreases.

We attribute the nearly linear increase of the intensity between n_g=7 and n_g=15 in figure 5.3 to an increase of the E-field amplitude in the waveguide. The intensity ($|E|^2$) of light in photonic crystal waveguides is expected to be proportional to the group index.[20] To the best of our knowledge, our measurement is the first direct observation that the local energy density increases in a photonic crystal as the group velocity decreases. The energy in the chirped waveguide therefore increases as a result of the increase in group index, while the losses are still modest. At larger group indices the waveguide losses increase, causing the increase of the intensity with n_g to be reduced, resulting in a less than linear increase, finally resulting in a maximum followed by a decrease.

From these measurements, we can recover the losses in the waveguide as a function of group velocity. We can describe the intensity in the waveguide according to Lambert-Beer's law:

$$I(x + \mathrm{d}x) = I(x)\mathrm{e}^{-An_g^{\alpha}(x)\mathrm{d}x}, \tag{5.1}$$

describing that an infinitesimal increase in position is accompanied by a loss which scales with n_g^{α}, with n_g a function of x. We keep the loss exponent α constant for all n_g, in order to compare our quantitative results with that of others. Using the assumption that $|n_g^{\alpha}(x)\mathrm{d}x| \ll 1$, the above equation leads to

$$I(x) = I(0)\exp[-A\int_0^x n_g^{\alpha}(x')\,\mathrm{d}x'], \tag{5.2}$$

with A being a loss coefficient, $I(0)$ the intensity input in the waveguide. When we want to fit this relation to the measured results, the integral needs to be evaluated, but since $n_g(x)$ can not be approximated with by low-order polynomial, we have evaluated the integral in equation 5.2 numerically.

In the fit of equation 5.2 to the measured position-dependent intensity, the fit parameters were the loss exponent α, the loss coefficient A and $I(0)$. The resulting fit is shown in figure 5.3. We find a close agreement with the measured results using α=2.84. The fit has a goodness R^2 of 0.97 [‡]. Note that an R^2 value of 1 represents a perfect overlap with the data. Following the fit result, the loss at n_g=7 would be 1.8 dB/mm, which is a typical loss figure for these waveguides.[80,81] Please note that the record low loss in these waveguides is on the order of a few dB/cm. By allowing R^2 values down to 0.95, we obtain a loss exponent α of 2.9 ± 0.3. For reference, following reference [39], we have also plotted the best fit

[‡]
$$R^2 = 1 - \frac{\sum_N (\log I_{c,N} - \log I_{m,N})^2}{\sum_N (\langle \log I_{c,N} \rangle_N - \log I_{m,N})^2}, \tag{5.3}$$

with $I_{c,N}$ and $I_{m,N}$, being the calculated and measured data, respectively. $\langle\ \rangle_N$ denotes the average.

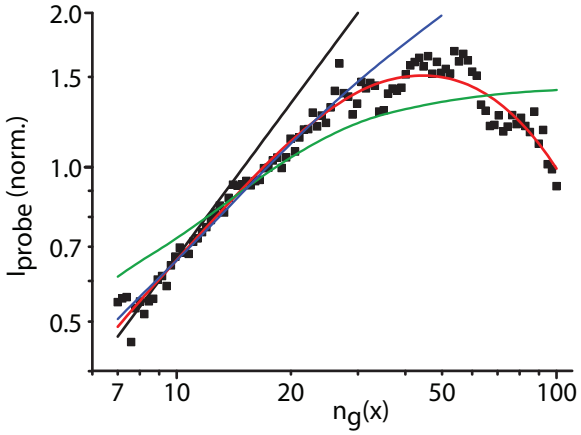

Figure 5.3: Intensity detected by the near field probe as a function of the group index n_g, normalized at n_g=20. The data is averaged over 25 measurements, ranging between ω=0.2936 and ω=0.2982. The black line shows a linear relation. The red line represents the best fit to the measurements with $\alpha = 2.84$. The green line represents the best fit using $\alpha = 2$ when the fit is forced to describe the measurements for all n_g. The blue line is the result of a fit with $\alpha = 2$ for the data points with $n_g < 30$ only.

result using $\alpha = 2$ in figure 5.3 for the situation that the exponent α is kept constant for all n_g, i.e., for all group velocities. Clearly, if a single exponent $\alpha = 2$ is forced to describe also the group velocity regime where multiple scattering phenomena become important, the result is unsatisfactory. The result has an R^2 of 0.82.

5.5 Discussion and conclusions

The found exponent of 2.9 ± 0.3 is still significantly larger than the exponent predicted and measured previously.[39,81,82] The large exponent cannot be attributed to a non-adiabatic transition to lower group velocity due to the design of the chirped waveguide. In fact, recent publications[86,87] have shown that a transition to velocities of $v_g < c/100$ can be very efficient in chirped waveguides, even within 3 or 4 lattice spacings, compared to the ~ 200 lattice spacings used in this investigation.

For the analysis performed in this chapter, it is crucial that the I_{probe} we measured and plotted in figure 5.3 is linearly proportional to the field amplitude squared in the waveguide. In other words, the coupling efficiency from structure to near-field probe must be constant. This is not a trivial assumption however. Disorder in the structure can cause scattering of light out of the forward waveguide mode, which we call loss. Potential channels to which the light can scatter are backscattering into the waveguide mode, out-of-plane scattering

and coupling to the near-field probe. The ratio for scattering of the light into each of these channels, depends on the density of states (DOS) of the individual channels, which is closely related to the group velocity. For slow light in the waveguide, the DOS-dependence results in a higher probability to scatter back into the slow waveguide mode, at the expense of scattering into an out-of-plane channel. With this dependence in mind, we expect a lower pickup efficiency for the near-field probe if the group velocity in the waveguide is low. Naively, one could argue that the drop in I_{probe} in figure 5.3 is due to the DOS-dependence. However, when we fit a loss model which includes the DOS-dependence to the measured data, we find a range of acceptable loss exponents α between 2.7 and 4.6. These values are still significantly higher than the expected exponent of $\alpha = 2$, from theoretical predictions, thus corroborating our finding.

The large discrepancy between theoretical predictions and the experimental observations can be explained as follows. The theoretical predictions are based on perturbation theory. While the essential assumption that the modes in the slightly disordered waveguide can still be described by the modes in the perfect waveguide may still hold, the theory does not include multiple scattering phenomena of backward and forward propagating modes between local scattering centers. The multiple scattering leads to a change in the propagation properties, for example by the formation of highly localized resonances (see arrow in figure 5.2f). As the group velocity decreases, the back-scattering into the same (but backward) waveguide mode increases.[39] Hence, the multiple scattering becomes more prominent for smaller group velocities.

We observe two regimes of slow light propagation. In the first regime the waveguide modes are well behaved and can be described with existing theory. In the second regime multiple scattering becomes important, which is no longer described by existing theory. The group velocity for which the transition between the two regimes occurs will depend on the quality of the fabrication: the higher the quality, the smaller the group velocity for which multiple scattering becomes important. In our case the transition occurs at roughly $c/30$.

In conclusion, our measurements on a chirped photonic crystal waveguide show that the detected intensity increases in a near-field microscope as the group velocity in the waveguide decreases. The increase is proportional to the increase of the electromagnetic energy density in the waveguide. As the light propagates further, the group velocity decreases further and a decrease in detected intensity due to increased waveguide losses is observed. In the area were the losses increase, the modal pattern breaks up and becomes irregular. Using the experimental data, we recovered that the losses scale proportional to $v_g^{-\alpha}$, with α=2.9$\pm$0.3, when a single exponent is used to describe all the losses together: significantly larger than expected based on a perturbative treatment of the disorder. From our observations we conclude that two regimes should be considered when describing the propagation in a photonic crystal waveguide: one in which the group velocities are relatively high and which is well described by the usual perturbative methods, and the other, at smaller group velocities, when multiple scattering becomes important and influences the propagation properties.

5

6 The effect of higher-order dispersion

We have studied the dispersion of ultrafast pulses in a photonic crystal waveguide as a function of optical frequency, in both experiment and theory. With phase-sensitive and time-resolved near-field microscopy, the light was probed inside the waveguide in a non-invasive manner. The effect of dispersion on the shape of the pulses was determined. As the optical frequency decreased, the group velocity decreased. Simultaneously, the measured pulses were broadened during propagation, due to an increase in group velocity dispersion. On top of that, the pulses exhibited a strong asymmetric distortion as the propagation distance increased. The asymmetry increased as the group velocity decreased. The asymmetry of the pulses is caused by a strong increase of higher-order dispersion. In addition, we demonstrate by a near-field experiment, that the second and third-order dispersion can be reduces by factors 9 and 7 respectively, by merely changing the width of the waveguide.

6.1 Introduction

An interesting feature in both bulk photonic crystals and photonic crystal waveguides (PhCWs) is, that light will propagate with a very low group velocity at some specific optical frequency.[17,19,88,89] Hence, light-matter interaction is very strong and can be exploited for enhanced non-linear interactions in PhCWs.[20] Recently, all-optical switching in PhCs has been demonstrated[90] and PhCW lasing has been reported.[91] Also optical solitons have been proposed[92] and the nonlinear propagation of ultrafast pulses has been reported.[93]

The group velocity is usually strongly dependent on frequency. This effect is quantified

by the group velocity dispersion (GVD). Since every optical pulse has a certain spectral content, an optical pulse will experience a broadening due to the GVD. In PhCWs, this effect occurs at much shorter propagation lengths compared to conventional waveguides. Since the dispersive properties can be tailored by choosing the proper geometry, a tailored GVD can be exploited for pulse compression.[94] This so-called dispersion control of pulses in PhCWs is one of the promising applications of photonic crystals.

Recently, a number of studies have investigated the dispersive effect of PhC structures on pulse propagation.[18,95,96] Generally, these studies report on the reduction of the group velocity. Asano and co-workers also quantified the enhanced group velocity dispersion in a PhCW.[96] Enhanced GVD was also found in bulk 3D photonic crystals.[95] In this work, evidence was found of third order dispersion (TOD),[97] but not quantified. Aspects of third and higher-order dispersion have been discussed in theory in the context of slow light propagation in nonlinear photonic crystals.[98]

For a detailed analysis of the dispersion of an optical pulse in a waveguide, one would ideally want to monitor the pulse shape as it propagates through a structure. Only then can the evolution of the pulse shape be evaluated as it propagates, and pulse distortion due coupling in and out of the sample therefore be excluded. Since out-of-plane radiation is absent for truly guided light, i.e. under the light line in a perfect structure, the study of the dispersion effects of a single, long structure as a function of position, would rely on scattering at defects, which is not desirable. Alternatively, structures of different length can be used, which has the disadvantage that the dispersion effects are studied in different waveguides. We circumvent these disadvantages by using a near-field approach. Near-field microscopy allows the local investigation of propagating light with a sub-wavelength resolution, while the structure under investigation is not disturbed.[55]

Here we present the near-field probing of optical pulses as they travel through a photonic crystal waveguide. As we change the optical frequency and in this way access slower propagating light, the dispersion of the pulses increases dramatically. The pulse shapes change from initially symmetric to broader and more asymmetric pulse envelopes as the group velocity decreases. The measurements are reproduced by calculating the expected pulse shapes from the dispersion relation. Thus we demonstrate that higher-order dispersive effects play an important role in the propagation of light in photonic crystal waveguides. These higher-order dispersive effects can be detrimental to many slow light applications and should be taken care of by proper dispersion engineering. We demonstrate one method to achieve this dispersion engineering. By changing the width of the waveguide, a mode with low group velocity and low dispersion is obtained. Our near-field experiments show that pulses indeed exhibit much less pulse dispersion in these broader waveguides.

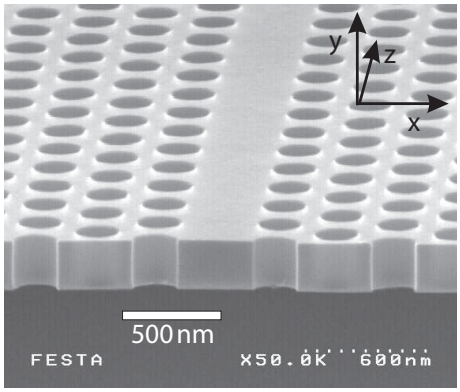

Figure 6.1: Scanning electron microscopy image of the photonic crystal structure. The inset denotes the used cartesian coordinate system used in this chapter. The PhCW is oriented in the z-direction. The x-direction is in the plane of the PhC perpendicular to z. The y-direction is perpendicular to the plane of the membrane.

6.2 Experimental aspects

The samples used in these experiments were fabricated in epitaxial hetero-structures grown by molecular beam epitaxy. A 250-nm-thick GaAs core layer was grown on top of a 2-μm-thick $Al_{0.6}Ga_{0.4}As$ sacrificial layer on a GaAs substrate. A membrane-type photonic crystal structure was fabricated using high-resolution electron-beam lithography, dry etching, and selective wet-etching techniques. The 2D PhC thus consisted of a hexagonal array of air holes etched into a planar GaAs slab. The sacrificial layer was removed by an HF solution via the air holes. The lattice constant is 339 nm with air-holes of 204 nm in diameter. By leaving a single row of air-holes unperforated, a so-called W1 waveguide was created. A section of the resulting structure is shown in figure 6.1.

The propagation of light in the W1 waveguide is described by the dispersion relation, shown in figure 6.2a. This dispersion relation of the W1 waveguide was calculated by 3D plane wave expansion.[99] In the dispersion relation, we found two waveguide modes within the photonic crystal bandgap for TE polarization. These modes are denoted odd and even in figure 6.2. The even mode is largely underneath the light line and is therefore in principle lossless.[100] Near $\omega = 0.254$ the even mode bends towards $k = \pi/a$, corresponding to a strong reduction of the group velocity (v_g), since the v_g is determined by the inverse of the slope of $k(\omega)$. Note that the 2D bandgap only exists for TE polarization. TM polarized light can either propagate through the crystal, or it can be confined to the waveguide by refractive index contrast.[101]

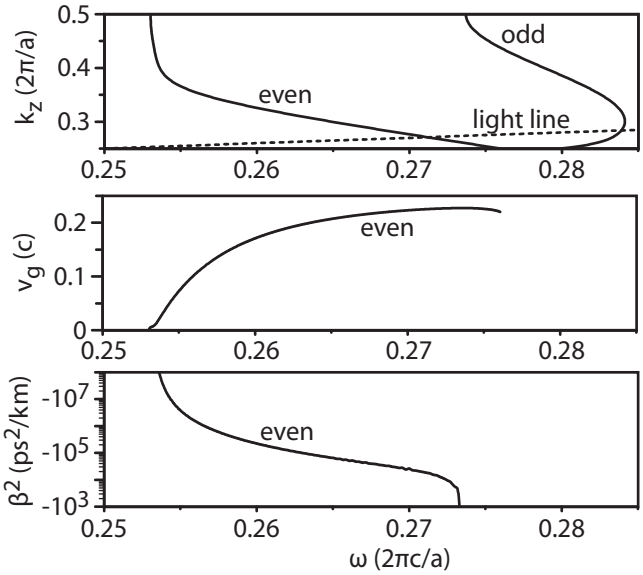

Figure 6.2: (a) Portion of the dispersion relation of the W1 waveguide calculated by 3D plane wave expansion. In the 2D bandgap, two waveguide modes are allowed to propagate for TE polarization, denoted "even" and "odd" by their in-plane symmetry with respect to the waveguide. The light line ($\omega = ck$) is represented by the dashed line. (b) The group velocity (v_g) as a function of frequency, calculated by taking the derivative of $k(\omega)$. (c) The second order derivative of $k(\omega)$ gives the group velocity dispersion ($\beta_2 = d^2k/d\omega^2$). As the group velocity reduces around $\omega = 0.254$, the GVD increases several orders of magnitude.

This dispersion relation $k(\omega)$ of a medium can be expressed in the Taylor expansion:

$$k(\omega) = \beta_0 + \beta_1(\omega - \omega_0) + \frac{\beta_2}{2}(\omega - \omega_0)^2 + \frac{\beta_3}{6}(\omega - \omega_0)^3 + \dots . \tag{6.1}$$

In this expansion, the coefficients β_i represent the dispersive constants of a material. The wavevector equals β_0, β_1 is the inverse of the group velocity (v_g), β_2 and β_3 represent the group velocity dispersion (GVD) and the third order dispersion (TOD), respectively.

In figure 6.2b, the group velocity of the even TE-polarized mode is shown as a function of optical frequency. At high frequencies, v_g is found to be $0.23c$. As the frequency is reduced, the group velocity decreases to become zero at $\omega = 0.253$. The frequency dependency of β_2 is shown in figure 6.2c. At high frequencies, the GVD is in the order of -10^4 ps^2/km. As the frequency is reduced and the group velocity drops, the GVD increases by several orders of magnitude. The GVD is many orders of magnitude larger than in fiber optics. For comparison, the GVD in an optical fiber is between -28 and +8 ps^2/km.[102] Because, the GVD is also frequency-dependent, higher-order dispersive effects can also play a role in the propagation of light through PhCWs.

We monitored the broadening of femtosecond pulses as a function of propagation distance. We used laser light obtained from a Ti:Sapphire-pumped optical parametric oscillator, that provided pulses with a tunable carrier wavelength between 1200 and 1350 nm. The full width at half maximum (FWHM) of the pulse spectrum was 12 nm, corresponding to a Fourier limited pulse duration of 207 fs (FWHM). These pulses were coupled into the PhCW by focusing the light onto the membrane facet with a microscope objective with a numerical aperture of 0.4.

We investigated the waveguide with the heterodyne interferometric detection scheme, which yielded spatially-resolved, phase-sensitive and time-resolved information on the propagation light.[55] Figure 6.3 shows the setup in a schematic representation. Before coupling the pulsed light into the PhCW, the light was split into two parts. The light traveling through the sample and the fiber probe is called the signal branch. The other branch (reference), contained an optical delay line. Both the signal and reference light was mixed interferometrically and collected onto a detector. The detector signal is fed into a lock-in amplifier (LIA). Using pulsed laser light, the interference will only be present when the pulses in both branched overlap in space and time at the mixing junction. In order to obtain temporal overlap, the optical path of the reference branch could be varied. Thus, our setup allowed two distinct measurement techniques: either scanning the fiber probe for a fixed delay line position (i.e. a fixed reference time) or scanning the delay line for a single probe position.

Chapter 2 describes how the interferometric near-field microscope measures pulses that may have dispersed. The main result is found in equation 2.19 which shows, in a slightly different form, that the signal obtained from the lock-in amplifier is

$$V_{LIA}(z,\tau) \propto 2\mathcal{F}^{-1}\{E_{ref}(\omega)E_{sig}(\omega)e^{ik(\omega)z}\}. \tag{6.2}$$

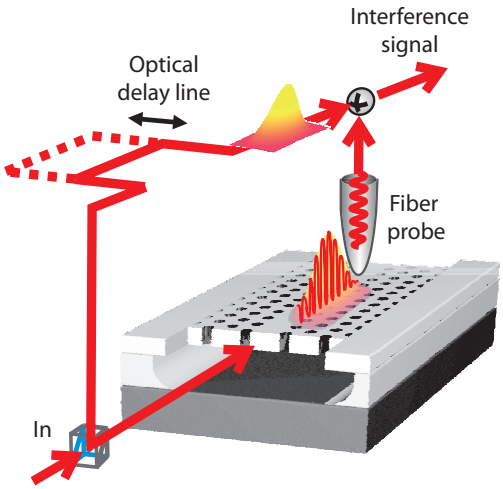

Figure 6.3: Schematic representation of the experimental setup. Pulsed laser light was coupled into the PhCW. The fiber probe collected a fraction of the propagating light. This light was mixed interferometrically with a reference pulse from the same laser. Only the interference between the two pulses was detected. Two measurement modes were possible: either scanning the fiber probe over the surface with a fixed optical delay line, or scanning the delay line for a single probe position.

This equation contains the E-field spectrum of the reference (E_{ref}) and signal branch (E_{sig}). The inverse Fourier transform is denoted $\mathcal{F}^{-1}$. We assume that the spectrum of the light in the signal branch was not necessarily equal to the spectrum of the light in the reference branch, due to a frequency-dependent group velocity in the waveguide. Therefore, not all frequencies would couple to the PhCW equally efficiently and we assume that the coupling of the light to the waveguide obeyed Fresnel's law.[103]

Note that the LIA signal may be complex, illustrating that we measure the propagating light phase-sensitively. The absolute value of V_{LIA} is the interference amplitude, while the argument of the signal resembles the phase of the light in the signal branch. In equation 6.2, V_{LIA} has two variables z and τ. In the experiments, either z or τ in equation 6.2 was fixed, while the other variable was varied. In this way, two measurement approaches were possible: a time-resolved measurement of the interference or a space-resolved measurement, experimentally corresponding to scanning either probe or delay time.

In the first measurement scheme, the fiber probe is scanned over the sample. Such a measurement results in the distribution of the interference as a function of position. We will refer to this measurement mode as the spatial interference distribution (SID) measurement and it contains a combination of dispersion and pulse shape information. With this technique, spatial properties can be derived on the propagation of light, for example wavevectors and mode profiles.[104]

In the second scheme, the probe is kept at a fixed position on the waveguide and the optical path length of the reference branch is varied. Now, a pulse cross-correlate (PXC) between the light in the two branches is obtained in time. With a PXC measurement, temporal information can be recovered, like optical frequency and pulse dispersion.[95] Obviously, overlapping conclusions can be drawn from either measurement (SID and PXC), like pulse dispersion. Nevertheless, the two methods complement each other. Only, by using both measurement approaches, the full picture can be obtained.

6.3 Near-field results

Figure 6.3 shows the result of a SID measurement of the pulses in the W1 PhCW. At each scan position, the interference between the reference and signal (including sample) pulses is measured. Measurements are presented at the optical frequencies 0.2664, 0.2635 and 0.2603 in normalized units. The optical delay in the reference branch was chosen such that the maximum of the measured optical signal was found at approximately the same position. Because the group delay increased in these measurements with decreasing frequency, the delay τ was increased going from figure 6.3a to figure 6.3c. The pulses are found to be well confined to the waveguide in the lateral direction. At each frequency, the spatial distribution along the propagation direction is different. At the highest frequency (ω=0.2664), the pulse in the structure was least distorted by the dispersion and we find a smooth and

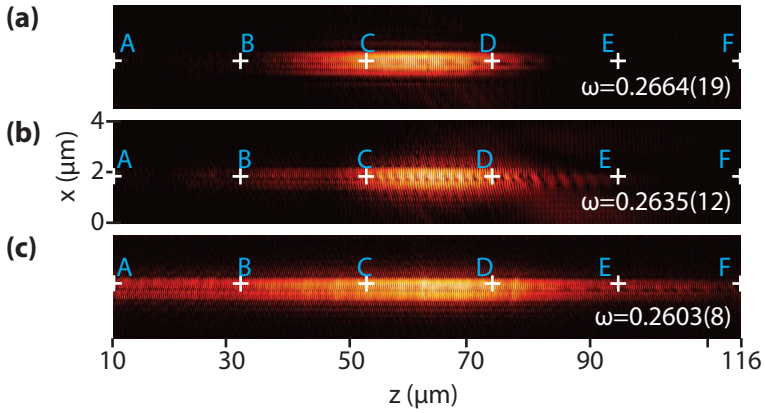

Figure 6.4: Near-field optical measurement obtained by scanning the surface of the PhC sample. The false-color images represent the amplitude of optical interference. Measurements at normalized optical frequencies 0.2664, 0.2635 and 0.2603 are shown in (a), (b) and (c) respectively. Images size: 106μm x 4μm. The crosses "A" up to "F" represent the positions were additional experiments were conducted.

short envelope of $25(2)$ μm (FWHM) in width. As the frequency was reduced, the measured pattern was elongated along the propagation direction. At ω=0.2635 the elongation was still moderate, but the measurement at ω=0.2603 shows significantly broader pulses ($48(3)$ μm FWHM) than at higher optical frequencies. A clear beating pattern is visible in the measurement at ω=0.2635. Most probably, an unwanted TM polarized mode was generated while coupling light to the structure, which "quasi-interferes" with the TE mode, resulting in the modulated amplitude pattern. Note that due to the mixing of polarizations in the near-field probe, quasi-interference can occur between orthogonally polarized modes.[101,105] We see that the pulses are broadened, as we approached the slow-light region of the dispersion relation. From the SID measurements, the temporal shape of the pulse can not be recovered. Therefore we conducted additional experiments, to determine the pulse dispersion in a more direct fashion.

We measured the cross-correlation function of the pulses in the reference and signal branch in a PXC measurement. These interferograms are measured at six positions along the waveguide. The positions are equally spaced along the propagation direction and the first and last positions ("A" and "F") are at 10 μm and 116 μm distance from the waveguide input facet, respectively. The position of the fiber probe at each of these locations is highlighted with crosses in figure 6.3. The interferograms resulting from the PXC measurements are shown in figure 6.5a-c. For clarity only the amplitude of the interferograms is presented, while all the underlaying fringes are also measured. The underlaying fringes of the measurement at position "F" in figure 6.5a are shown in figures 6.6b and 6.6c. The interference

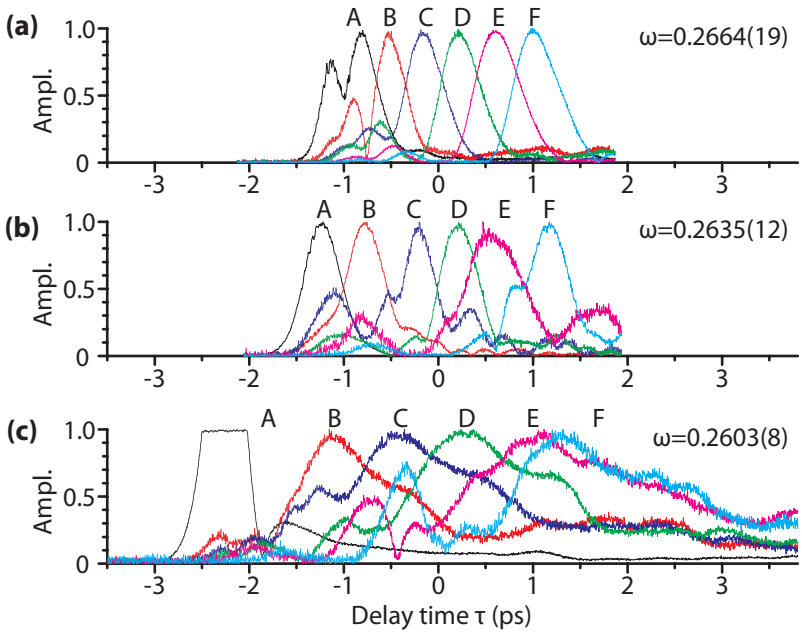

Figure 6.5: (a-c) Cross-correlation functions of the pulses in reference and signal branch of the interferometric setup. At the optical frequencies 0.2664, 0.2635 and 0.2603, the interferograms are measured at 6 equidistantly spaced points on the waveguide between 10 μm and 116 μm from the membrane facet. These measurement points are highlighted with crosses in figure 6.3. The measurement points "A"-"F" correspond to the points in figure 6.3, i.e. the interferogram "A" is measured at location "A". The interference amplitudes are normalized with respect to their maximum. In the first curve in (c), our detector saturates because this close to the incoupling point, light from the coupling objective is picked up directly.

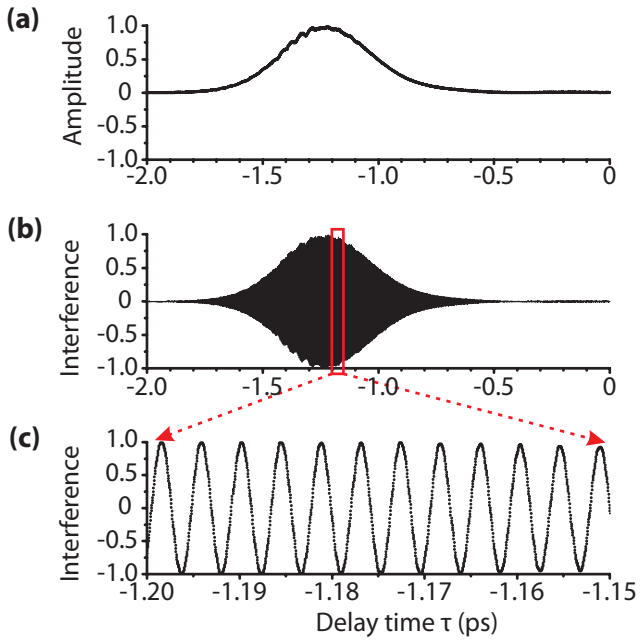

Figure 6.6: Details of the measurements in figure 6.5 at position "A" at $\omega = 0.2635$, showing the interference amplitude (a) and the underlaying interference fringes (b and c).

fringes are well resolved. By Fourier transformation, the optical carrier frequency is recovered. We find frequencies of ω =0.2664(19), 0.2635(12) and 0.2603(8). The error in these values is given by the FWHM of the corresponding Fourier transforms.

Six interferograms at ω =0.2664 are shown in figure 6.5a. The interferograms are found at different delay times, corresponding to the traveling time of the pulse. We analyzed both the center of mass and the maxima of the interferograms as a function of probe position. We found a linear dependence of the found delay time τ as a function of probe position z. The slope represents the group velocity. Due to the asymmetric pulse dispersion (especially at low ω), the found velocity is slightly different, depending on with method was used. We found that, the center-of-mass approach results in a too low v_g, whereas analyzing the maxima results in a too high group velocity. Therefore, we used both approaches to determine the group velocity, were the results represent the upper and lower error margin. In this way, we find a group velocity of $c \cdot 0.188(5)$ for $\omega = 0.2664$. Similarly, the group velocities of the other measurements are also calculated. The group velocities for the measurements at ω=0.2635 and 0.2603 are $c \cdot 0.151(5)$ and $c \cdot 0.116(9)$, respectively.

In addition to a difference in group velocity, we observe a broadening of the interferograms. At ω =0.2664, the interferogram retains its initial shape, but as the pulses travel further in

the PhCW, the interferogram is broadened up to 0.57(5) ps at position "F". This broadening is still moderate at this high frequency, but as the frequency is reduced to ω=0.2603 the pulses experience a much stronger broadening. At the same spatial position ("F"), we measured a FWHM of the interferogram of 2.2(2) ps. Interestingly, as the pulse has propagated through 106 μm, the shape of the pulse has become asymmetric for all frequencies. The largest asymmetry is found in the measurements at ω=0.2603.

Also other modes can be recognized in figure 6.5. Both air-guided light and a TM-polarized mode is detected at ω=0.2664. These modes are visible as smaller side-lobes on the main pulse. We could discriminate these modes by their group velocities found in figure 6.5 and their spatial profile in the measurements of figure 6.3. Particularly at the measurement position at 10 μm from the facet, the air-guided light is very strong. This observation is not surprising, since we couple light into the structure via an objective, that focusses light onto the facet. Since a diffraction limited spot at these wavelength is larger in diameter (3 μm) than the membrane thickness, such coupling results in some light skimming over the surface of the PhCW.

At ω=0.2635, a TM-polarized mode is very strong and causes a quasi-interference with the dominant TE-polarized mode. Specifically, a TM-polarized crystal mode travels at roughly the same group velocity as the TE defect mode, which causes the irregular pulse shapes in the interferograms in the measurement at ω=0.2635. The TM-crystal mode is particularly strong in the measurements at this frequency. In the other measurements, its influence is negligible. From a Fourier transform of the complex fields in figure 6.3, we know that multiple k-vectors are present in the measurement.[101] These correspond to the even TE-mode, a TM waveguide mode and a TM crystal mode, each having a different group velocity. The spatial overlap of the orthogonally polarized pulses is confirmed by selective Fourier filtering of the individual wavevectors corresponding to a single mode.[104]

In figure 6.7, we have summarized our experimental findings, and compared these to the values derived from the calculated dispersion relation. In this figure, two additional experiments were added. The wavevectors are determined by means of a Fourier transform of the SID measurements.[18,101] With ω and k known, a portion of the dispersion relation can be drawn. In figure 6.7a, the measured dispersion relation is slightly offset (0.5% of ω) with respect to the theoretical dispersion relation. This offset can be attributed to a slight offset of the theoretical dispersion relation of $\Delta\omega \approx 0.006$, compared to the found results in the measurements. This small difference can easily be explained by assuming that the actual geometric and optical properties of the sample are slightly different from the parameters used in the simulations.

The group velocities are shown in figure 6.7b as a function of frequency. We find group velocities ranging from $0.188(5)\cdot c$ down to $0.108(9)\cdot c$. The qualitative agreement between experimental data and the theoretic dispersion relation is clear. Again, the measured points are offset in frequency with respect to the theoretic curve. The discrepancy in figure 6.7b (2% of ω) is larger than in figure 6.7a. The larger offset suggests that the actual dispersion

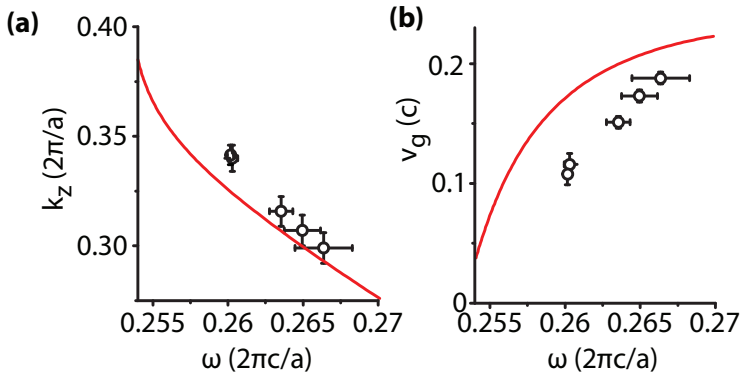

Figure 6.7: Summary of the found experimental results. The carrier frequency of the pulses is found by Fourier transformation of the interferograms. In both figures, the theoretical values are depicted by a straight red line. (a) The theoretical dispersion curve and the experimentally found dispersion relation of the TE mode. The values of k are found by Fourier transformation of the data from the SID measurements in figure 6.3. (b) Group velocity of the pulses, found by evaluating the center-of-mass of the interferograms in figure 6.5.

relation differs from the simulated curve in two aspects. First, the actual curve is offset in frequency as is observed in figure 6.7a. Second, the actual curve runs steeper than the simulated curve, due to the difference in group velocity.

6.4 The effect of higher-order dispersion

In order to demonstrate the effect of higher-order dispersion on pulse propagation, we will compare our theoretical findings with the results obtained from simulations. We have solved equation 6.2 numerically using the full dispersion relation in figure 6.2a. The numerical result describes the interferogram at a specific point on the waveguide. In this way, we can compare the results in figure 6.5a-c directly with what is expected from the dispersion relation. Since the found experimental dispersion relation, is not an exact match to the calculated dispersion relation, we matched the group velocities of experiment and simulation. We found that the calculated results at frequencies ω=0.2620, 0.2585 and 0.2565 correspond to the experimental frequencies ω=0.2664, 0.2535 and 0.2503. We have calculated six interferograms at positions from 10 μm up to 116 μm and the results are shown in figure 6.7. Again, only the amplitude of the interferograms are shown for clarity.

In figure 6.8, the interferogram envelope hardly changes at frequency ω=0.2620. At this frequency, only a slight symmetric broadening is visible after 116 μm of propagation. This slight broadening is quite in contrast to the results at ω=0.2585. At this frequency, the in-

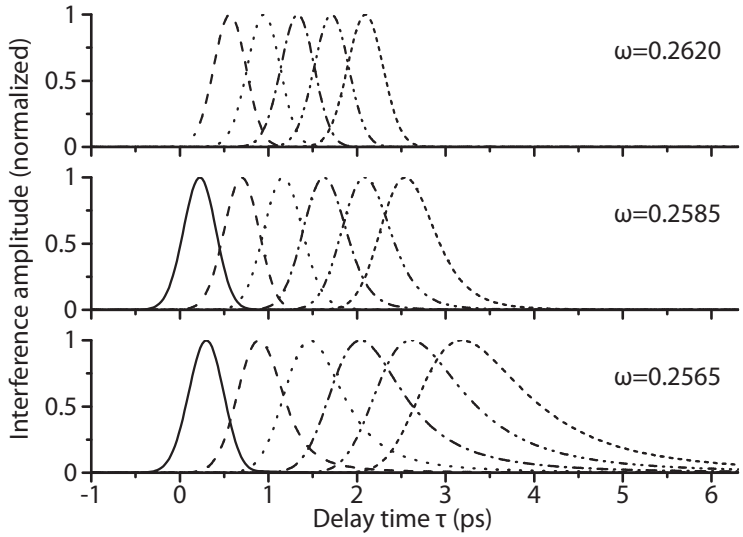

Figure 6.8: Calculated amplitude of the interferograms at frequencies 0.2620, 0.2585 and 0.2565, using the dispersion relation from the simulations (figure 6.2a). For each frequency, the interferogram is calculated for 6 waveguide lengths, equidistantly spaced between 10 and 116 μm.

terferograms are clearly broadened when propagating through the waveguide. This effect is present much stronger when calculating the envelopes at ω=0.2565. Now, the dispersion is very strong and after 116 μm, the pulse are approximately 3 times longer (FWHM) than initially. At this frequency, the asymmetry of the interferogram becomes clear. Since the spectrum of the pulses is symmetric along the carrier wavelength, the asymmetry in temporal pulse shape (and also in the interferogram) can only be caused by the enhanced higher-order dispersion in the waveguide. By comparing figures 6.5 and 6.8, we can conclude that the overall interference envelope change is similar in the measurements and the calculation.

From the theoretical interferograms corresponding to the measurements at $\omega = 0.2603$, we calculated the magnitude of the dispersive terms. We found the following GVD: $\beta_2 = -1.1(3) \cdot 10^6$ ps^2/km. For TOD we find $\beta_3 = 1.1(4) \cdot 10^5$ ps^3/km and for the fourth order dispersion we found $\beta_4 = -8(4) \cdot 10^3$ ps^4/km.

Next we will demonstrate the influence of the higher-order dispersive terms, if the dispersion is approximated by the Taylor-expansion in equation 6.1. We recalculated the interferogram of figure 6.5c (position "F"), since this interferogram shows the strongest effect of higher-order dispersion. First, the dispersion free propagation of light was considered, in other words $\beta_{>2} = 0$ in equation 6.1 and using this dispersion, the interferogram was

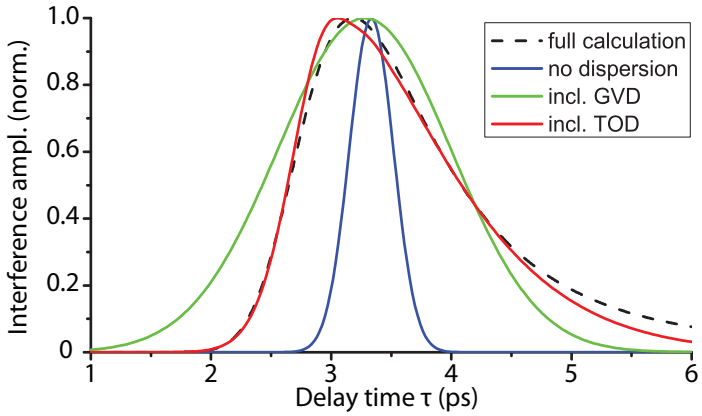

Figure 6.9: The effect of higher-order dispersion on the propagation of a slow pulse. The pulse shape is calculated after 116 μm of propagation at $\omega = 0.2565$. The blue curve represents the interferogram of dispersion-free propagating pulses. In the green curve, the effect of GVD is included. The third order dispersion is included in the red curve. In the dashed black curve, the full dispersion relation is included.

recalculated. In steps, the higher-order dispersive terms were added to the calculation. First only GVD and then TOD was added to the calculation. The results are shown in figure 6.9, where they are compared to the calculation using the full dispersion relation, with all dispersive orders included. Clearly, if we compare the dispersion-free propagating pulse with the full calculation, it is clear that the pulse broadens significantly and the goodness R^2 of the overlap between the two curves is 0.44, while an R^2-value of 1 represent a perfect overlap. This broadening is also visible if the GVD is included in the calculation. Now the R^2 increased to 0.90. However, the shape of the interferogram is still symmetric. We obtain an asymmetric interferogram if TOD is considered, which approximates the actual interferogram quite well with an R^2 of 0.99. If also the fourth order dispersion is included (not shown), a slightly better overlap is found. Note however, that the group velocity in this calculation is still quite high ($v_g = 0.116 \cdot c$). If the group velocity is further decreased, higher-order dispersive effect play an increasingly important role and then, using a Taylor expansion as in equation 6.1 is an inaccurate approximation to the dispersion relation if only lower order dispersive terms are considered.

6.5 Slow light with low dispersion

The photonic crystal waveguide that was studied in the previous section is a promising candidate for highly integrated photonic circuitry. Since some frequencies of light are not allowed to propagate in the crystal region of photonic crystals, waveguide bends can be

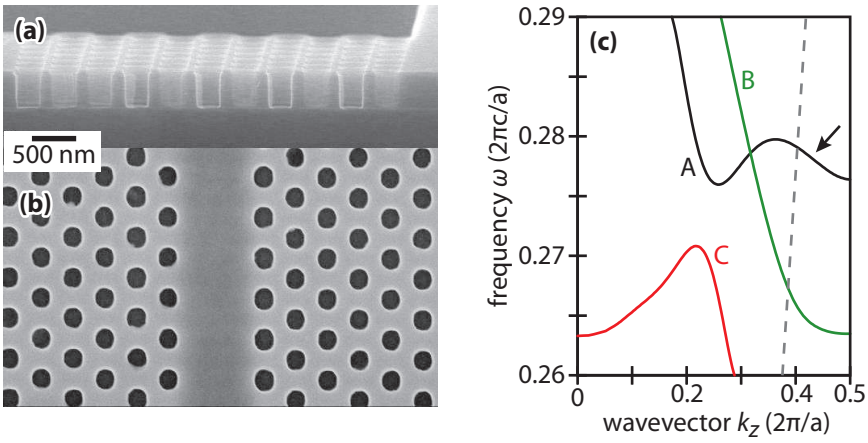

Figure 6.10: (a,b) Scanning electron micrographs of a photonic crystal waveguide, with a waveguide width of two rows of holes (W2). The crystal area is a hexagonal lattice (period $a = 420$ nm) of air holes (radius 118 nm) in a 240 nm thick Si layer on top of SiO_2. The images show a side view (a) and a top-view (b). (c) Portion of the dispersion relation for light polarized in the plane of the top layer in the frequency range of 0.26-0.29 in normalized frequency units. Three waveguide modes are shown, all are confined to the waveguide, but have different symmetries. Mode A (black) and C (red) have even in-plane symmetry whereas B (green) has odd symmetry. The light line of the SiO_2 is shown as the gray dashed line, indicating the wavevector of light in bulk SiO_2. The arrow indicates a slow mode with low dispersion.

very sharp,[106] passive filters can be very small[42] and cavities can be fabricated with a low modal volume.[27] For some applications, the dispersive effects discussed in the previous sections are detrimental to the functioning of an actual photonic crystal device. To that end, optical signals, which are a collection of pulses must retain their shape and thus not broaden due to dispersion.

To this end, the material must have low dispersion so that the values of β_2, β_3 and higher terms are negligible. In addition, a low group velocity would be advantageous for enhanced light-matter interaction. In a device where nonlinear optical effects are exploited, a slow wave can increase the efficiency significantly,[20] which may lead to low-power integrated nonlinear optics. The combination of slow light with low dispersion can be achieved with photonic crystal waveguides. In the literature, a number of strategies are proposed, for example by altering the hole radii alongside a photonic crystal waveguide[62] or by changing the shape of the holes.[107] A third option, which will be investigated in greater detail, is to vary the width of the waveguide.[54] The pulse tracking near-field microscope will be used to investigate slow light propagation with low dispersion.

Figures 6.10a and b present the photonic crystal waveguide under investigation. The waveguide is wider than the one shown in figure 6.1. In this case, the width is two rows of holes, instead of one. The air holes with radius 118 nm are etched in a hexagonal lattice in a 240 nm thick Si layer on top of SiO_2. The corresponding dispersion relation for TE-polarized light is depicted in figure 6.10c. Multiple modes can be discerned in this figure, denoted A, B and C. In addition, the magnitude of the wavevectors in bulk SiO_2 are depicted with the dashed gray line. This line is called the light line of SiO_2. All modes of the photonic crystal waveguide with wavevectors left of this line can couple from the waveguide to the bulk SiO_2, which is a significant loss channel in photonic crystal waveguides. The modes with wavevectors right of the light line are bound to the waveguide and can propagate without radiative losses.

With this property in mind, only two modes propagate with low losses through the waveguide: mode A with wavevectors between $k = -0.4$ and -0.5 (in units $2\pi/a$), and mode B in the same wavevector range. The curve of mode B shows close similarities with the mode in figure 6.2a. It is therefore a reasonable assumption, that the dispersion would also be similar to the dispersion discussed in the previous section, where at a v_g of c/9, a very strong asymmetric distortion of the pulses is observed as they propagate through a W1 photonic crystal waveguide. Mode A, however, has a much more homogeneous slope left of the light line, indicated by the arrow in figure 6.10c. The homogeneous slope suggests, that the group velocity is low, while the dispersion is small.

The propagation of pulses through this waveguide is investigated with the pulse tracking microscope. Femtosecond pulses are coupled into the waveguide with a central frequency of 0.278 with a spectral FWHM of 0.004, thus slightly exceeding the bandwidth of mode "A" left of the light line. The result of a series of pulse tracking experiments is shown in figure 6.11. In figure 6.11a, several modes are already excited in the photonic crystal waveguide. These are the modes already discussed (TE) and possibly also unwanted modes with the polarization along the direction of the pores (TM), though these have a much lower amplitude. In the consecutive images in figures 6.11b-j the propagation of the various modes is observed. Since some of the modes propagate with different group velocities or are excited at slightly different time, they can be observed as individual pulses.

One mode resides in the waveguide for the longest period of time and exits the scanned area after approximately 16 ps. This mode is the slow mode with wavevectors in the range of $k = 0.4 \ldots 0.5$. An analysis of the group velocity, as is performed in section 2.4.4, reveals that the group velocity of this slow mode is c/25. The velocity corresponds nicely to what is expected based on the slope of mode A at $\omega = 0.278$ in figure 6.10c.

The fact that the wave propagates at a low group velocity may not come as a surprise, given the knowledge from the dispersion relation. More interesting is the shape of the pulse as it propagates. In figure 6.11, the pulse with the low group velocity does not appear to broaden. This is quite in contrast to the slow mode in section 6.2 (see figure 6.3), that broadens very rapidly within 106 μm of propagation even though it is faster than the slow

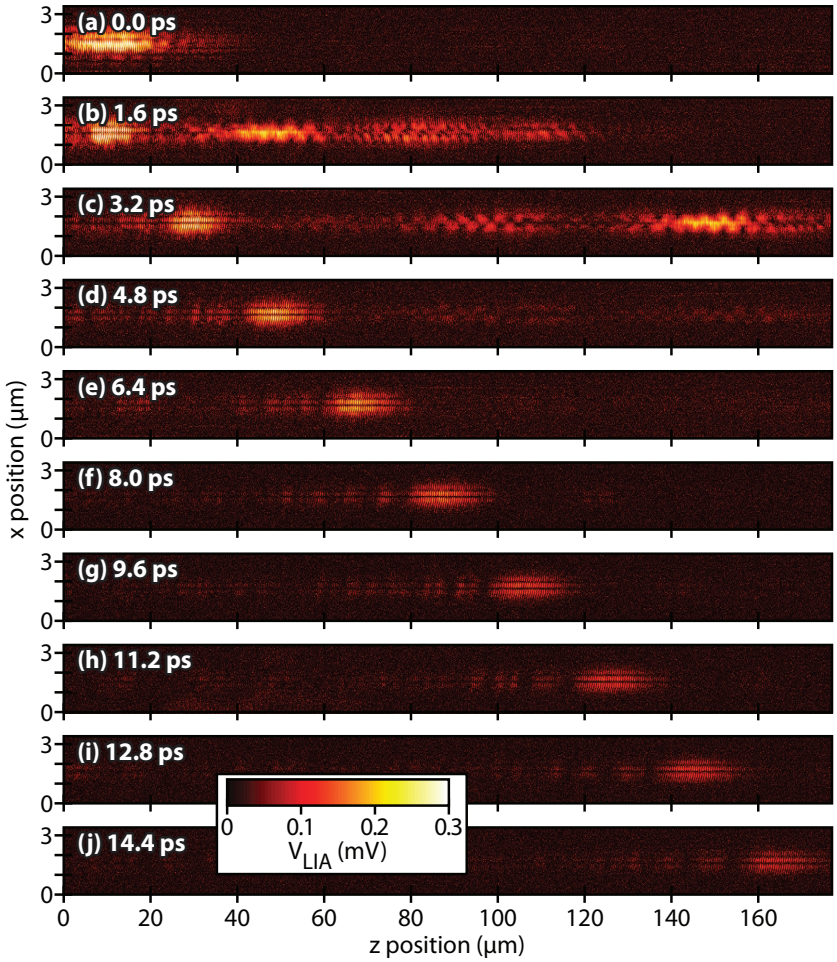

Figure 6.11: A series of pulse tracking measurements on a W2 photonic crystal waveguide. (a-j) Amplitude of the lock-in signal of the same area ($176 \times 3.4\ \mu m^2$) of the waveguide. Several modes are excited in the waveguide at 0 ps. The modes can be resolved individually in (b) and (c), due to different group velocities. The group velocity of the slowest mode, which can be seen throughout (b) up to (j) is c/25.

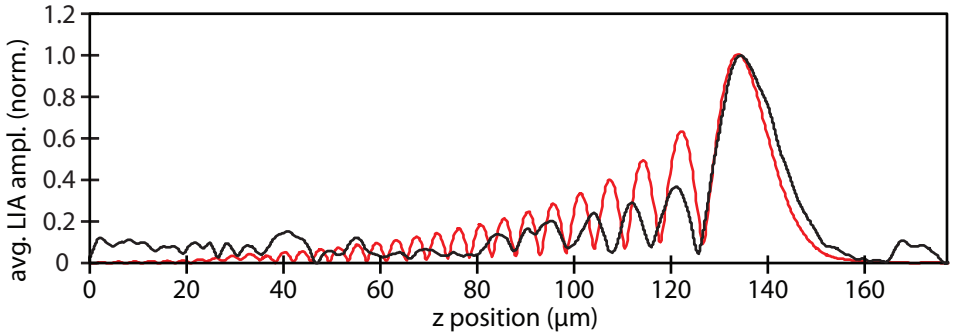

Figure 6.12: In black is shown the interference amplitude of the slow pulse measured at 12.0 ps delay time, see figure 6.11. The data is filtered to show only the wavevectors in the range of $-0.37 > k > -0.5$ (in units $2\pi/a$), corresponding to the slow mode.[54] The red curve shows the corresponding result of a calculation using the dispersion relation shown in figure 6.10c. In the calculation we included a cut-off of the spectrum, and a group-velocity dependent decay of the spectrum.

mode in figure 6.11 (c/9 vs. c/25). The slow pulse in figure 6.11 retains its shape even after a propagation distance of 165 μm. Only the amplitude of the pulse decreases upon propagation, which is a known issue for slow light in photonic crystals.[39,81]

On close examination of figure 6.11, one can see a pattern trailing the slow-light pulse. This trailing pattern is more easily seen in figure 6.12. In order to obtain the curve in this figure, the measured V_{LIA} distribution is filtered to contain only the wavevectors in the range of $-0.37 > k > -0.5$. This filtered data is subsequently averaged in the direction perpendicular to the waveguide to yield an average amplitude as a function of position z. Figure 6.12 shows the data corresponding to the delay time of 12.0 ps. In the figure, the maximum interference signal is found at 134 μm. At smaller distances, trailing fringes are clearly resolved.

The experimental results are compared to theory. For this comparison, equation 6.2 is solved numerically. Since the bandwidth of the used pulses is larger than the bandwidth of the slow mode, we changed the spectrum of $E_{sig}(\omega)$ with respect to the light in the reference branch. The dispersion relation used is the same as in figure 6.10c. Also, the decay of the light depends strongly on the group velocity. Therefore, a v_g-dependent loss is included in the calculations. The resulting interference amplitude as a function of distance is plotted in red in figure 6.12 and shows good agreement with the measurement data. The fringes on the trailing edge are caused by higher order dispersion, of which TOD is the most prominent. In addition, fringes are in part also present due to the cut-off of the spectrum of the pulse due to the finite admitted bandwidth of the structure. However, the fact that the pulses still stay relatively compact, makes the waveguide studied in this section promising

for slow light applications.

6.6 Discussion and conclusions

Figure 6.12 illustrates that the pulses can indeed be transmitted with low dispersion. Although the group velocity dispersion is indeed low, the trailing fringes of the pulses show that higher-order dispersion is significant. If we compare the two waveguides used in this chapter, at the group velocity of $c/25$, we find that the W1 waveguide has a β_2, which is 9 times higher than the W2 waveguide. There is also a significant difference in third-order dispersion, which is a factor of 7 lower in the W2 waveguide.

We have studied the dispersion of ultrafast pulses in a photonic crystal waveguide in both experiment and theory. We locally probed the light in the waveguide with an near-field technique and monitored the pulse shapes with an interferometer. At several waveguide positions, the shape of the obtained interferogram in time was analyzed. For ultrafast pulses, we find that as the propagation length increases, the envelope of the measured interferogram becomes asymmetrically. We have modeled the interferometric measurements for comparison between experiment and theory. Our model shows that the shape of the interferogram is a direct measure for the shape of the pulse envelope in the photonic crystal waveguide, and therefore the pulses in the waveguide must also be asymmetric in time. We find that the increased higher-order dispersion has a large effect on the pulse asymmetry, even at relatively high group velocities. Depending on the incident optical frequency, the group velocity varied between $0.188(5) \cdot c$ and $0.108(9) \cdot c$. Though these group velocities are moderately low, the found values for GVD and TOD are already substantial. We have quantified the GVD from our measurements, and found anomalous dispersion up to $\beta_2 = -1.1(3) \cdot 10^6$ ps^2/km. Similarly, the TOD is found to be very large: values up to $\beta_3 = 1.1(4) \cdot 10^5$ ps^3/km are found. These parameters are sufficient to simulate the dispersive effects of a femtosecond pulse traveling through our photonic crystal waveguide at a moderate speed of $0.116 \cdot c$. As the group velocity reduces further, even higher-order dispersive terms will start to play a role. Especially at these lower optical frequencies the common approach, to approximate the dispersive properties by a Taylor expansion, is only valid if many orders of the expansion are included. We have found that the effect of higher-order dispersion in a typical photonic crystal (waveguide) strongly increases when the group velocity decreases.

Slow light devices could find their application in optical data processing. Delay times in the picosecond or nanosecond regime would be useful. In any slow-light application a trade-off between bandwidth and device size has to be found: device sizes can be reduced by exploiting slower light, but usually at the expense of large dispersion and hence a reduction of the useful bandwidth. If the studied W1 waveguide were to be used for the delaying of a 1 ps pulse by 1 ns with respect to air, the pulse would be elongated (mainly by GVD) to 0.16 ns,

if a relatively high group velocity would be chosen ($c/10$). However, if one exploits a lower group velocity, for example $c/50$ to achieve the same delay, the elongation would be up to 4 times larger (approximately 0.5 ns) and the pulse shape would become asymmetric, due to the increased higher-order dispersion. In this respect, the large higher-order dispersion in the studied W1 waveguide makes the simple geometry an unlikely candidate for slow-light applications. However, in photonic crystals, one has the freedom to selectively alter the dispersive properties by changing the geometry of the lattice, or even by using combinations of lattices. We showed that the second and third order dispersion can be reduces by factors 9 and 7 respectively, by merely changing the width of the waveguide. Additional engineering of the dispersion can reduce the dispersion even further. This dispersion engineering has for example already been demonstrated by changing the radius of the holes alongside the waveguide.[62] This freedom has to be exploited to create large-bandwidth slow-light that does not suffer from dispersion.

7

Tracking pulses in *k*-space

The propagation of light through photonic crystal structures is governed by their photonic eigenstates and the coupling between these states. Here we investigate the propagation of light pulses through a photonic crystal device in real-time. Analysis of the photonic eigenstates in k-space allows different states to be identified. By tracking the evolution of the eigenstates both in k-space and in time, we uncover the dynamics of the eigenstates and the coupling between them on a femtosecond time-scale.

7.1 Introduction

Periodic structures have a large influence on propagating waves. This property holds for various types of waves over a large range of length scales: from electrons in atomic crystals,[71] light in photonic crystals,[6,14,108] to acoustic waves in sonic crystals.[109] The eigenstates of these waves are best described with a bandstructure, which represents the relation between energy and wavevector (k). This relation is usually not straightforward: due to the imposed periodicity, bands are folded into every Brillouin zone, inducing splitting of bands and appearance of bandgaps. As a result, exciting phenomena like negative refraction,[110,111] auto-collimation of waves[112,113] and low group velocities[18,19,114] arise. *k*-space investigations of electronic eigenstates have already yielded new insights into the behavior of electrons at surfaces and in novel materials.[115–118] However, for a complete characterization of a structure, also understanding of the mutual coupling of eigenstates is essential. We investigated the propagation of light pulses through a photonic crystal structure using a near-field microscope.[41,119] Tracking the evolution of the photonic eigenstates in both *k*-

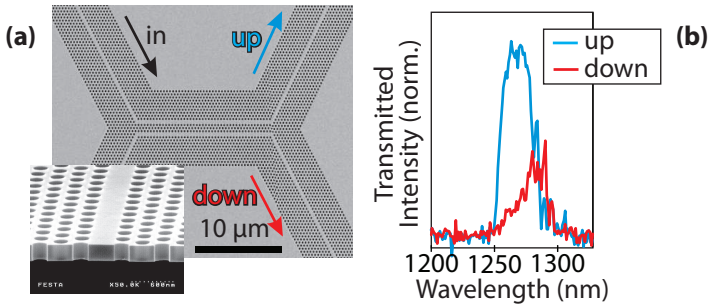

Figure 7.1: Photonic crystal sample and transmission. (a) Scanning electron microscope image of the sample, with two input waveguides (left) and two output waveguides (right). The directional coupler (center) is 45 lattice periods long. The inset shows a close-up of the membrane facet. (b), Transmission spectra of the device for both output ports. The device transmits light in the wavelength range between 1250 and 1290 nm. Most light is transmitted to the upper output waveguide, but at larger optical wavelengths the coupling to the lower output waveguide increases.

space and time allows us to identify individual eigenstates, uncovered their dynamics and coupling to other eigenstates on femtosecond time-scales even when co-localized in real space and time.

7.2 Photonic crystal structure

The structure under investigation is a two-dimensional photonic crystal structure, consisting of air holes (period $a = 339$ nm, radius 102 nm) in a GaAs membrane (thickness 250 nm), that has a 2D photonic bandgap between vacuum wavelengths 1220 nm and 1350 nm, in which we fabricated a so-called directional coupler with two input waveguides and two output waveguides (figure 7.1a) by leaving single rows of holes unperforated. The waveguides were chosen as they support only a single eigenstate at the polarization and the frequencies used in the experiment, which simplifies a k-space analysis. In the directional coupler, two waveguides run parallel, allowing the light to couple from the upper to the lower waveguide and vice versa. While seemingly a simple photonic structure, the propagation of light through it already involves many photonic eigenstates and coupling between these states. Different orientations of the waveguides are present in the device resulting in eigenstates represented in k-space by different wavevectors. At the coupling section the waveguides interact resulting in new symmetric and anti-symmetric eigenstates. Figure 7.1b shows the experimentally determined (time-averaged) transmission of both the upper and lower output waveguides obtained from 'white-light' transmission measurements. This input-output analysis reveals a frequency-specific response owing to particular

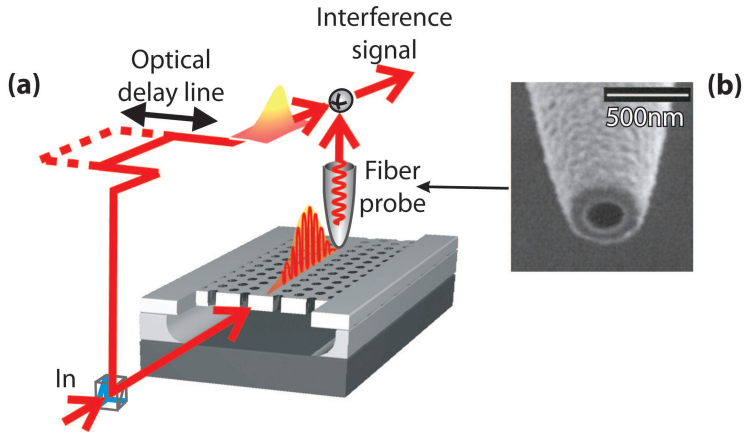

Figure 7.2: Schematic representation of the interferometric near-field setup. (a) The aluminum-coated near-field probe in (b), is scanned over the surface and collects a minute fraction of the propagating light. The collected light is mixed interferometrically with a reference beam. Only the resulting interference signal is recorded. The delay time in the experiment is controlled by the optical delay line.

eigenstates. By tracking these eigenstates in time, we will quantitatively recover both the individual eigenstates as well as their coupling dynamics on a femtosecond time-scale.

7.3 Time-resolved experiments

We investigated the propagation of light in the PhC structure with a phase-sensitive and time-resolved near-field microscope, which is schematically depicted in figure 7.2a. Femtosecond laser pulses (center wavelength 1260 nm, spectral width 12 nm), are launched into the structure, see also figure 7.2a. The evanescent field of the propagating light is probed locally by a metal-coated tapered optical fiber (figure 7.2b). The spatial resolution is better than the so-called diffraction limit and is to first approximation determined by the size of the aperture (250 nm). The choice of the aperture diameter is a trade-off between higher resolution at smaller diameter and a strong decrease of the throughput as the diameter is decreased. The collected light is interferometrically mixed with a reference pulse from the same pulsed laser source. When the probe is scanned over the surface of the sample, the optical path length of the sample branch changes. Therefore, interference maxima and minima are obtained, depending on the phase of the light in the sample relative to the phase of the reference pulse. Due to the duration of the laser pulses, interference will only be detected if there is sufficient time-overlap between the pulses in the reference and sample branch. In this way, the scan will result in a spatial map of the interference, which gen-

erally appears like a "snapshot" of the propagating pulse.[55] The instant at which such a "snapshot" is recorded, is determined by the arrival time of the reference pulse, also called "delay time". Figure 7.3a-f shows the result of a series of near-field measurements at 1260 nm were the transmission efficiency through the structure is high (see figure 7.1b). The orientation of the image is equal to that of figure 7.1a.

The optical signal is depicted in red and blue representing positive and negative E-fields. The inset shows a section of the input waveguide, where the phase evolution of the propagating light is clearly resolved. At the delay time defined 0.00 ps, the pulse is found to be located in the input waveguide. When we map the optical field at increased delay times (figure 7.3b-f), we observe the pulse dynamics in the structure: after entering the directional coupler, the pulse propagates into the upper and lower output waveguides. In the last two images recorded at 1.60 and 2.00 ps, the pulse exits the structure, with most of the light exiting through the upper output waveguide.

7.4 *k*-space maps

The consecutive measurements in figure 7.3a-f show the real-time dynamics of a femtosecond pulse traveling through a photonic crystal device. Although the images demonstrate the basic dynamics of the light propagating in such a structure, a detailed understanding of the propagating light remains hidden, as to that end the interplay between the eigenstates needs to be uncovered. When the propagation of a specific eigenstate in a waveguide (also called a waveguide mode) is to be investigated, there are a number of challenges. The first difficulty is to determine how many eigenstates are excited, since these states are usually excited simultaneously and propagate along the same path: they are co-localized in real space and time. Secondly, when multiple states are excited, separating them to investigate each individual state is impossible. However, in a k-space analysis, we recover the wavevectors present. When the eigenstates have different wavevectors, the states can be separated in k-space, even when co-localized in real space. By evaluating the eigenstates in both k-space and in time, we recover both the characteristic of each state and the coupling dynamics between them. In our experiment, the spatial frequencies (the wavevectors) contained in the real-space images are recovered via a two-dimensional Fourier transform. In this way, we obtain the wavevectors, direction and the amplitude of the corresponding eigenstates. Recently, this method has been applied to the investigation of phononic crystals.[120] By recovering the wavevectors as a function of time, we can investigate the dynamics of the individual eigenstates.

The k-space image of the measurement at 0.00 ps is depicted in figure 7.3g. Two stripes are visible in this figure: these are the most prominent spatial frequencies contained in the light field in the input waveguide. The confinement of the light in a narrow structure, i.e., the waveguide in real space, results in the elongated features (stripes) in k-space, since a

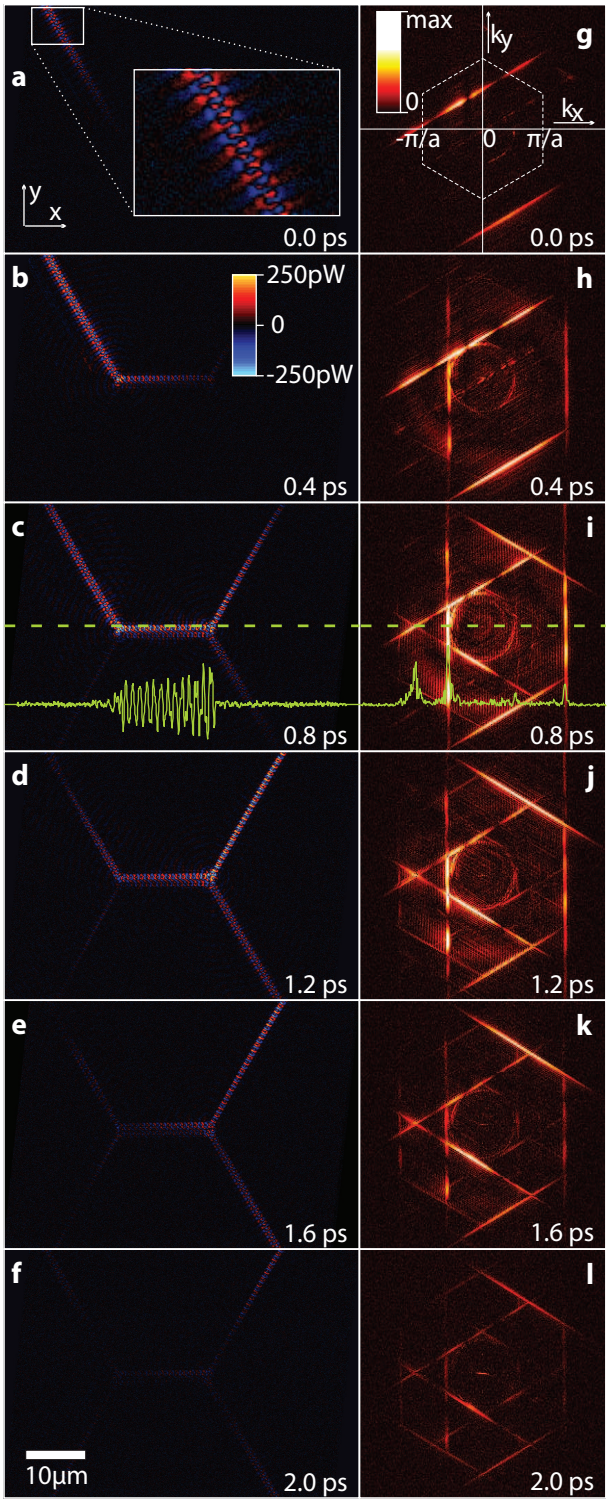

Figure 7.3: Pulse evolution in real space and ***k****-space. (a-f) Raw data obtained from an interferometric near-field measurement with delay times increasing from 0 to 2.0 ps. The background (of 0.40±0.02µW) is represented in black and the positive and negative interference values in red and blue, respectively. The consecutive images show an optical pulse entering the structure through the upper input waveguide and exiting the structure through both output waveguides. The inset of (a) shows a close-up of the measurement at 0 ps. (g-l) show the k-space map corresponding to (a) up to (f). In each k-space map, the eigenstates are visible as bright features. As time progresses, light couples sequentially to multiple eigenstates, since new features appear in k-space. The first Brillouin zone of the lattice is given by the dashed hexagon in (g). The image orientation (k_x,k_y) corresponds to (x,y) in (a-f). Line traces of the data are depicted in green in (c) and (i), corresponding to the data under the dashed green lines.*

small feature in real space is build up by a large number of spatial frequencies. In effect, the shape of the stripe is directly related to the lateral mode profile by a Fourier relation. The elongation of the stripe in k-space is therefore perpendicular to the direction of the waveguide. Due to the long range periodicity of the optical field along the waveguide, we obtain well defined wavevectors in the direction of the waveguide. In this way, we have probed the eigenfunction of the light in the structure and have recovered the wavevectors corresponding to this optical field.

Note that we find two stripes in figure 7.3g, while only a single eigenstate is excited. This observation is a direct consequence of the Bloch wave nature of the guided light. The eigenfunction obeys Bloch's theorem, which means that a single eigenfunction is composed of multiple wavevectors[24] in such a way that the eigenfunction conforms to the imposed periodicity of the lattice. Therefore, the individual wavevectors, the Bloch harmonics, are spaced one reciprocal lattice vector apart in k-space. This spacing can also be observed in figure 7.3g, since the wavevectors are spaced one Brillouin zone (dashed hexagon) apart. There are also harmonics with larger wavevectors but these could not be resolved in our k-space maps due to their low amplitude. Together the two harmonics shown represent more than 99% of the energy in the eigenstate. Interestingly, each Bloch harmonic has a different amplitude profile: the two k-space features have a different structure perpendicular to the propagation direction. This difference can be understood by realizing that in general the spatial mode pattern is more complicated close to the holes than in the center of the waveguide. A complicated pattern requires the mixing of more harmonics,[60] with amplitudes such that together they form the pattern.

As the delay time is increased to 0.40 ps (figure 7.3h), we observe two new features, now with an elongation in the vertical direction. These vertical stripes correspond to the eigenstates of the directional coupler. We find both a positive and a negative wavevector at $k_x = 1.43\pi/a$ and $k_x = -0.57\pi/a$, respectively. The coupling in the directional coupler occurs due to a coherent superposition of a symmetric and anti-symmetric eigenstate, that have a slightly different wavevector. At the frequency used, the difference in k-vector is too small to be resolved in our k-space maps.

Two new stripes appear in figure 7.3i, corresponding to the Bloch mode in the upper output waveguide. Note that the light in the lower output waveguide does not give rise to new feature in k-space, because the waveguide geometry and direction are identical to the input waveguide. The k-space features therefore overlap with the wavevectors of the input waveguide.

Above, we discussed the evolution of the three most prominent eigenstates found in k-space during a time interval of 2.0 ps. In addition other, less pronounced eigenstates are present, for example those that show up as a circle of radius $0.54\pi/a$ around the origin. The circular shape indicates equally long wavevectors in every direction. In fact, the wavevectors correspond to light skimming over the surface in every direction, originating from scattering at the intersections. We also find evidence for reflections at the intersections: a reflected

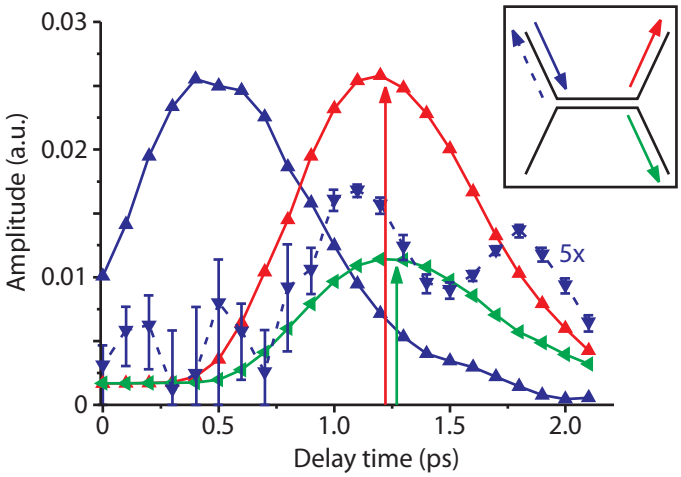

Figure 7.4: Amplitude in each eigenstate as a function of time. Evolution of the amplitude in each of the most pronounced eigenstates as time progresses, determined from the k-space images. The blue line represents the amplitude in the input waveguide. The light traveling backward in the input waveguide is depicted by the dashed blue line (5 times magnified), where the error bars are proportional to the noise of the Fourier Transform. The red and green arrows depict the exit time of the corresponding output pulses, determined by the center-of-mass of the time versus intensity curves (amplitude squared). The time difference between the output pulses is 70±20 fs. The inset shows a schematic of the position and propagation direction of the eigenstates.

wave with an initial wavevector $\mathbf{k}$ will have a reflected wavevector $-\mathbf{k}$, an equally large wavevector in the opposite direction. Indeed, in figure 7.3k two vertical features are found at $k_x = -1.43$ and $0.57\pi/a$. This is the eigenstate corresponding to reflected light and propagates back in the directional coupler in the $-\mathbf{x}$-direction. Similarly, also an eigenstate is found, associated with backward propagating light in the input waveguide.

Since we have recovered the wavevectors of the device eigenstates, we can now investigate the individual states by selecting their wavevectors in k-space. To demonstrate this approach, we studied the amplitude of the light in the input waveguide, the two output waveguides and the reflected light into the upper input waveguide. As the eigenstate in one of the output waveguides has the same signature in k-space as the input waveguide, we performed a selection in real space to separate the two.

The results are depicted in figure 7.4. At each delay time, the real-space image is split into three sections: the upper input waveguide and the lower and upper output waveguides. A Fourier transform of each of these real-space images gives three k-space images, cor-

responding to the three waveguides. The E-field amplitude of the eigenstates in each of the waveguides is recovered by summation of the amplitude of the two Bloch harmonics at $|\mathbf{k}|$=0.57 π/a and -1.43 π/a. The amplitude pattern of the harmonics does not play a role, since we sum over the full width of de k-space pattern perpendicular to the waveguide direction. The blue curve indicated by a continuous line indicates the amplitude of the mode in the input waveguide (as it propagates towards the directional coupler). The maximum amplitude is found around 0.5 ps: as soon as the mode couples to the modes of the directional coupler its amplitude decreases. The green and red curve show the amplitude of the light in the lower and upper output waveguide, respectively. From the height of the curves we obtain a splitting ratio of 1:5 (in intensity, or amplitude squared in favor of the upper output waveguide.

Interestingly, the two output pulses do not exit the directional coupler at the same time. The characteristic exiting time is indicated by the arrows. These times are calculated by evaluating the center-of-mass of the curves. Despite the identical path length for the two routes, the pulse in the lower output waveguide exits the directional coupler 70 ± 20 fs later than the pulse in the upper output waveguide. This difference can be understood by noting the spectral characteristics of the device in combination with pulse dispersion. From the transmission spectra in figure 7.1b, we know that the low-frequency components couple more efficiently to the lower output waveguide. Due to anomalous dispersion,[101] these low-frequency components arrive at a later time at the directional coupler, and therefore the output appears at a later time. The error of ± 20 fs has two main contributions: the error in determining the center-of-mass of the curves and a correction for the slightly different length of the measured output waveguides.

We have also analyzed the light reflected back into the upper input waveguide, due to reflections at the intersections, both at the right and the left side of the directional coupler. The reflected light is depicted in figure 7.4 by the dashed blue curve. The reflected amplitude in the measured stretch of the input waveguide has two main peaks, at 1.1 ps and 1.8 ps, respectively. The first peak corresponds to reflections at the left intersection and the second peak is caused by reflected light at the right intersection in the directional coupler. The peaks between 0 and 0.8 ps do not exceed the noise level in the k-space maps, which is depicted by the error bars in figure 7.4. The area under the curve of intensity versus delay time is proportional to the total energy reflected back into the upper input waveguide: in this case 2% of the input energy is reflected back.

7.5 Discussion and conclusions

Our measurement approach can be adopted to investigate and understand the behavior of any complex optical system where electro-magnetic waves are present at the surface, to probe its eigenstates, their relative amplitudes and their coupling in time. Care has to be

taken in determining the relative amplitudes of eigenstates or of their Bloch harmonics, as these may be detected with a different efficiency, which depends, for example, on wavevector. Also a number of oscillations of the optical field must be measured in order to assign a wavevector with a useful accuracy. Correspondingly, the concept of assigning wavevectors may not be very useful in small structures, for example in small-volume cavities. Nevertheless, the method is suited for the investigation of the majority of photonic crystal devices.

Moreover, it should be particularly exciting to implement the approach to probe novel classes of optical meta-materials where, for example, negative phase velocities and negative group velocities have been reported.[40] Our ability to observe the time-resolved interplay between eigenstates underlying the counter-intuitive properties of meta-materials, will spark exciting new avenues of research. Ultrafast, time-resolved studies on atomic systems in k-space have been limited to structural rearrangements of the crystal lattice itself.[121–123] The k-space representation of electronic eigenstates in time-averaged experiments has elucidated the properties of very diverse systems ranging from surfaces,[115] carbon nanotubes[117] to High-Tc superconductors.[116] Both of the techniques used, scanning tunneling microscopy[124] and angle-resolved photoemission,[125,126] can be modified to enable time-resolved measurements. Thus, tracking eigenstates in k-space like described in this chapter is, in principle, possible for electronic eigenstates. Such a development offers the exciting perspective of unraveling the dynamics and coupling of electronic states on a femtosecond timescale.

7

References

[1] W. Friedrich, P. Knipping, M. Von Laue, *Interferenz-Erscheinungen bei Röntgenstrahlen*, Proc. Bavarian Acad. Sci., 303 (1912).

[2] N.W. Ashcroft, N.D. Mermin, *Solid State Physics*, Harcourt Inc., Orlando, FL, USA (1976).

[3] E. Yablonovitch, *Inhibited Spontaneous Emission in Solid-State Physics and Electronics*, Phys. Rev. Lett. **58**, 2059 (1987).

[4] S. John, *Strong Localization of Photons in Certain Disordered Dielectric Superlattices*, Phys. Rev. Lett. **58**, 2486 (1987).

[5] E. Yablonovitch, T.J. Gmitter & K.M. Leung, *Photonic band structure: The face-centered-cubic case employing nonspherical atoms*, Phys. Rev. Lett. **90**, 2295 (1991).

[6] See for example, *Photonic Crystals and Light Localization in the 21st Century*, in *NATO Science Series*, C.M. Soukoulis, ed. (Kluwer Academic, Dordrecht, The Netherlands, 2001).

[7] A.C. Neville, *Metallic gold and silver colours in some insect cuticles*, J. Insect Physiol. **23**, 1267 (1977).

[8] P. Vukusic & I. Hooper, *Directionally controlled fluorescence emission in butterflies*, Science **310**, 1151 (2005).

[9] J.W.S. Rayleigh, *On the remarkable phenomenon of crystalline reflexion described by Prof. Stokes*, Phil. Mag. **26**, 256 (1888).

[10] J.C. Knight, J. Broeng, T.A. Birks et al., *Photonic bandgap guidance in optical fibers* Science **282**, 1476 (1998).

[11] J.E.G.J. Wijnhoven & W.L. Vos, *Preparation of photonic crystals made of air spheres in titania*, Science **281**, 802 (1998).

[12] T. Asano, B.S. Song & S. Noda, *Analysis of the experimental Q factors (similar to 1 million) of photonic crystal nanocavities*, Opt. Express, **14**, 1996 (2006).

[13] P. Lodahl, A.F. van Driel, I.S. Nikolaev et al., *Controlling the dynamics of spontaneous emission from quantum dots by photonic crystals*, Nature **430**, 654 (2004).

[14] M. Fujita, S. Takahashi, Y. Tanaka et al., *Simultaneous inhibition and redistribution of spontaneous light emission in photonic crystals*, Science **308**, 1296 (2005).

[15] A.A. Erchak, D.J. Ripin, S. Fan et al., *Enhanced coupling to vertical radiation using a two-dimensional photonic crystal in a semiconductor light-emitting diode*, Appl. Phys. Lett. **78**, 563 (2001).

[16] K. Hennessy, A. Badolato, M. Winger et al., *Quantum nature of a strongly coupled single quantum dot-cavity system*, Nature **445**, 896 (2007).

[17] M. Notomi, K. Yamada, A. Shinya et al., *Extremely large group-velocity dispersion of line-defect waveguides in photonic crystal slabs*, Phys. Rev. Lett. **87**, 253902 (2001).

[18] H. Gersen, T.J Karle, R.J.P. Engelen et al., *Real-space observation of ultraslow light in photonic crystal waveguides*, Phys. Rev. Lett. **94**, 073903 (2005).

[19] Y.A. Vlasov, M. O'Boyle, H.F. Hamann et al., *Active control of slow light on a chip with photonic crystal waveguides*, Nature **438**, 65 (2005).

[20] M. Soljačić & J.D. Joannopoulos, *Enhancement of nonlinear effects using photonic crystals*, Nature Mater. **3**, 211 (2004).

[21] H. Benisty, *Modal analysis of optical guides with two-dimensional photonic band-gap boundaries*, J. Appl. Phys. **79**, 7483 (1996).

[22] M. Born & E. Wolf, *Principles of optics*, (7th ed., Cambridge Univ. Press, Cambridge, UK, 1999).

[23] S. Noda, K. Tomoda, N. Yamamoto et al., *Full three-dimensional photonic bandgap crystals at near-infrared wavelengths*, Science **289**, 604 (2000).

[24] P.St.J. Russell, *Optics of Floquet-Bloch waves in dielectric gratings*, Appl. Phys. B **39**, 231 (1986).

[25] S. Noda, M. Yokoyama, M. Imada, et al., *Polarization mode control of two-dimensional photonic crystal laser by unit cell structure design*, Science **293**, 1123 (2001).

[26] E. Cubukcu, K. Aydin, E. Ozbay, et al., *Negative refraction by photonic crystals*, Nature **423**, 604 (2003).

[27] Y. Akahane, T. Asano, B.S. Song et al., *High-Q photonic nanocavity in a two-dimensional photonic crystal*, Nature **425**, 944 (2003).

[28] H.G. Park, S.H. Kim, S.H. Kwon, et al., *Electrically driven single-cell photonic crystal laser*, Science **305**, 1444 (2004).

[29] T. Yoshie, A. Scherer, J. Hendrickson et al., *Vacuum Rabi splitting with a single quantum dot in a photonic crystal nanocavity*, Nature **432**, 200 (2004).

[30] G. Lecamp, J.P. Hugonin & P. Lalanne, *Theoretical and computational concepts for periodic optical waveguides*, Opt. Express **15**, 11042 (2007).

[31] M. Lončar, D. Nedeljković, T.P. Pearsall et al., *Experimental and theoretical confirmation of Bloch-mode light propagation in planar photonic crystal waveguides*, Appl. Phys. Lett. **80**, 1689 (2002).

[32] S.G. Johnson, P.R. Villeneuve, S.H. Fan et al., *Linear waveguides in photonic-crystal slabs*, Phys. Rev. B **62**, 8212 (2000).

[33] S. Olivier, M. Rattier, H. Benisty et al., *Mini-stopbands of a one-dimensional system: The channel waveguide in a two-dimensional photonic crystal*, Phys. Rev. B **63**, 113311 (2001).

[34] P.E. Barclay, K. Srinivasan, M. Borselli et al., *Efficient input and output fiber coupling to a photonic crystal waveguide*, Opt. Lett. **29**, 697 (2004).

[35] Y. Raichlin, A. Millo & A., Katzir *Investigations of the structure of water using mid-IR fiberoptic evanescent wave spectroscopy*, Phys. Rev. Lett. **93**, 185703 (2004).

[36] D. Rychtarik, B. Engeser, H.C. Nagerl et al., *Two-dimensional Bose-Einstein condensate in an optical surface trap*, Phys. Rev. Lett. **92**, 173003 (2004).

[37] A.W. Snyder & J.D. Love, *Optical waveguide theory*, (Chapman & Hall, London, UK, 1983).

[38] G.P. Agrawal, *Nonlinear Fiber Optics*, (Academic Press, San Diego, CA, USA, 2001).

[39] S. Hughes, L. Ramunno, J.F. Young et al., *Extrinsic optical scattering loss in photonic crystal waveguides: Role of fabrication disorder and photon group velocity*, Phys. Rev. Lett. **94**, 033903 (2005).ch1

[40] G. Dolling, C. Enkrich, M. Wegener et al., *Simultaneous negative phase and group velocity of light in a metamaterial*, Science **312**, 892 (2006).

[41] S.I. Bozhevolnyi, V.S. Volkov, E. Devaux et al., *Channel plasmon subwavelength waveguide components including interferometers and ring resonators*, Nature **440**, 508 (2006).

[42] R.J.P. Engelen, Y. Sugimoto, H. Gersen et al., *Ultrafast evolution of photonic eigenstates in k-space*, Nature Phys. **3**, 401 (2007).

[43] L. Novotny & B. Hecht, *Principles of Nano-Optics*, (Cambridge Univ. Press, Cambridge, 2007).

[44] E.A. Igel & M. Kristiansen, *Rotating Mirror Streak and Framing Cameras*, (SPIE, Bellingham, WA, 1997).

[45] L. Zehnder, *Ein neuer Interferenzrefraktor*, Z. Instrumentenkunde **11**, 275 (1891).

[46] L. Mach, *Über einen Interferenzrefraktor*, Z. Instrumentenkunde **12**, 89 (1892).

[47] M.L.M. Balistreri, J.P. Korterik, L. Kuipers et al., *Local observations of phase singularities in optical fields in waveguide structures*, Phys. Rev. Lett. **85**, 294 (2000).

[48] R. Hillenbrand & F. Keilmann, *Complex optical constants on a subwavelength scale*, Phys. Rev. Lett. **85**, 3029 (2000).

[49] A. Nesci, R. Dändliker & H.P. Herzig, *Quantitative amplitude and phase measurement by use of a heterodyne scanning near-field optical microscope*, Opt. Lett. **26**, 208 (2001).

[50] A. Nesci & Y. Fainman, *Complex amplitude of an ultrashort pulse with femtosecond resolution in a waveguide using a coherent NSOM at 1550 nm*, in "Wave Optics and Photonic Devices for Optical Information Processing II", P. Ambs and F. R. Beyette, Jr., eds., Proc. SPIE **5181**, 62 (2003).

[51] L. Gomez, R. Bachelot, A. Bouhelier et al., *Apertureless scanning near-field optical microscopy: a comparison between homodyne and heterodyne approaches*, J. Opt. Soc. Am. B **23**, 823 (2006).

[52] A.E. Siegman, *Lasers*, (Univ. Science Books, Mill Valley, CA, U.S.A., 1986)

[53] M. Young, *Optics and lasers: Including fibers and optical waveguides*, (Springer series in optical sciences 14/2, Springer Verlag, Berlin, Germany, 1986)

[54] M.D. Settle, R.J.P. Engelen, M. Salib et al., *Flatband slow light in photonic crystals featuring spatial pulse compression and terahertz bandwidth*, Opt. Express **15**, 219 (2007).

[55] M.L.M. Balistreri, H. Gersen, J.P. Korterik et al., *Tracking femtosecond laser pulses in space and time*, Science **294**, 1080 (2001).

[56] I. Newton, *Opticks: or, a Treatise of the Reflections, Refractions, Inflections and Colours of Light* (4th ed., William Innys, London, 1730), Book III, Qu. 29, 346.

[57] M. Cai, O. Painter & K.J. Vahala, *Observation of critical coupling in a fiber taper to a silica-microsphere whispering-gallery mode system*, Phys. Rev. Lett. **85**, 74 (2000).

[58] L. Kastrup, H. Blom, C. Eggeling et al., *Fluorescence fluctuation spectroscopy in subdiffraction focal volumes*, Phys. Rev. Lett. **94**, 178104 (2005).

[59] S.I. Bozhevolnyi, V.S. Volkov, T. Sondergaard et al., *Near-field imaging of light propagation in photonic crystal waveguides: Explicit role of Bloch harmonics*, Phys. Rev. B **66**, 235204 (2002).

[60] H. Gersen, T.J. Karle, R.J.P. Engelen et al., *Direct observation of Bloch harmonics and negative phase velocity in photonic crystal waveguides*, Phys. Rev. Lett. **94**, 123901 (2005).

[61] I.P. Radko, S.I. Bozhevolnyi & N. Gregersen, *Transfer function and near-field detection of evanescent waves*, Appl. Opt. **45**, 4054 (2006).

[62] L.H. Frandsen, A.V. Lavrinenko, J. Fage-Pedersen et al., *Photonic crystal waveguides with semi-slow light and tailored dispersion properties*, Opt. Express **14**, 9444 (2006).

[63] D. Mori & T. Baba, *Dispersion-controlled optical group delay device by chirped photonic crystal waveguides*, Appl. Phys. Lett. **85**, 1101 (2004).

[64] T.J. Karle, Y.J. Chai, C.N. Morgan et al., *Observation of Pulse Compression in Photonic Crystal Coupled Cavity Waveguides*, J. Lightwave Technol. **22**, 514 (2004).

[65] E. Schonbrun, Q. Wu, W. Park et al., *Polarization beam splitter based on a photonic crystal heterostructure*, Opt. Lett. **31**, 3104 (2006).

[66] H. Nakamura, Y. Sugimoto, K. Kanamoto et al., *Ultra-fast photonic crystal/quantum dot all-optical switch for future photonic networks*, Opt. Express **12**, 6606 (2004).

[67] T. Baba, D. Mori, K. Inoshita et al., *Light localizations in photonic crystal line defect waveguides*, IEEE J. Sel. Top. Quantum Electron. **10**, 484 (2004).

[68] S.G. Johnson P. Bienstman, M.A. Skorobogatiy et al., *Adiabatic theorem and continuous coupled-mode theory for efficient taper transitions in photonic crystals*, Phys. Rev. E **66**, 066608 (2002).

[69] P. Tortora M. Abashin, I. Märki et al., *Observation of amplitude and phase in ridge and photonic crystal waveguides operating at 1.55 μm by use of heterodyne scanning near-field optical microscopy*, Opt. Lett. **30**, 2885 (2005).

[70] R.J.P. Engelen, Y. Sugimoto, Y. Watanabe et al., *The effect of higher-order dispersion on slow light propagation in photonic crystal waveguides*, Opt. Express **14**, 1658 (2006).

[71] F. Bloch, *Uber die Quantenmechanik der Elektronen in Kristallgittern*, Z. Physik **52**, 555 (1928).

[72] J.A. Veerman, A.M. Otter, L. Kuipers et al., *High definition aperture probes for near-field optical microscopy fabricated by focused ion beam milling*, Appl. Phys. Lett. **72**, 3115 (1998).

[73] K. Edagawa, S. Kanoko & M. Notomi, *Photonic amorphous diamond structure with a 3D photonic band gap*, Phys. Rev. Lett. **100**, 013901 (2008).

[74] A. Berrier M. Mulot, M. Swillo et al., *Negative Refraction at Infrared Wavelengths in a Two-Dimensional Photonic Crystal*, Phys. Rev. Lett. **93**, 073902 (2004).

[75] R.D. Meade, K.D. Brommer, A.M. Rappe, et al., *Novel applications of photonic band gap materials*, J. Appl. Phys. **75**, 4753 (1994).

[76] A.F. Koenderink, A. Lagendijk & W.L. Vos, *Optical extinction due to intrinsic structural variations of photonic crystals*, Phys. Rev. B **72**, 153102 (2005).

[77] J. Topolancik, B. Ilic & F. Vollmer, *Experimental Observation of Strong Photon Localization in Disordered Photonic Crystal Waveguides*, Phys. Rev. Lett. **99**, 253901 (2007).

[78] J. Bertolotti, S. Gottardo, D.S. Wiersma et al., *Optical Necklace States in Anderson Localized 1D Systems*, Phys. Rev. Lett. **94**, 113903 (2005).

[79] D. Gerace & L. C. Andreani, *Disorder-induced losses in photonic crystal waveguides with line defects*, Opt. Lett. **29**, 1897 (2004).

[80] Y. Tanaka Y. Sugimoto, N. Ikeda et al., *Group velocity dependence of propagation losses in single-line-defect photonic crystal waveguides on GaAs membranes*, Electronics Lett. **40**, 174 (2004).

[81] E. Kuramochi, M. Notomi, S. Hughes et al., *Disorder-induced scattering loss of line-defect waveguides in photonic crystal slabs*, Phys. Rev. B **72**, 161318 (2005).

[82] L. O'Faolain, T.P. White, D. O'Brien et al., *Dependence of extrinsic loss on group velocity in photonic crystal waveguides*, Opt. Express **15**, 13129 (2007).

[83] Z.Y. Li & K.M. Ho, *Anomalous Propagation Loss in Photonic Crystal Waveguides*, Phys. Rev. Lett. **92**, 063904 (2004).

[84] M. Sandtke R.J.P. Engelen, H. Schoenmaker, et al., *Novel instrument for surface plasmon polariton tracking in space and time*, Rev. Sci. Instrum. **79**, 013704 (2008).

[85] M. Gurioli F. Bogani, L. Cavigli et al., *Weak Localization of Light in a Disordered Microcavity*, Phys. Rev. Lett. **94**, 183901 (2005).

[86] J.P. Hugonin P. Lalanne, T.P. White et al., *Coupling into slow-mode photonic crystal waveguides*, Opt. Lett. **32**, 2638 (2007).

[87] P. Pottier, M. Gnan & R.M. De La Rue, *Efficient coupling into slow-light photonic crystal channel guides using photonic crystal tapers*, Opt. Express **15**, 6569 (2007).

[88] V.N. Astratov, R.M. Stevenson, I.S. Culshaw et al., *Heavy photon dispersions in photonic crystal waveguides*, Appl. Phys. Lett. **77**, 178 (2000).

[89] K. Inoue, N. Kawai, Y. Sugimoto et al., *Observation of small group velocity in two-dimensional AlGaAs-based photonic crystal slabs*, Phys. Rev. B **65**, 121308 (2002).

[90] M. Notomi, A. Shinya, S. Mitsugi et al., *Optical bistable switching action of Si high-Q photonic-crystal nanocavities*, Opt. Express **13** 2678 (2005).

[91] A. Sugitatsu, T. Asano T & S. Noda, *Characterization of line-defect-waveguide lasers in two-dimensional photonic-crystal slabs*, Appl. Phys. Lett. **84** 5395 (2004).

[92] S.F. Mingaleev, Yu.S. Kivshar & R.A. Sammut, *Longrange interaction and nonlinear localized modes in photonic crystal waveguides*, Phys. Rev. E **62** 5777 (2000).

[93] M.D. Rahn, A.M. Fox, M.S. Skolnick et al., *Propagation of ultrashort nonlinear pulses through two-dimensional AlGaAs high-contrast photonic crystal waveguides*, J. Opt. Soc. Am. B **19**, 716 (2002).

[94] S. Yamada, Y. Watanabe, Y. Katayama et al., *Simulation of optical pulse propagation in a two-dimensional photonic crystal waveguide using a high accuracy finite-difference time-domain algorithm*, J. Appl. Phys. **93**, 1859 (2003).

[95] A. Imhof, W.L. Vos, R. Sprik et al., *Large dispersive effects near the band edges of photonic crystals*, Phys. Rev. Lett. **83**, 2942 (1999).

[96] T. Asano, K. Kiyota, D. Kumamoto et al., *Time-domain measurement of picosecond light-pulse propagation in a two-dimensional photonic crystal-slab waveguide*, Appl. Phys. Lett. **84**, 4690 (2004).

[97] M. Miyagi & S. Nishida, *Pulse spreading in a single-mode fiber due to third-order dispersion*, Appl. Opt. **18**, 678 (1979).

[98] J. Khurgin, *Performance of nonlinear photonic crystal devices at high bit rates*, Opt. Lett. **30**, 643 (2005).

[99] S.G. Johnson & J.D. Joannopoulos, *Block-iterative frequency-domain methods for Maxwell's equations in a planewave basis*, Opt. Express **8** 173 (2001).

[100] Y. Sugimoto, Y. Tanaka, N. Ikeda et al., *Low propagation loss of 0.76 dB/mm in GaAs-based single-line-defect two-dimensional photonic crystal slab waveguides up to 1 cm in length*, Opt. Express **12**, 1090 (2004).

[101] R.J.P. Engelen, T.J. Karle, H. Gersen et al., *Local probing of Bloch mode dispersion in a photonic crystal waveguide*, Opt. Express, **13**, 4457 (2005).

[102] Product information sheet, *Corning SMF-28e Optical Fiber, Product Information*, (Corning Inc., 2005).

[103] P. Sanchis, P. Bienstman, B. Luyssaert et al., *Analysis of butt coupling in photonic crystals*, IEEE J. Quantum Electron. **40**, 541 (2004).

[104] H. Gersen, E.M.P.H. van Dijk, J.P. Korterik et al., *Phase mapping of ultrashort pulses in bimodal photonic structures: A window on local group velocity dispersion*, Phys. Rev. E **70**, 066609 (2004).

[105] M.L.M. Balistreri, A. Driessen, J.P. Korterik et al., *Quasi interference of perpendicularly polarized guided modes observed with a photon scanning tunneling microscope*, Opt. Lett. **25**, 637 (2000).

[106] E. Chow, S. Y. Lin, J. R. Wendt et al., *Quantitative analysis of bending efficiency in photonic-crystal waveguide bends at λ=1.55 μm wavelengths*, Opt. Lett. **26**, 286 (2001).

[107] A. Saynatjoki, M. Mulot, J. Ahopelto et al., *Dispersion engineering of photonic crystal waveguides with ring-shaped holes*, Opt. Express **15**, 8323 (2007).

[108] A.F. Koenderink, M. Kafesaki, C.M. Soukoulis et al., *Spontaneous emission in the near field of two-dimensional photonic crystals*, Opt. Lett. **30**, 3210 (2005).

[109] F. Cervera, L. Sanchis, J.V. Sánchez-Pérez et al., *Refractive acoustic devices for airborne sound*, Phys. Rev. Lett. **88**, 023902 (2002).

[110] X. Hu, Y. Shen, X. Liu et al., *Superlensing effect in liquid surface waves*, Phys. Rev. E **69**, 030201 (2004).

[111] L. Feng, X.-P. Liu, M.-H Lu et al., *Acoustic backward-wave negative refractions in the second band of a sonic crystal*, Phys. Rev. Lett. **96**, 014301 (2006).

[112] G. Mahieu, B. Grandidier, D. Deresmes et al., *Direct evidence for shallow acceptor states with nonspherical symmetry in GaAs*, Phys. Rev. Lett. **94**, 026407 (2005).

[113] Z.L. Lu, S. Shi, J.A. Murakowski et al., *Experimental demonstration of self-collimation inside a three-dimensional photonic crystal*, Phys. Rev. Lett. **96**, 173902 (2006).

[114] R.P. Feynman, R.W. Hellwarth, C.K. Iddings et al., *Mobility of slow electrons in a polar crystal*, Phys. Rev. **127**, 1004 (1962).

[115] M.F. Crommie, C.P. Lutz & D.M. Eigler, *Imaging standing waves in a 2-dimensional electron gas*, Nature **363**, 524 (1993).

[116] Z.X. Shen, W.E. Spicer, D.M. King et al., *Photoemission-studies of high-T-c superconductors – the superconducting gap*, Science **267**, 343 (1995).

[117] S.G. Lemay, J.W. Janssen, M. van den Hout et al., *Two-dimensional imaging of electronic wavefunctions in carbon nanotubes*, Nature **412**, 617 (2001).

[118] K. McElroy, R.W. Simmonds, J.E. Hoffman et al., *Relating atomic-scale electronic phenomena to wave-like quasiparticle states in superconducting* $Bi_2Sr_2CaCu_2O_{8+\delta}$, Nature **422**, 592 (2003).

[119] E. Betzig & J.K. Trautman, *Near-field optics - microscopy, spectroscopy, and surface modification beyond the diffraction limit*, Science **257**, 189 (1992).

[120] D.M. Profunser, O.B. Wright & O. Matsuda, *Imaging ripples on phononic crystals reveals acoustic band structure and Bloch harmonics*, Phys. Rev. Lett. **97**, 055502 (2006).

[121] A. Rousse, C. Rischel, S. Fourmaux et al., *Non-thermal melting in semiconductors measured at femtosecond resolution*, Nature **410**, 65 (2001).

[122] M. Greiner, O. Mandel, T. Esslinger et al., *Quantum phase transition from a superfluid to a Mott insulator in a gas of ultracold atoms*, Nature **415**, 39 (2002).

[123] B.J. Siwick, J.R. Dwyer, R.E. Jordan et al., *An atomic-level view of melting using femtosecond electron diffraction*, Science **302**, 1382 (2003).

[124] H. Shigekawa, O. Takeuchi & M. Aoyama, *Development of femtosecond time-resolved scanning tunneling microscopy for nanoscale science and technology.*, Sci. Technol. Adv. Mater. **6** 582 (2005).

[125] A.D. Damascelli, H. Lu, K.M. Shen et al., *Fermi Surface, Surface States, and Surface Reconstruction in* Sr_2RuO_4, Phys. Rev. Lett. **85**, 5194 (2000).

[126] P. Szymanski, S. Garrett-Roe & C.B. Harris, *Time- and angle-resolved two-photon photoemission studies of electron localization and solvation at interfaces*, Prog. Surf. Sci. **78**, 1 (2005).

Summary

Optical structures with dimensions down to nanometer length scales have been a topic for investigation for an increasing number of researchers, due to their intriguing physical properties and their possible new optical applications. Future applications are foreseen in optical data communication, quantum computing or all-optical switching. For all these applications, light needs to have a strong interaction with the material in which it propagates. Photonic crystals are a promising technology that might enable this. Photonic crystals are structures in which the refractive index varies periodically, by alternating materials with different refractive indices, for example silicon and air. If the period is comparable to the wavelength of light, the periodic structure has intriguing properties for the propagation of light. Light in a certain range of optical frequencies cannot propagate through the crystal and will be reflected, or if light is emitted inside the crystal it will remain confined in the crystal. Light with an optical frequency that is allowed to propagate in the crystal may have a very low group velocity.

In this thesis, we investigated two-dimensional photonic crystals, fabricated by perforating a thin membrane of transparent material with a hexagonal lattice of air holes. In such a perforated film, light in a certain band of optical frequencies cannot propagate. If a row of holes in the lattice is not perforated, states appear that allow the propagation of light along the row with optical frequencies that are not able to propagate in the lattice itself. Since the waveguide is embedded in a periodic medium, these waveguide can also have spectacular properties such as the ability to slow down light.

Slow light depends crucially on the geometry of the structure, i.e., the crystal lattice, the homogeneity in shape and size of the air holes and the surrounding dielectric. This property can be exploited for example for sensitive optical detectors or for switching light, since a small change in geometry results in a large change in optical properties. Similarly, when transmission efficiency is considered, any inhomogeneity in the lattice will result in propagation losses. For a full understanding of the intricate interaction of light and geometry,

that may change on the subwavelength scale, the optical field should also be monitored on this scale. Since a conventional microscope does not have the required subwavelength resolution and does not detect truly guided light, we used a so-called near-field microscope.

We described the working of the near-field microscope in chapter 2. In this microscope, a sharp glass needle is scanned over the surface of the structure under investigation. A minute fraction of the light underneath the needle couples to the needle. By detecting the intensity of the signal exiting the needle, a map can be reconstructed of were light is located inside the structure. By integrating the near-field microscope into one of the arms of an interferometer, the light can be measured in a phase-sensitive and time-resolved way. The light in one arm of the interferometer acts as a reference, which is mixed interferometrically with the light from the near-field probe. This method allows the determination of the phase velocity, the group velocity and also allows pulse deformation to be tracked as a function of time and position.

As the name already indicates, the near-field microscope measures the optical field close to an object at distances typically much smaller than the wavelength of light. In a photonic crystal waveguide, the light does not propagate solely in the dielectric material. A small portion of the light has an evanescent tail extending into the air above and below the waveguide. In chapter 3, we have studied this evanescent field with the near-field microscope. The rate with which the field decays above the structure depends on the wavevector of the light in the structure. Typically, the evanescent field decays single exponentially as a function of height. In photonic crystals however, the propagating waves are a superposition of multiple wavevectors, which causes the evanescent field to decay non-exponentially. Not only the large number of wavevectors of the light influence the decay of the evanescent field. The confinement of the light to a narrow waveguide also has a profound effect, since this requires a range of wavevectors in the direction perpendicular to the direction of propagation. By taking all wavevectors into account, in all directions, the decay of the evanescent field can be described appropriately.

As said, the optical properties of a photonic crystal waveguide depend strongly on the geometry of the structure. When the geometry is gradually changed as a function of position, the optical properties change accordingly. In chapter 4 showed how we can measure these properties locally with a near-field microscope. The optical properties are described in the dispersion relation, that describes what wavevectors may propagate at what optical frequencies. This relation is strongly dependent on, for example, the diameter of the holes of the crystal. If the holes in the crystal are enlarged gradually as a function of position, also the dispersion relation shifts in frequency. If the change in optical properties is gradual, the transition may be without losses, which is called an adiabatic transition. By measuring the phase and amplitude of the light in the waveguides with the near-field microscope, we can recoverer the shift of the dispersion relation. In order to do so, the dominant wavevectors in a small area need to be determined. A big analysis area has the advantage that the wavevector resolution is better. A larger area also means that the dispersion is averaged

over the large area. For a waveguide with a gradually increasing hole diameter as a function of position, we showed that the dispersion relation shifts to higher optical frequencies as the hole diameter increases.

In chapter 5, the so-called chirped waveguide described above was used to investigate the relation between group velocity and losses. We expected that a decrease of the group velocity results in an increase of the losses. Slow light has a longer interaction time with the same area of the structure and therefore also more time to find and scatter off imperfections. One generally assumes that these imperfections, being small fabrication errors, roughness of holes or the surface, have a very small effect on the propagation of light. In that case, the losses scale as the square of the group velocity. Our measurements show however, that the losses scale cubic with the group velocity. This observation appears to be conflicting with the initial expectation. Also the light pattern we measured is irregular at low group velocities, while it remains smooth at higher velocities. Both observations show that the assumption that the imperfections hardly influence the propagation, is false. In fact, our measurements show that the imperfections drastically alter the propagation of light.

In chapter 6, we studied the evolution of pulses in photonic crystal waveguides. In a photonic crystal, the group velocity is strongly dependent on the optical frequency of light. Such a strong dependence results in a high group velocity dispersion. This dispersion causes pulses to elongate symmetrically in time as they propagate through a medium. By following the pulses as they propagate, we determined the group velocity of the light. Our measurements also show that the elongation of the pulses is not symmetric in time. This elongation can be explained by the effect of higher-order dispersion, which plays a significant role in photonic crystal waveguides. By altering the geometry of the waveguide, for example by making the guide broader, the dispersion relation changes drastically. In the new dispersion relation, an eigenstate can be found with a low group velocity while having low dispersion. Our time-resolved measurements show that pulses with a group velocity 25 times lower than in vacuum, can propagate through the broader waveguide with very low deformation of the pulses. Our experiments show that the waveguide has a record high delay-bandwidth product of 30.

In chapter 7, the evolution of pulses is investigated that propagate through a passive photonic crystal filter, which is build from several components. Each of these components has unique eigenstates for propagating light, which are coupled to one and other. Analysis of such structure is difficult since many different states can be excited simultaneously in the same area. By translating our measurement to the spatial frequency domain, the wavevectors can be made visible. Since each wavevector can be assigned uniquely to the eigenstates, the states can be investigated individually. Our analysis method shows that the energy in each of the states can be tracked in time. The thus acquired evolution of the pulses in the composite structure showed for example, what portion of the light is reflected back to the input and with what femtosecond time difference the pulses exit each component.

Samenvatting

Elektronica heeft het leven in de westerse wereld drastisch veranderd de afgelopen decennia. Continue vooruitgang op het gebied van chips en opslagmedia heeft steeds meer mogelijk gemaakt en zal in de toekomst ook nieuwe technologie mogelijk maken. Deze technologie zal echter uiteindelijk een fundamentele grens bereiken. Een voordehandliggende grens is bijvoorbeeld dat elektronische componenten niet kleiner kunnen worden dat een enkel molecuul.

In de transatlantische telecommunicatie liep men al in de jaren tachtig tegen de beperkingen van koperkabel aan. De oplossing hiervoor werd gevonden in de optica: met een glasvezelkabel kan de dataoverdracht veel efficiënter plaatsvinden, omdat verliezen kleiner zijn en het makkelijker is om overspraak te vermijden als er meerdere signalen tegelijk door de kabel verstuurd worden. Door de ontwikkelingen op het gebied van opto-elektronica is de prijs van deze systemen zo laag dat glasvezelbekabeling inmiddels ligt niet alleen in de oceaan ligt, maar ook in dorpen en steden, met als voornaamste doel breedbandige telecommunicatie mogelijk te maken in elk huishouden.

Om te begrijpen hoe de snelheid van telecommunicatienetwerken een nieuwe technologische boost kan krijgen, moeten we kijken naar de schakelelementen in deze netwerken. In deze zogenaamde routers worden de optische signalen vertaald naar elektrische en zo verder verwerkt. Na verwerking, worden de resulterende signalen weer vertaald naar optische signalen voor verder transport. De vertaling van optische naar elektronische signalen en vice versa limiteert momenteel de snelheid van communicatienetwerken. Als deze routers met enkel optische signalen zouden werken zou de snelheid verbeteren. Een cruciaal onderdeel van een optische router is de optische schakelaar.

Voor het bouwen van een optische schakelaar, moet licht een sterkte interactie hebben met het materiaal waarin het voortbeweegt. Een veelbelovende technologie hiervoor zijn de fotonische kristallen. Fotonische kristallen zijn structuren waarin de brekingsindex pe-

riodiek varieert, door gebruik te maken van twee verschillende materialen bijvoorbeeld silicium en lucht. Door de periode even klein te kiezen als de golflengte van licht, krijgt de periodieke structuur interessante optische eigenschappen. Zo kan licht in een bepaalde frequentieband niet door het kristal propageren en zal gereflecteerd worden, of als het licht in het kristal ontstaat zal het opgesloten blijven. Licht met een optische frequentie die wel mag voortbewegen in het fotonisch kristal kan een erg lage voortplantingssnelheid hebben. Dit langzame licht kan wellicht gebruikt worden om een efficïente optische schakelaar te maken.

In dit proefschrift is gebruik gemaakt van twee-dimensionale fotonische kristallen, gemaakt in een dunne film van een transparant materiaal, waar een hexagonaal rooster van kleine gaten in is geëtst. Ook in zo'n geperforeerde film kan licht in een bepaalde frequentieband niet propageren. Als nu een rij gaatjes niet geëtst is in het rooster ontstaan er propagerende toestanden in deze rij bij frequenties die in het rooster niet toegestaan zijn. De rij niet-geëtste gaatjes vormen daardoor een golfgeleider met een beperkt aantal eigentoestanden. Omdat de golfgeleider is ingebed in een periodiek medium, verschillen de eigentoestanden aanzienlijk van de eigentoestanden van niet-periodieke lichtgeleiders. Een zeer spectaculaire eigenschap van deze golfgeleiders is dat licht bij bepaalde optische frequenties met een lage groepssnelheid kan propageren.

De propagatie van langzaam licht is sterk afhankelijk van de geometrie van de fotonisch kristal golfgeleider, zoals het rooster, de homogeniteit van de vorm en grootte van de gaatjes en het omringend diëlektricum. Dit gegeven kan worden gebruikt voor gevoelige optische sensoren of het schakelen van licht. De gevoeligheid voor de geometrie heeft ook gevolgen voor de transmissie van licht door de golfgeleider, omdat elke kleine imperfectie in de structuur verliezen veroorzaakt. Omdat een dergelijke structuur het voortbewegen van licht op de subgolflengteschaal kan beïnvloeden, dient het licht ook op deze schaal bestudeerd te worden. Omdat deze resolutie niet haalbaar is met een conventionele microscoop en ook omdat dergelijke microscopen geleid licht in een golfgeleider niet zichtbaar kunnen maken, hebben we voor de studie van licht in de fotonische kristallen gebruik gemaakt van een zogenaamde nabije veld microscoop.

In hoofdstuk 2 is beschreven hoe de nabije-veld microscoop werkt. In deze microscoop wordt met een zeer scherpe glazen naald het oppervlak van het fotonisch kristal afgetast. Hierbij wordt de naald op een constante afstand van ongeveer 10 nm boven het oppervlak gehouden. Van het licht dat voortbeweegt onder de naald, zal een klein gedeelte overkoppelen naar de naald. Door aan het eind van de naald een detector te plaatsen en de naald over het oppervlak te scannen, kan worden bepaald waar het licht zich bevindt. Door de gehele microscoop te integreren in een tak van een interferometer kunnen licht pulsen zowel fasegevoelig als ook tijdsopgelost gemeten worden. Het licht in één tak van de interferometer doet dienst als referentie, dat interferometrisch gemengd wordt met het licht van de naald. Met deze methode kan de fasesnelheid en groepssnelheid gemeten worden, maar ook kan de vervorming van de pulsen als functie van tijd en plaats gevolgd worden.

Zoals de benaming al aanduidt, kan een nabije-veld microscoop het optische veld dicht bij een object meten op een afstand die typisch kleiner is dan de golflengte van het licht. In een fotonisch kristal golfgeleider beweegt het licht zich niet enkel in het diëlektrisch materiaal voort. Het licht heeft een kleine evanescente staart in de lucht boven en onder de golfgeleider. Deze evanescente staart hebben we gemeten met de nabije veld microscoop. De resultaten zijn beschreven in hoofdstuk 3. Hoe snel de intensiteit boven de golfgeleider afvalt als functie van de hoogte, hangt af van de golfvector van het licht in de structuur. Typisch vervalt de intensiteit exponentieel als functie van de hoogte. In fotonische kristallen echter, hebben de propagerende golven niet één, maar een oneindig aantal golfvectoren, wat een niet-exponentieel verval van het evanescente veld ten gevolge heeft. Niet alleen de vele golfvectoren van het licht in de golfgeleider bleken invloed te hebben op het evanescente veld. Ook het feit dat het licht opgesloten is in een smalle golfgeleider heeft een significant effect, omdat hiervoor ook golfvectoren nodig zijn in de richting loodrecht op de voortplantingsrichting. Door alle golfvectoren in alle richtingen mee te nemen, kan het evanescente veld van een fotonisch kristal golfgeleider wel goed beschreven worden.

Hoofdstuk 4 liet zien hoe de optische eigenschappen van een fotonisch kristal golfgeleider kan veranderen als functie van positie, en hoe we deze optische eigenschappen lokaal kunnen meten met de nabije veld microscoop. De optische eigenschappen worden beschreven in de dispersierelatie, die beschrijft welke golfvectoren bij welke optische frequentie toegestaan zijn. Deze relatie is sterk afhankelijk van, onder andere, de diameter van de gaatjes van het kristal. Als de gaatjes van het kristal naast de golfgeleider geleidelijk wordt vergroot als functie van positie, verschuift ook de dispersierelatie als functie van positie. Door met onze nabije veld microscoop de fase en amplitude van het licht in de golfgeleider te meten, kunnen we het verschuiven van de dispersierelatie meten. Hiervoor moet een klein gebied gekozen worden, waarvan de dominante golfvectoren kunnen worden bepaald. Hoe groter dit gebied wordt gekozen, des te beter is de resolutie van de gevonden golfvectoren. Een groot analysegebied betekend echter ook een dat de gevonden data een gemiddelde is van dit hele gebied. Voor de golfgeleider met geleidelijk veranderende eigenschappen konden we laten zien dat de dispersierelatie van de golfgeleider naar hogere frequenties opschuift als de diameter van de gaatjes vergroot wordt.

In hoofdstuk 5 werd de hierboven beschreven golfgeleider gebruikt om de relatie tussen groepssnelheid en verliezen te onderzoeken. We verwachtten dat langzaam licht grotere verliezen zal hebben. Het langzaam voortbewegende licht heeft immers een langere interactietijd met de structuur en heeft derhalve ook meer tijd om imperfecties in het kristal te vinden en daaraan uit de golfgeleider te verstrooien. In het algemeen wordt aangenomen dat de imperfecties, door kleine fabricagefouten, ruwheid van gaatjes of ruwheid van het oppervlak, een zeer klein effect hebben op het voortbewegen van licht. In dat geval zouden de verliezen schalen met het kwadraat van het groepssnelheid. Uit onze metingen blijkt echter dat de verliezen schalen met de derde macht van de groepssnelheid. Dit lijkt niet te stroken met de theorie. Ook de intensiteitsverdeling van het licht met een lage groeps-

snelheid is onregelmatig, terwijl die met hogere groepssnelheid wel regelmatig is. Deze observaties laten doen vermoeden dat de aanname dat de imperfecties de propagatie niet beïnvloeden, onjuist is. Ons onderzoek bewijst dat de imperfecties de optische eigenschappen zelfs domineren en daardoor de voortbeweging van licht aanzienlijk veranderen.

In hoofdstuk 6 werd de dynamica van pulsen in fotonisch kristal golfgeleiders bestudeerd. In een fotonisch kristal is de groepssnelheid sterk afhankelijk van de frequentie van het licht. Zo'n sterke afhankelijkheid noemen we een hoge groepssnelheiddispersie. Deze dispersie zorgt ervoor dat pulsen symmetrisch langer worden in de tijd als ze door een medium voortbewegen. Door de pulsen te volgen in de tijd, hebben we de groepssnelheid bepaald. Onze metingen laten zien dat deze verbreding niet symmetrisch is. Blijkbaar speelt hogere orde dispersie een significante rol in deze golfgeleiders. Door de geometrie van de golfgeleider te veranderen, door de geleider bijvoorbeeld breder te maken, wordt de dispersierelatie ook drastisch veranderd. In de nieuwe dispersierelatie is een eigentoestand te vinden met een lage groepssnelheid en weinig dispersie. Onze tijdsopgeloste metingen laten zien dat de pulsen die met een snelheid welke 25 keer lager is dan die in vacuüm voortbewegen, weinig dispersie vertonen en daardoor de pulsen nagenoeg niet vervormen.

In hoofdstuk 7 wordt de dynamica van pulsen in een passief fotonisch kristal filter bekeken welke opgebouwd is diverse componenten. Elk element heeft unieke eigenstoestanden. De toestanden van elk element zijn gekoppeld. Analyse van dergelijke structuren is moeilijk aangezien de diverse toestanden tegelijkertijd aangeslagen worden in hetzelfde gebied. Door de meetresultaten te vertalen naar het ruimtelijke frequentiedomein, kunnen de golfvectoren zichtbaar gemaakt worden. Aangezien de golfvectoren uniek toegewezen kunnen worden aan enkele eigentoestanden, kunnen deze eigentoestanden individueel bestudeerd worden. Onze analysemethode laat dan ook zien dat de dynamica van pulsen in dergelijke complexe structuren met een hoge precisie bestudeerd kunnen worden.

Dankwoord

"Wat ik na mijn afstuderen ga doen? Nou, een promotieonderzoek doen lijkt me maar niks, daar heb ik het geduld niet voor."

ik, 2003

Tsja, na vier jaar promoveren moet ik deze woorden toch terugnemen. Het is dan ook zeker geen eindeloze lijdensweg geworden wat ik misschien vreesde tijdens mijn afstudeerperiode. Integendeel, de afgelopen vier jaar waren ontzettend boeiend en ik heb me geen moment hoeven vervelen. Wat me uiteindelijk over de streep trok om te beginnen was het enthousiasme van Kobus en zijn manier van onderzoek doen. Het lijkt soms wel of wij een onderwerp opzoeken wat technisch bijna onmogelijk is en dan eens kijken wat voor rare dingen we zien als we gaan meten. Omdat je vooraf geen idee hebt wat je zoekt en/of gaat vinden is ons werk altijd weer verrassend. Kobus, ik heb genoten van onze discussies, vooral als de resultaten weer eens niet eenvoudig uit te leggen waren. De laatste jaren wist je feilloos door mijn bluf heen te prikken, wat toch aangeeft dat we elkaar erg goed aanvoelen. Bedankt voor alles de afgelopen jaren.

Ik begon met mijn promotie toen Marijn bezig was de microscoop te bouwen waarmee ik nog jaren zou werken. Marijn, ik vond het erg leuk om samen met jou de problemen met de opstelling aan te pakken. Ondanks de tegenslagen in die tijd was je toch altijd mijn opgewekte kamergenoot. Je was ook een ideale reisgenoot voor onze internationale tripjes door je relaxte houding en gevoel voor humor.

Zoals gezegd, er waren nogal wat probleempjes met de microscoop in Amsterdam. Ik ging daarom in het eerste jaar nog een paar keer naar Enschede om daar metingen te doen. Daarvoor wil ik Niek en zijn groepsgenoten graag bedanken. Ook na mijn afstuderen

kwam ik graag terug naar Twente, waar ik altijd behulpzame en enthousiaste mensen om me heen vond. En die behulpzame mensen uit Twente konden we ook in Amsterdam wel gebruiken, aangezien we de microscoop maar niet goed aan de praat kregen. Jeroen en Frans bedankt voor jullie hulp met de nabije-veld microscoop. Met Hinco, Marco, Idsart, Henk en Ton hebben jullie samen onze microscoop omgetoverd tot een supertool waarmee we toponderzoek kunnen doen en waar ik met veel plezier mee heb gewerkt.

Jord, jij was ongeveer tegelijk met mij begonnen in Amsterdam, ook al afkomstig van T10. Nu heb ik de neiging om op onmogelijke tijden te werken, zoals bij zonsopkomst tijdens mijn metingen in Twente, maar ook tijdens de vakanties was ik soms aan het werk in een leeg AMOLF. Nouja, bijna leeg dan, want jij was er ook geregeld. Altijd gezellig om even te buurten bij een mede workaholic.

Matteo, you were a breath of fresh air in our group. You taught us to appreciate real coffee and home-cooked Italian food. To be continued? The last years our group expanded further with the addition of Chris, Marko, Aron, Lydwin, Dries and Tobias. I hope you had and will have an enjoyable time in our group. I certainly had a good time with all of you. Ook mijn kamergenoten wil ik graag bedanken voor een leuke tijd. Vier jaar geleden waren dat nog Marijn en Joris, later Dima en nog wat later Otto en Dries. Jullie wisten met voldoende flauwekul de dagelijkse frustraties weg te spoelen.

Outside of the Netherlands I had some very interesting contacts that allowed me to do the work presented in this thesis, but also on a personal level I can look back on pleasant meetings with our Japanese friends Asakawa-san, Sugimoto-san and Baba-san. I would also like to thank Tim and Thomas for a great collaboration. I also have nice memories of my time with Silvia, I enjoyed your company wherever we were in the world.

Binnen AMOLF heb ik erg prettig samengewerkt met alle leden van de NanoPhotonics afdeling. Jullie behulpzaamheid en collegialiteit maakt het werken erg relaxed. Maar ook buiten het werk, bijvoorbeeld op de vrijdagmiddagborrel (!) en onze uitjes naar Ameland en België, workshops en conferenties was het altijd erg gezellig.

Gelukkig is er ook nog tijd om een beetje te ontspannen na het werk. Buiten de groepsuitjes, de barbecues, het voetballen (bedankt Tijmen), de AMOLF-uitjes (thanks PV) en een motorvakantie (bedankt Robert) heb ik ontdekt dat AMOLF de perfecte plaats is om aan je motor te knutselen. Er zijn namelijk genoeg Amolfers met een knutselafwijking die precies weten hoe je motorblokken verwisselt (bedankt Hinco), allerlei mechanische handigheidjes kennen (bedankt Wim en de rest van de werkplaats) en gelukkig zijn er ook nog elektrotechnici met aanhangers om je motorfiets op te laden (bedankt Idsart).

Weg van het promotiewerk heb ik lekker kunnen ontspannen bij mijn vrienden en familie. Eventuele frustraties kon ik bij jullie vergeten door een gezonde portie onzin en gezelligheid. Pim en René, bedankt det geej mien paranymphen ziet en mich nog efkes door de verdediging heen wille helpe. Die ontspanning heb ich auch kinne vinge as ich wir in Kepèl waas. Jeroen en Annelies, door uch veult toes nag steeds as toes as we der allemaol

zien.

As letste, bedankt pap en mam, netuurlik omdet ge mich op de wereld gezat hebt, veur uch leefde en omdet geej mich altied de ruumte hebt gegeave om miene eige weeg te goan. Doarum draag ich dit bukske gear aan uch op.